THE IN-SITU MEASUREMENT OF MECHANICAL PROPERTIES OF MULTI-LAYER COATINGS

by

PINYEN LIN

B.S., Chemical Engineering, National Taiwan University (1982)
M.S., Polymer Science and Engineering, Polytechnic University (1986)

SUBMITTED TO THE DEPARTMENT OF
MATERIALS SCIENCE AND ENGINEERING
IN PARTIAL FULFILLMENT OF THE REQUIREMENTS
FOR THE DEGREE OF

DOCTOR OF PHILOSOPHY IN MATERIALS SCIENCE AND ENGINEERING

at the

MASSACHUSETTS INSTITUTE OF TECHNOLOGY

June, 1990

© Massachusetts Institute of Technology, 1990, All rights reserved

Signature of Author _____

Department of Materials Science and Engineering
May 4, 1990

Certified by _____

Professor Stephen D. Senturia
Department of Electrical Engineering and Computer Science
Thesis Supervisor

Accepted by _____

Professor Thomas W. Eagar
Acting Chairman, Graduate Committee
Department of Materials Science and Engineering

MASSACHUSETTS INSTITUTE
OF TECHNOLOGY

JUN 12 1990

LIBRARIES
ARCHIVES

THE IN-SITU MEASUREMENT OF MECHANICAL PROPERTIES OF MULTI-LAYER COATINGS

by

PINYEN LIN

Submitted to the Department of Materials Science and Engineering
on May 4, 1990 in partial fulfillment of the requirements
for the degree of Doctor of Philosophy in
Materials Science and Engineering

ABSTRACT

An in-situ technique was developed for analyzing the mechanical properties of multi-layer polymeric films in terms of the properties of the individual layers. Several different materials, including a polyimide and three organic paint resins, were used in this study. The deflection of circular or square suspended membranes consisting of one or more polymeric layers was measured as a function of applied differential pressure. This so-called load-deflection behavior can be readily analyzed for a single layer to yield residual stress and the biaxial modulus. This thesis addresses the extension of the load-deflection technique to multi-layer films.

Sample fabrication methods for both square and circular suspended multi-layer films were developed for this study. Square multi-layer suspended films were made by spinning or spraying resin coatings on top of polyimide suspended membranes fabricated using microelectronic techniques, and curing them. Single- and multi-layer circular membranes were made without polyimide substrates by first applying the coating to a release layer, bonding a circular ring to the coating, then removing the coating from the release.

Finite element models for a single layer based on membrane mechanics were used to analyze the load-deflection behavior of the uncoated polyimide and the single-layer resin films. These results were used in a multi-layer finite element model for comparison with the experimental behavior of the multi-layer coatings. The results from the bi-layer films were in good agreement with those from single-layer films. This indicates that the load-deflection behavior of composite multi-layer coatings could be successfully analyzed in terms of the corresponding properties of the constituent layers. It was found that the effective biaxial modulus obeys a simple sum rule, while the residual stress must be corrected in the thicker films due to thickness-induced bending effects. The limitation of this technique is mainly from the variation of the film thickness, which reduces significantly the accuracy of the results for the films with more than three layers.

Thesis Supervisor: Dr. Stephen D. Senturia

Title: Professor of Electrical Engineering and Computer Science

Table of Contents

List of Figures

List of Tables

Acknowledgements

It is almost impossible to complete a thesis without help from other people. Many people have helped and supported me substantially during my stay at MIT. It is my great pleasure to acknowledge them.

First of all, I would like to thank my thesis advisor, Professor Stephen D. Senturia. He not only gave me technical advice on my work, but also provided me with a comfortable working atmosphere. His unfailing encouragement gave me the strength to continue my work even when the obstacles seemed insurmountable. He patiently taught me how to do research, to speak in public, to organize ideas, and to write reports. In ancient China, teachers were the most respected figures, after the emperor and one's own parents. Professor Senturia truly deserves this degree of respect.

For their help and cooperation in both experimental work and mechanical analysis, I would like to acknowledge the "mechanical measurement group" within our research group: Mark (now Professor) Allen, Jeffrey Y. Pan, and Fariborz Maseeh. They introduced me to the experimental work in the microelectronics laboratory, work on the humidity effect, and the use of ADINA programs.

Special thanks also go to Dr. Herb Neuhaus and Susan Noe. Herb was the most generous source of answers when I had questions about CAF and UNIX. Susan has been my most-consulted English and polymer information source, and was always enthusiastic in helping me. Both of them took great care of the green, lovely plants in the office, in which I have been for three years, and made it a nice place to stay.

I would also like to thank other group members: Joe Bernstein, Robert Harris, Michael Huff, Mehran Mehregany, Shaheen Mohamedi, Edward Murphy, Pradnya Nagarkar, Aleks Nikolich, Kay-Yip Ng, Professor Martin Schmidt, Daniel Sobek, David Volfson, and Albert Young. They have been a great source of information, ideas, and suggestions. In addition, I wish to express my thanks to our secretary Scotti Fuller, who was always helpful when I ran out of time.

I would like to thank my thesis committee, Professors Frederick J. McGarry and David K. Roylance. Their suggestions and criticisms were very valuable to this work. Very useful suggestion on the mechanical analysis were supplied by Professors Klaus-Jurgen Bathe and Rohan Abeyaratne. Without their useful discussion, the mechanical modelling would not have been successful.

This work was primarily sponsored by the E. I. DuPont du Nemours and Company. The U. S. Department of Justice (contract J-FBI-88-067) funded much of the FEM analysis work. The coatings were supplied and sprayed by the Marshall Laboratory of DuPont Company. I would like to express my gratitude to Dr. Paul McGonigal, Dr. Bill Golton, Dr. Frank Rohrbacher, Joanne Paci, and Griffin Tall, for their help in the coating process. Additional sample preparation was carried out in the Microelectronics Laboratory of the MIT Center for Materials Science and Engineering, which is supported in part by the National Science Foundation under contract DMR-87-192117, and the Microsystems

Technology Laboratories. I am very thankful for the dedication of the technicians who kept equipment running well: Richard Perilli, Darrell Roan, Doug Young, Octavio Hurtado, and Paul McGrath. The uniaxial tensile tests were carried out in the Professor McGarry's laboratories. I wish to acknowledge John Moalli for teaching me how to operate the machine and for arranging special schedules for me when I was in a big rush to get results.

A lot of comments on and corrections to this thesis were given by the instructors at the MIT Writing Center in order to make it readable. I would like to take this opportunity to thank them for their effort.

I am grateful to my wife, Shang-Chyan Chen, for providing me a loving home and for understanding my frequent absence in the evening and weekends. I also wish to thank my parents and parents-in-law for their caring and generous support.

CHAPTER 1

Introduction

1.1 Motivation and Goals of Thesis

Polymeric coatings have been used in many ways from automobile paints to package coatings for integrated circuits. It is important to understand the mechanical properties of coatings in order to ensure they fulfill their designed functions [1]. Among the mechanical properties, the biaxial modulus, the residual stress, and the in-plane Poisson ratio of the coatings are particularly interesting since they describe the fundamental behavior of the material as a thin film. To measure these properties, the *in situ* measurement techniques are desirable since these techniques measure the mechanical properties of coatings while they are in use.

At present, the residual stress measurement is usually performed using *in situ* techniques, while the modulus and the in-plane Poisson ratio measurements are most often carried out by other free-film techniques which require the removal of coatings from substrates. The requirement of free-film samples not only makes it impossible to measure the residual stress, but also may modify the properties of coatings. For example, for residual stress which exceeds the limit of the linear elasticity regime, the free-film tensile measurements may cause a problem of accuracy. In addition, the in-plane Poisson ratio measurement from free-film techniques has poor reproducibility due to the low precision of the measurement of the tiny change in the lateral strain of thin coatings.

Most coatings are based on organic polymers and many are multi-layered. The materials of multi-layer paints, such as those used on automobiles, usually vary from layer to layer, which causes nonuniformity of mechanical properties throughout the thickness [2,3]. The multi-layer structure of coatings increases the difficulty of mechanical analysis since the behavior of multi-layer films is not a simple average of single-layer behavior [4,5]. The mechanical behavior of multi-layer coatings has not been well characterized, and very few researchers have reported a satisfactory way to analyze multi-layer problems.

The blister method is one way to measure mechanical properties of thin films *in situ* [6-11]. In this method, the deflection of a suspended film is measured as a function of applied pressure; this is known as the load-deflection behavior. The biaxial modulus and the residual stress of the films can be extracted simultaneously from the relationship between the applied pressure and the deflection using a mathematical model. Using this technique, the in-plane Poisson ratio can also be calculated by comparing the value of biaxial modulus with the value of Young's modulus from uniaxial tensile tests [12]. Hence, the blister method and the uniaxial tensile tests have been chosen for this study. However, the current techniques for fabricating test samples for the blister method are not suitable for polymeric coatings partly due to the low chemical stability of coatings. In addition, the mathematical model deals only with thin single-layer films, and hence, this model is not applicable to the study of multi-layer coatings.

The goal of this work is to develop experimental techniques and corresponding mathematical models for the *in situ* measurement of the mechanical properties of multi-layer polymeric coatings. The first part of the goal will be accomplished with the development of an *in situ* measurement technique which can be adopted by the coating industries for routine measurement. In developing this technique, three issues have to be considered: (a) the fabrication of precise samples, (b) the reproducibility of mechanical measurements, and (c)

the ease of adoption of this technique by the coating industry. This implies that this technique has to be capable of handling the multi-layer structure of coatings commonly used for polymeric coatings. This technique will provide a new way to evaluate the mechanical properties of each layer in a multi-layer coating system. A design of a chamber to control the environmental conditions for the blister tests is also discussed in this development as well.

The second part of the goal is to develop mathematical models for thick films and to apply it to multi-layer coatings tested by the blister method. At present, only simplified thin models are available. This causes errors in the evaluation of mechanical properties of thicker films. As coatings get thicker, bending energy must be considered in the blister method. Thus, the new model has to include this thickness effect and be usable for the evaluation of mechanical properties of multi-layer coatings. Both analytical solutions and the finite element method are used for this purpose.

1.2 Multi-layer Polymeric Coatings

Polymeric coatings have been used in human society in a variety of ways. The various coating products — paints, varnishes, lacquers, enamels, chemical coatings, maintenance finishes, etc. — have been used to protect, decorate, and provide functional properties to a number of surfaces and objects [2]. The composition of polymeric coating usually includes polymers (resins), solvents, pigments, additives, and extenders [13]. Nevertheless, not all polymeric coatings have all of these ingredients.

Three commercially available coatings were selected for this study. These polymeric coatings are clear finishes for the automobile and truck bodies and flexible finishes for plastic substrates of automobiles [14]. The mechanical properties of these

paints are quite different since they are designed to fit different purposes. The main requirements for these finishes are appearance, durability and corrosion protection. The finishes are mainly comprised of undercoats or primers and topcoats. Primers are applied mainly to prevent corrosion, in addition to smoothing out small imperfection. Topcoats are usually formulated to impart high gloss and excellent appearance.

Another polymer material studied in this work is polyimide. Polyimide (PI) is a class of polymers produced form dianhydrides reacted with diamines [15]. It has been widely used as an electronic insulator in microelectronics and as a composite component in other fields due to its low dielectric constant and excellent thermal and chemical stability [16]. The PI suspended membrane for the blister method has been successfully produced using microelectronic fabrication [10,17]. In this study, the PI suspended membrane was used as a base on which other coatings were coated. That is, multi-layer square samples were made by applying different coatings on top of single-layer PI samples.

1.3 Mechanical Property Measurements

1.3.1 Biaxial Modulus

A coating with high modulus can strengthen the coated substrates. However, a high modulus implies brittleness, which may reduce the toughness of the material and cause cracking problems. The most common way to obtain the biaxial modulus is to measure Young's modulus which is modified from the biaxial modulus by a factor of one minus the Poisson ratio (Eq. 1.1).

$$\text{Biaxial modulus} = \frac{\text{Young's modulus}}{1-\nu} \tag{1.1}$$

where ν is the Poisson ratio. This measurement is done using a uniaxial tensile test instrument on the coatings released from the substrate. To fabricate free-film samples, the polymer coatings are coated on a weakly adhering substrate; or, the adhesion between coatings and substrates is weakened by specific solutions or vapors after the curing process. Then the coating is removed from its substrate as a free film and is cut into an appropriate shape for a standard tensile test. The modulus is obtained from the relationship between stress and strain.

Although the equipment for the uniaxial tensile test is reasonably easy to operate, there are some drawbacks. First, it is very hard to remove coatings from their substrate without modifying their properties. The film may be damaged during the process of peeling and/or shape cutting, especially when coatings are very brittle and fragile. In addition, the requirement of free-film samples in tensile tests causes the loss of the information about residual stress. Finally, this measurement is adequate only for residual stress (or strain) which does not exceed the limit of the linear elasticity regime of coatings. The modulus measurement from a released coating may deviate from the real coating properties when the residual stress is beyond the linear elastic regime. Thus, it is desirable to measure Young's modulus *in situ*.

1.3.2 Residual Stress

Residual stress is an important parameter in terms of mechanical failure of the coatings. Originating in the curing process, residual stress includes two parts: intrinsic stress and the stress due to the mismatch of the thermal expansion coefficient between coatings and substrates [18,19]. The intrinsic stress is generated by the evaporation of solvents, the loss of small molecules due to chemical reaction, and the restrictive force in the interface of polymer films and substrates [20]. The intrinsic stress is dependent on

conditions such as chain mobility at cure temperature, degree of crosslinking, and so forth. The thermal expansion coefficients of polymeric coatings are usually larger than those of substrates such as ceramics, metal, etc. Therefore, tensile residual stress is more commonly found in the polymeric coatings than compressive residual stress.

The importance of residual stress is four-fold. First, high residual stress aggravates the problems of cracking and adhesion failure to the coatings [21]. Second, it may introduce cracking to coatings applied on an irregular surface where the residual stress concentration is high [22]. Third, the residual stress may deform the shape of the coated subjects, since the residual stress provides an intrinsic force to distort the coated subject. Fourth, other physical properties, such as permeability, are also affected by residual stress. The presence of such residual stress certainly affects the mechanical properties of coatings and/or the substrates. As mentioned above, in a case of very high residual stress, it may invalidate the results of the free-film tests due to the nonlinear elasticity of coatings.

Many stress-measuring techniques for residual stress have been developed recently [23-27]. Residual stress in both inorganic and organic thin films on various substrates has been measured [28-30]. For organic coatings, the most widely used technique is the plate or beam deflection method (Fig. 1.1) [31-34]. In the case of plates, circular plates were most often used due to their geometric simplicity. The procedure of residual stress measurement is the following. The organic paints are first coated onto the substrate which may be a plate or a strip. When residual stress is built up within the paints, the substrate is warped or bent. The curvature of the deflected substrate can be measured optically, electrically, or mechanically [26,35]. By applying an adequate mathematical model, such as the Stoney equation [36] for the circular plate, the residual stress of coatings can be determined [25]. Similar techniques to measure the residual stress of inorganic coatings on single crystal silicon wafers have been reported as well [37,38].

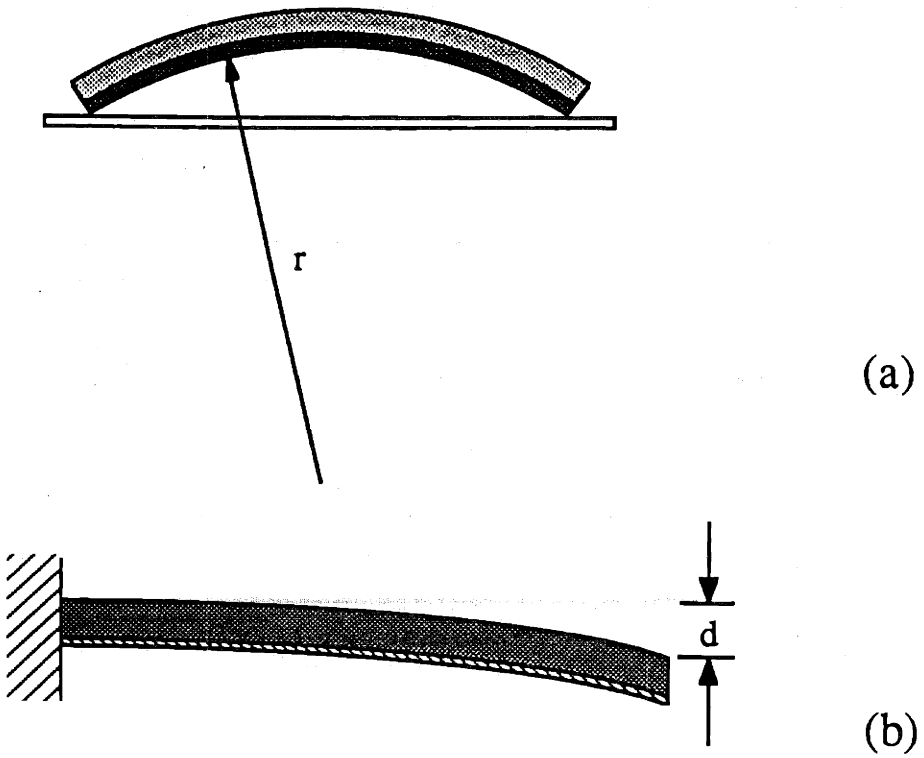

Figure 1.1 (a) The plate deflection method; (b) the beam deflection method.

In this method, the experimental work is not complicated and the temperature dependence of residual stress can also be studied. There are, however, some disadvantages. For organic coatings, the residual stress is usually smaller than that of inorganic or metallic films. Thus, the curvature or the deflection of the substrate may be very small and difficult to determine easily and accurately. Since the substrate is usually a metallic or an inorganic substrate, the surface of which can be optically smooth, the problem of small deflections can be solved by using an expansive, sophisticated optical instrument [39,40]. However, this instrument may not be applicable for a polymeric substrate whose surface is apparently not optically smooth. An alternative way to solve the

small deflection problem is reducing the thickness of the substrate. However, the bending stiffness of coatings, which originally could be neglected in the thick-substrate situation, then becomes significant. In this case, the Young's modulus of the coating is needed before determining the residual stress [41-45]. In addition, the stress measured by these methods are the average stress along the film. The stress difference across the substrate can not be obtained by this method.

1.3.3 In-Plane Poisson Ratio

The in-plane Poisson ratio measurement is not commonly carried out due to difficulty in measuring tiny changes in the lateral strain of thin coatings. Bauer [46] measured the pressure dependence of stress on a thin film under a uniaxial load. Both in-plane and out-of plane Poisson ratios can be evaluated from this method. However, this technique also requires removal of coating from the substrate, which includes the disadvantages of the free-film technique. Alternately, the bulk Poisson ratio, measured from a bulky solid chunk instead of a thin coating, has been used to substitute the in-plane Poisson ratio. However, it is arguable whether or not the bulk Poisson ratio is the same as the in-plane Poisson ratio.

By using the blister method for different shapes of films, such as square and rectangular, the separation of the Young's modulus from the in-plane Poisson ratio can be achieved in theory because of the different Poisson ratio dependence in different geometries [47]. The advantage of this technique is that the in-plane Poisson ratio can be measured simply by applying the blister method to samples with different geometries. However, this technique is in a preliminary stage and is still under investigation.

Another feasible way to measure in-plane Poisson ratio is to use the blister method together with the uniaxial tensile test since the results from both methods, the biaxial modulus and the Young's modulus, also have different Poisson ratio dependence [48]. That is, the ratio of the Young's modulus and the biaxial modulus is one minus the Poisson ratio (1-ν). The disadvantage of this method is similar to the drawbacks of free-film tensile tests; especially, the sample preparation of tensile tests needs tremendous caution. Nevertheless, this technique seems to provide the most straightforward way of measuring the in-plane Poisson ratio. Hence, this technique will be used in this study.

1.3.4 Blister Method

Another way of improving the above-mentioned plate or beam deflection method in Section 1.2.2 is to create a suspended membranes by removing a portion of the substrate. This method (Fig. 1.2) is called the blister method (or sometimes the load-deflection method) [6-11]. It was originally designed to measure the stress-strain relationships in a thin film by applying pressure on one side of the unsupported region and observing film deflection using interferometry or microscopy techniques [6-8]. Recently, this method has been used to determine the biaxial modulus and the residual stress of thin coatings. These properties are extracted from the relationship between the applied pressure and the deflection using a mathematical model.

The advantages of this *in situ* technique are: (a) problems of handling free-film samples are eliminated; (b) knowing Young's modulus of films in advance is not necessary; (c) the in-plane Poisson ratio can be obtained together with other mechanical measurements. The limitation of the blister method is that only tensile residual stress can be detected, since compressive residual stress wrinkles the suspended films which make them unusable for the deflection measurement [25].

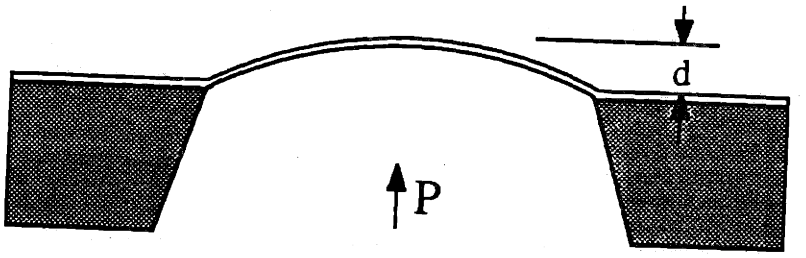

Figure 1.2 Cross-section of a suspended film undergoing a blister method.

A nice way to prepare suspended films is to introduce microfabrication techniques [10]. Using these techniques, the front side of silicon substrate is highly doped with boron. A hole can be created by etching from the back side of the silicon substrate using an etchant which stops at the boron doped layer. After the organic coating is deposited on the boron-doped layer, the boron-doped layer is then removed, leaving a suspended organic film.

There are several advantages to this technique. First, the surface of silicon substrate is clean and smooth so that the properties of films are reproducible. Second, the size of the suspended membranes can be precisely controlled by photolithography. Polyimide suspended films have been successfully fabricated by these techniques in a clean room facility [47,49]. To apply these techniques to any polymeric coatings, however, coating materials are found usually incompatible to the clean room facility. In addition, the sample fabrication time for this technique is long (approximately four hours per silicon wafer).

1.4 Organization of Thesis

In Chapter 2 the experimental methods used in this work are discussed. In particular, the materials examined, the sample fabrication for the blister test and the uniaxial tensile test, and the measurement setup are described in details. The mathematical models for load-deflection experiments, which include the multi-layer models and the thickness effect on the single-layer models, are presented in Chapter 3. In Chapter 4, the finite element analysis is used for calculating the constants of the models introduced in Chapter 3. The results of load-deflection experiments and uniaxial tensile tests are shown in Chapter 5. The humidity effect on the mechanical properties of coatings using load-deflection technique is given in Chapter 6. Finally, Chapter 7 shows the summary and the conclusion of the this measuring technique.

CHAPTER 2

Materials And Experimental Methods

2.1 Introduction

The mechanical properties of polyimide (PI) and three polymeric resins used in automotive paints were investigated in this study. Both single-layer and multi-layer films were made from these materials for mechanical measurements using the blister test and the uniaxial tensile test. Due to the differences in techniques of sample fabrication, there were two types of samples: coatings with PI and coatings without PI. The blister test provided information about the biaxial modulus and residual stress of films, while Young's modulus was obtained from the uniaxial tensile test. The comparison of the results from the two mechanical tests was made to evaluate the in-plane Poisson ratio of films. In summary, the types of samples were shown in Table 2.1. The detail description of materials is given in Section 2.2.

The samples containing PI included PI single-layer films and PI+coatings (PI with one or more paints) multi-layer films. The samples for the blister test were square suspended films and the samples for the uniaxial tensile test were ribbon-like films. Both types of samples were fabricated using microelectronic techniques. The effect of solvents on mechanical properties of PI was also examined using the blister test on single-layer PI samples.

The samples without PI were fabricated using a coat-and-peel method. These samples included single-layer coating films and multi-layer coating films. Circular

suspended films were the samples for the blister test, and ribbon-like free films were the samples for the uniaxial tensile test. The effect of humidity on the mechanical properties of coatings was also investigated using the blister test on single-layer coating samples.

Test	1 layer	2 layers	3 layers	4 layers
Blister Test (Square)	PI	PI+APC PI+APC-D PI+PEU	PI+APC+APC-D PI+APC-D+PEU PI+PEU+APC	PI+APC+APC-D+PEU PI+PEU+APC+APC-D
Blister Test (Circular)	APC APC-D PEU	APC-D+APC PEU+APC-D APC+PEU	APC-D+APC+PEU PEU+APC-D+APC	
Tensile Test	PI APC APC-D PEU	PI+APC APC+PEU APC-D+PEU		

Table 2.1 The summary of the single-layer and multi-layer samples for mechanical property measurements using the blister test and the uniaxial tensile test. PI is polyimide; APC is acrylic polymer coating; APC-D is acrylic polymer coating with dispersed resins; PEU is polyester urethane. PI+APC+APC-D means that PI is the bottom layer, APC is in the middle, and APC-D is the top layer.

This chapter begins with an introduction of the materials studied in this work. Next, the sample preparation for the blister test is described. The techniques for measuring film thickness are described in Section 2.5. Then, the measurement setup and experimental procedure for the blister test are given in Section 2.6. Finally, the sample preparation and the equipment setup for the uniaxial tensile test are detailed in Section 2.7.

2.2 Materials

Polyimides (PI) and three different polymeric resins were selected for *in situ* mechanical property measurements. In this study, PI served as a basic layer for fabricating multi-layer square samples using microelectronic techniques for the blister test. That is, the polymeric coatings were always deposited onto the PI layer when making multi-layer square samples.

All coatings in this study were resins used on automobiles and they were supplied by the Marshall R&D Laboratories of E. I. DuPont de Nemours and Company. They were chosen for several reasons. First, these coatings were quite different in their mechanical properties, which provided a broad testing range for mechanical measurement. Second, the coatings used here were composed of polymer resins and crosslinking agents only and contained no additives such as pigments. It is desirable to begin with such simple systems, especially since paints usually have a complicated formula.

The procedures to produce these coatings are described in detail in several U.S. patents [50,51]. Brief descriptions of the composition of each coating are given in the following sections.

2.2.1 Acrylic Polymer Coating

This coating is used primarily as a topcoat over automobiles and truck bodies [50,52]. It is designed for good durability, weatherability and adhesion to base coats as well as excellent aesthetic appearance. The coating is supplied in solution form with about 70% solid content. The process to make this coating typically includes two steps: (1) make

an acrylic polymer; (2) mix it with melamine formaldehyde crosslinking agents. This coating is called acrylic polymer coating (APC) in this study.

The monomers typically used to produce the acrylic polymer (in the first step) are shown in Table 2.2. To avoid confusion with the next section, this acrylic polymer is called acrylic polymer I. The composition by weight is about 15% styrene, 30% butyl methacrylate, 17% butyl acrylate, 38% hydroxyl propyl acrylate. This polymer is made by radical polymerization in a solution which is composed of monomers, solvent (xylene), polymerization initiators. The final polymer solution has about 71% solid content and the weight-average molecular weight of acrylic polymer I is about 6,000.

Monomers	Structures
Styrene	$CH_2=CH-C_6H_5$
butyl methacrylate	$CH_2=C(CH_3)-COOC_4H_9$
butyl acrylate	$CH_2=CH-COOC_4H_9$
hydroxyl propyl acrylate	$CH_2=CH-COOC_3H_6OH$

Table 2.2 The major monomers needed to make acrylic polymer I.

The next step is to add crosslinking agents (methylated and butylated melamine formaldehydes) to the solution of acrylic polymer I. The chemical structure of melamine is shown in Fig. 2.1a. Melamine is reacted with formaldehyde (HCHO) to form melamine formaldehyde (Fig. 2.1b). Melamine formaldehyde can form polymers through several polymerization mechanisms (Fig. 2.2). The degree of polymerization is about 1-3. This melamine formaldehyde is then reacted with methanol and/or butanol to form the

crosslinking agents of this coating: methylated and butylated melamine formaldehydes (Fig. 2.3). An acid catalyst solution such as dodecylbenzene sulfonic acid (less than 2% by weight) is added to the coating to increase the crosslinking rate during cure. Several possible crosslinking mechanisms (between acrylic polymer I and methylated/butylated melamine formaldehydes) in the presence of acid catalyst are shown in Fig. 2.4 [53]. The active functional groups for crosslinking are the hydroxyl groups of acrylic polymer I and the methylated and butylated methylol groups of melamine formaldehydes. The mixing ratio (by weight) of acrylic polymer I to methylated and butylated melamine formaldehydes is about 2:1.

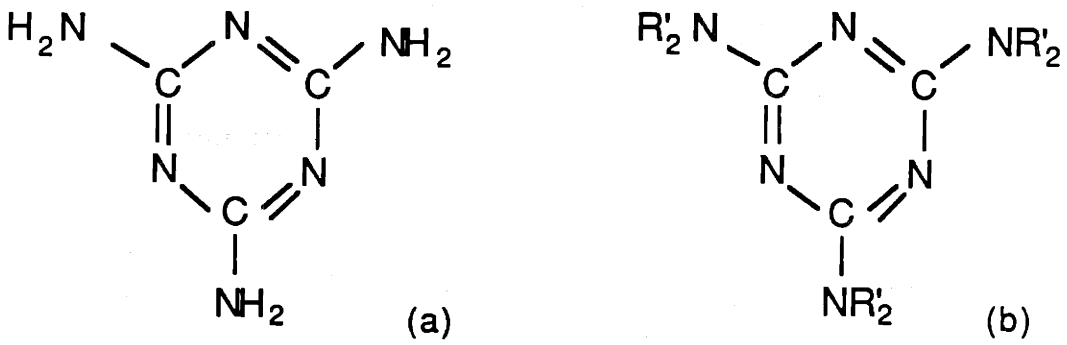

Figure 2.1 The chemical structures of melamine and melamine formaldehyde. (a) the structures of melamine; (b) the structure of melamine formaldehyde. In this particular coating (APC), the reaction between melamine and formaldehyde is complete. That is, R' is the $-CH_2OH$ group and there is no -H group.

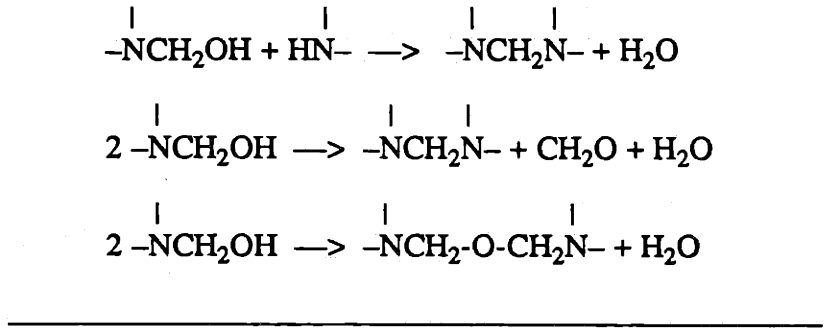

Figure 2.2 The possible polymerization mechanisms of melamine formaldehyde.

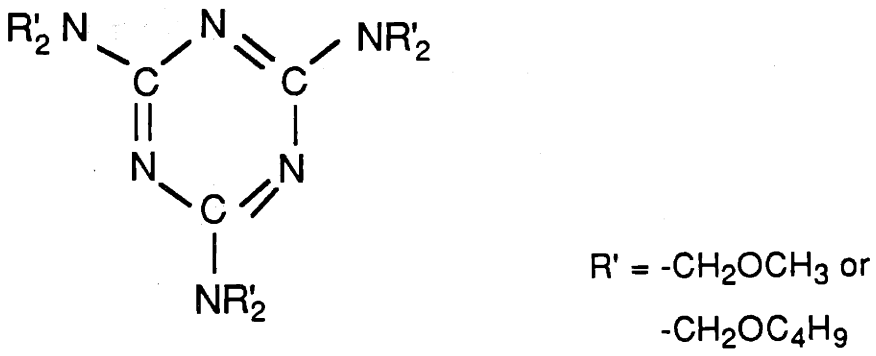

Figure 2.3 The chemical structures of methylated and butylated melamine formaldehyde. For the APC and APC-D coatings, the ratio of $-CH_2OCH_3$ group to $-CH_2OC_4H_9$ group is 1:1.

$$-NCH_2OR + HN- \longrightarrow -NCH_2N- + ROH$$

$$2\ -NCH_2OR + H_2O \longrightarrow -NCH_2N- + HCHO + 2\ ROH$$

$$2\ -NCH_2OR \longrightarrow -NCH_2N- + ROCH_2OR$$

$$-NCH_2OR + HOCH_2N- \longrightarrow -NCH_2OCH_2N- + ROH$$

$$-NCH_2OH + HOR'- \longrightarrow -NCH_2OR'- + H_2O$$

$$-NCH_2OR + HOR'- \longrightarrow -NCH_2OR'- + ROH$$

Figure 2.4 The possible crosslinking mechanisms of methylated/butylated melamine formaldehyde with acrylic polymer I. The R group stands for methyl and/or butyl groups. The –R'OH groups are the hydroxyl groups in acrylic polymer I.

2.2.2 Acrylic Polymer Coating With Dispersed Acrylic Resin

The second coating used in this study is also a finish coat on automobile and truck bodies. The ingredients of this coating is the same for the APC except for an extra component in this coating: a self stabilized dispersed acrylic resin. This coating is called acrylic polymer coating with dispersed resin (APC-D). The extra component, dispersed acrylic resin, is called acrylic polymer II. The procedure to produce this coating is typically as follows: (1) make the acrylic polymer I; (2) make the acrylic polymer II; (3) mix the acrylic polymer I and II with melamine formaldehyde crosslinking agents. The procedure to make acrylic polymer I and melamine formaldehyde crosslinking agents were described in the previous section.

Before producing acrylic polymer II, an acrylic polymer III has to be made first. The acrylic polymer III is polymerized in a solution and has about 52% solid content. The monomers for acrylic polymer III are shown in Table 2.3. The composition of acrylic polymer III by weight is about 15% styrene, 28% butyl methacrylate, 30% butyl acrylate, 10% hydroxy ethyl acrylate, 2% acrylic acid, 15% ethyl methacrylate. The weight-average molecular weight of acrylic polymer III is about 10,000. The acrylic polymer III is then mixed with other monomers and solvents for another polymerization. The solvents are mainly a mixture of xylene, butanol, heptane, isopropanol, and isobutanol. The monomers added to such polymerization are shown in Table 2.4. Note that two crosslinking reactions happened between the functional groups of monomers and acrylic polymer II. First, glycidyl methacrylate (in Table 2.4) reacts with the acrylic acid and hydroxyl groups in the acrylic polymer III (in Table 2.3). Second, the acidic groups of acrylic acid (in Table 2.3) reacts with hydroxyl group of hydroxy ethyl acrylate (in Tables 2.3 & 2.4). Hence, the

final product (acrylic polymer II) is a crosslinked gel-like polymer and has about 60% solid content. This polymer is called self stabilized dispersed resin.

Monomers	Structures
Styrene	$CH_2=CH-C_6H_5$
butyl methacrylate	$CH_2=C(CH_3)-COOC_4H_9$
ethyl methacrylate	$CH_2=C(CH_3)-COOC_2H_5$
butyl acrylate	$CH_2=CH-COOC_4H_9$
hydroxy ethyl acrylate	$CH_2=CH-COOC_2H_4OH$
acrylic acid	$CH_2=CH-COOH$

Table 2.3 The major monomers for making acrylic polymer III.

Monomers	Structures
methyl methacrylate	$CH_2=C(CH_3)-COOCH_3$
hydroxy ethyl acrylate	$CH_2=CH-COOC_2H_4OH$
Styrene	$CH_2=CH-C_6H_5$
methyl acrylate	$CH_2=CH-COOCH_3$
glycidyl methacrylate	$CH_2=C(CH_3)-COOCH_2\underset{\diagup\ \diagdown}{CH}-CH_2$ (O above CH)

Table 2.4 The monomers added to reacted with acrylic polymer III for making acrylic polymer II.

The acrylic polymer II is then mixed with acrylic polymer I, crosslinking agents, and solvents such as xylene, methanol, and methyl ethyl ketone. The mixing ratio (by weight) of acrylic polymer I: acrylic polymer II: melamine formaldehyde is about 4:1:2. The crosslinking mechanisms are similar to those shown in Fig. 2.4. The dodecylbenzene sulfonic acid is also added (less than 2% by weight) to the coating to increase the crosslinking rate during cure. The resulting coating has about 70% solid content.

2.2.3 Polyester Urethane Coating

The third type of coating is also a thermoset type of coating. This coating is a flexible finish and is applied to flexible substrates of automobile and truck bodies. It is called the branched aliphatic polyester urethane reacted with melamine formaldehyde crosslinker (PEU) [51]. The PEU is formed in three steps: (1) make a branched hydroxyl terminated polyester; (2) the branched polyester reacts with diisocyanates to form a polyester urethane; (3) mix the polyester urethane with melamine formaldehyde crosslinkers and acid catalyst. The solvent of this coating is a mixture of toluene, methanol, butanol, and other aromatic hydrocarbon solvents, since different solvents were added in those three steps.

In the first step, the branched hydroxyl terminated polyester was produced by a esterification of neopentyl glycol, trimethylol propane, dodecenedioic acid and azelaic acid. The chemical structures of monomers are shown in Table 2.5. The esterification is a reaction of two types of monomers: one has acidic functional groups, the other has hydroxyl functional groups. The mechanism is shown in Fig. 2.5a. To grow a branched polyester, monomers with more than two functional groups (either acidic or hydroxyl) are needed. In this particular coating, trimethylol propane (with three hydroxyl groups) was used to make a branched polyester. Figure 2.5b shows the reaction for the branched

polyester. To make a hydroxyl terminated polyester, excess hydroxyl groups were introduced to the esterification. The final product (hydroxyl terminated polyester) has a hydroxyl number of 110-250 and has an acid number of 1 or less.

Monomers	Structures
neopentyl glycol	$HOCH_2$-$CH(CH_2)_2$-CH_2OH
trimethylol propane	$HOCH_2$-$CH(CH_2OH)$-CH_2OH
dodecenedioic acid	HOOC-$(CH_2)_8$CH=CH-COOH
azelaic acid	HOOC-$(CH_2)_7$-COOH

Table 2.5 The major monomers for making the branched polyester.

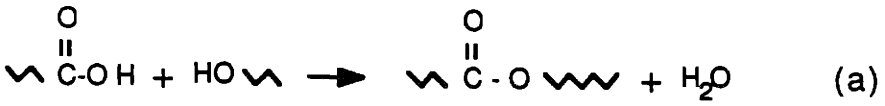

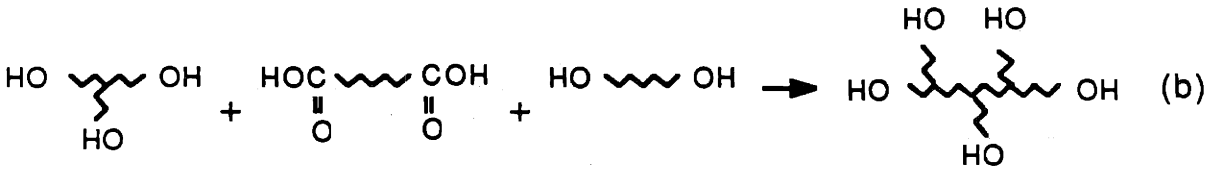

Figure 2.5 (a) Ester group is the basis of polyester chemistry; (b) The mechanism to form branched polyester.

Second, the polyester was then reacted with a 1:1 mixture of 2,2,4-trimethyl hexamethylene diisocyanate and 2,4,4-trimethyl hexamethylene diisocyanate (Fig. 2.6a) to form the polyester urethane. In this step, the hydroxyl groups of polyester reacted with the isocyanato groups to form the polyester urethane. The reaction to form the urethane group is shown in Fig. 2.6b. The final composition of the polyester urethane contains by weight about 32% neopentyl glycol, 4% trimethylol propane, 22% azelaic acid, 26% dodecanedioic acid and 16% trimethylol hexamethylene diisocyanates. It has a hydroxyl number about 60 and has a weight-average molecular weight about 15,000.

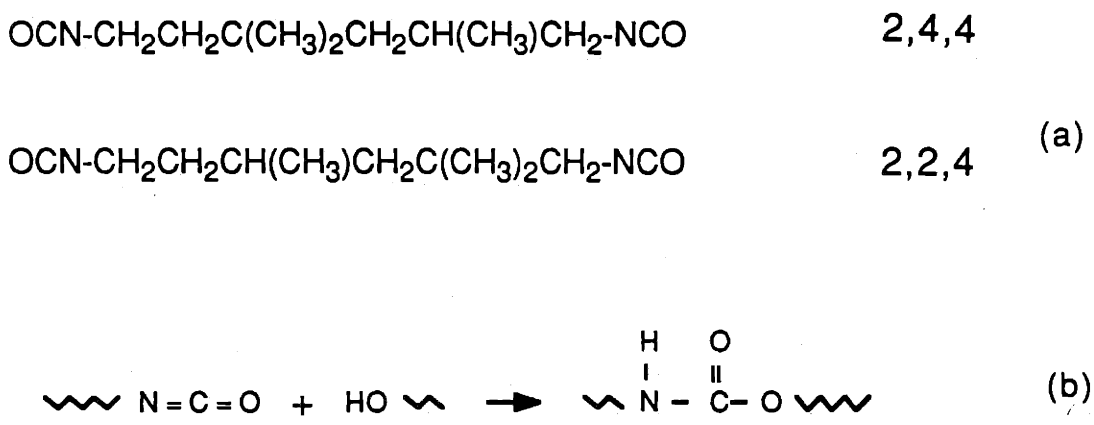

Figure 2.6 (a) The chemical structures of 2,2,4-trimethyl hexamethylene diisocyanate and 2,4,4-trimethyl hexamethylene diisocyanate; (b) Hydroxyl group reacted with isocyanato group to form urethane group.

The crosslinking agents (methylated and butylated melamine formaldehydes) used in the third step are similar to those in Section 2.2.1 (Fig. 2.1). However, the compositions of the functional groups of crosslinking agents are different. First, melamine reacts with formaldehyde to form melamine formaldehyde and the R groups in Fig. 2.1b

are the -H group (19%) and the -CH_2OH group (81%). Second, melamine formaldehyde reacts with methanol and butanol to form methylated and butylated melamine formaldehydes. The R groups of melamine formaldehyde (Fig. 2.3) are -H (19%), -CH_2OH (16%), -CH_2OCH_3 (16%) and -$CH_2OC_4H_9$ (33%). The mixing ratio (by weight) of polyester urethane to methylated/butylated melamine formaldehydes is about 5:9. The active functional groups for crosslinking are the hydroxyl groups of polyester urethane and the methylated and butylated methylol groups of melamine formaldehydes. The possible crosslinking mechanisms are similar to those shown in Figs. 2.2 and 2.4. An acid catalyst solution is added to the coating to increase the crosslinking rate. Solvents such as methanol, butanol and xylene are also added in this mixing process. The solid content of the final product is about 65% by weight.

2.2.4 Polyimides

Polyimide (PI) is a class of polymers which are from the condensation polymerization of dianhydride and diamine (Fig. 2.7a). Polyimide has very high thermal stability (typically maximum temperature is 400-450°C) and is not solvent extractable. In order to be easily processed, DuPont created a two-step polymerization for PI. In the first step, polyamic acid (PAA) is produced by the reaction of diamine and dianhydride in an appropriate solvent such as N-methylpyrrolidone (NMP). PAA (Fig. 2.7b) is soluble and can be deposited on wafers by the spin coating technique. In the second step, imidization occurs at a high temperature (usually above 200°C) and water molecules are generated from this reaction (Fig. 2.7c).

Polyimides were made by DuPont and were obtained in the form of PAA in NMP solvent. Figure 2.8 shows the diamines and dianhydrides of the PIs used in this work. These PIs contain benzophenonetetracarboxylic dianhydride (BTDA) and metaphenylene

diamine (MPDA) and oxydianiline (ODA). The first PI, BTDA-MPDA(20%)/ODA(80%), is known as DuPont Pyralin® 2555 and the second PI, BTDA-MPDA(40%)/ODA(60%), is known as Pyralin® 2525 [83]. These two PIs were chosen for their long linear elasticity regime up to about 2.5% [12]. BTDA-MPDA(20%)/ODA(80%) was used primarily in this study, while BTDA-MPDA(40%)/ODA(60%) was used only in the test of solvent effect (Section 2.3.3).

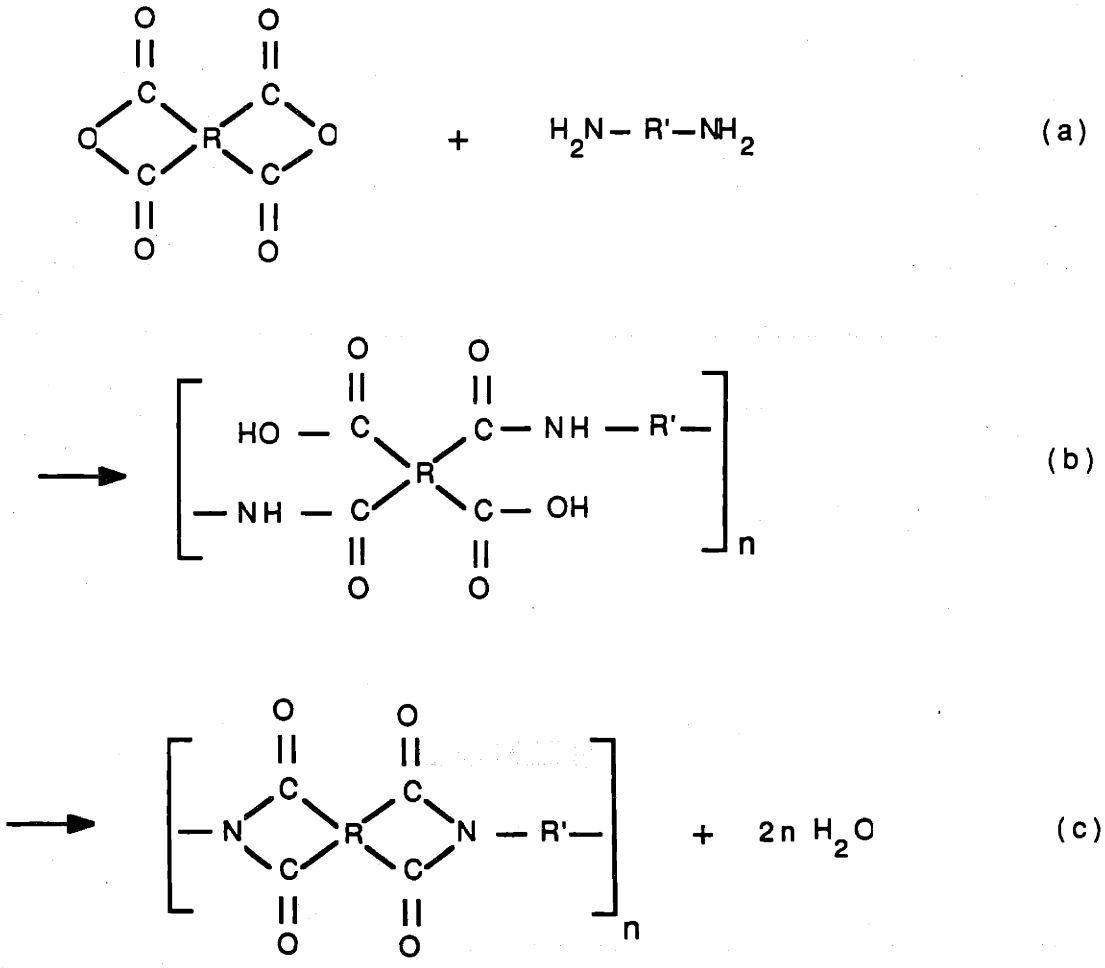

Figure 2.7 (a) Diamine and dianhydride (b) polyamic acid is formed; (b) polyimide and water are generated through imidization.

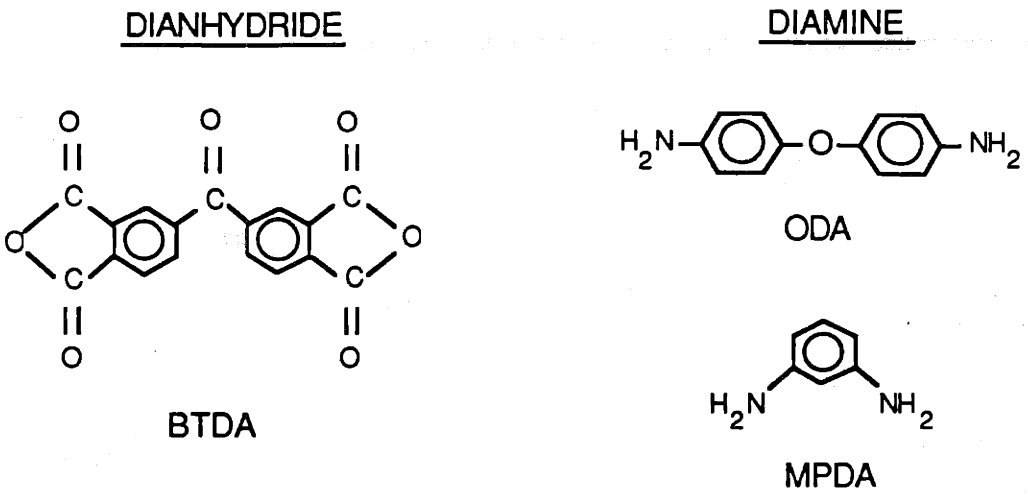

Figure 2.8 The chemical structure of dianhydride and diamine used in this work.

2.3 Fabrication of Square Samples

2.3.1 Single-layer Square Suspended Films

The process to fabricate single-layer PI square samples for the blister method is from Mehregany [49]. Figure 2.9 shows the schematic of the process. Two-inch <100> silicon wafers (either n-type or p-type) were the starting materials (Fig. 2.9a). The wafers were then subjected to a cleaning process such as RCA clean procedure to remove any organic and inorganic residues from surfaces. A heavily boron doped layer (p^+ Si) was formed onto the surface of Si wafers by a diffusion process (Fig. 2.9b). The boron was deposited from solid sources at a temperature of 1175°C for 3 hours in an environment of 10% oxygen and 90% nitrogen. Then approximately 1 μm silicon dioxide layer was grown (Fig. 2.9c) in an oxidation oven at 1100°C for 210 minutes (15 minutes in dry oxygen, 3 hours in steam and oxygen, 15 minutes in dry oxygen).

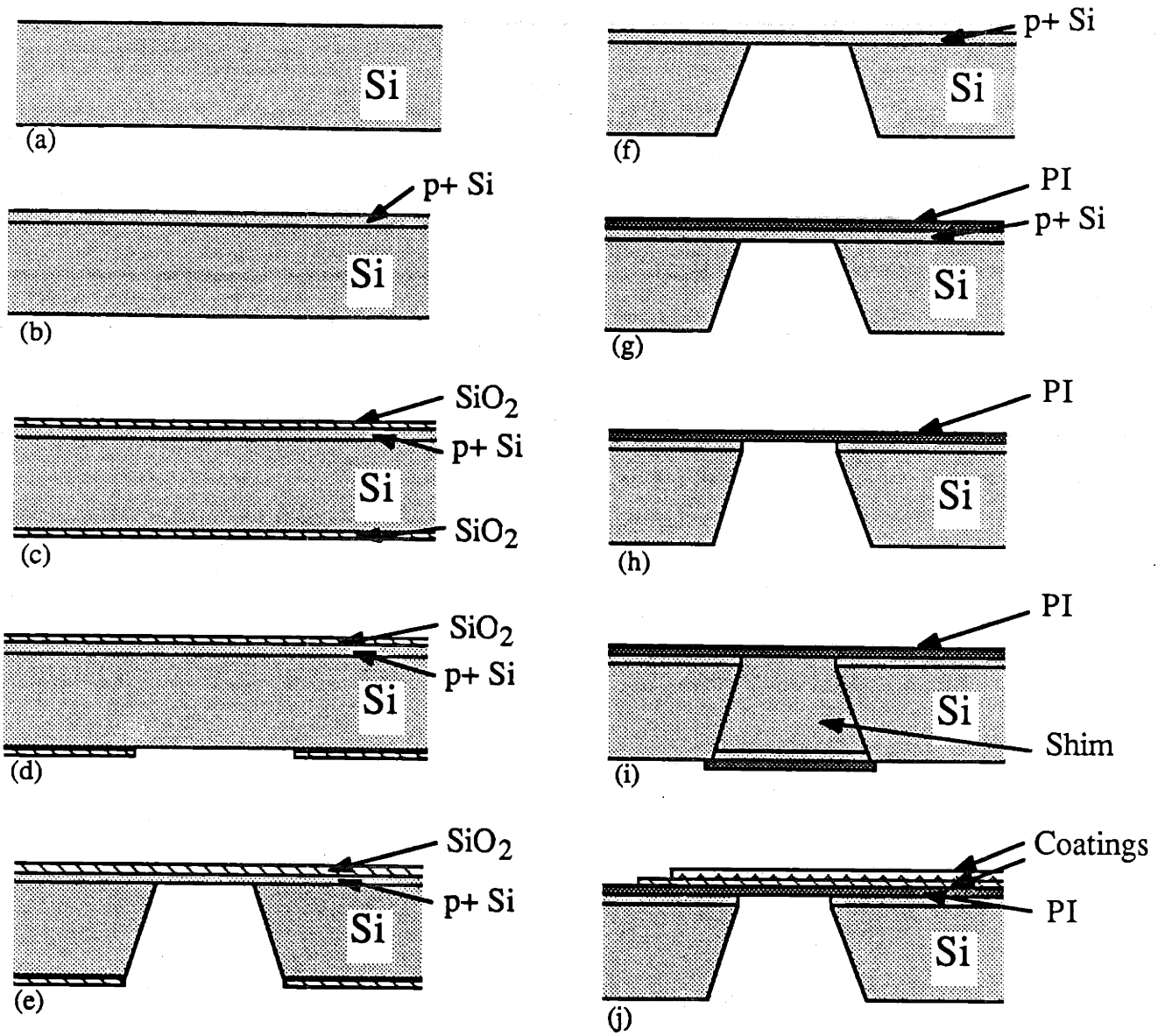

Figure 2.9 The fabrication of multi-layer square suspended films. (a) blank Si wafer; (b) boron deposition; (c) thermal oxidation; (d) photolithography to open a window on oxide; (e) anisotropic etching; (f) oxide removal; (g) polyimide deposition; (h) SF_6 plasma etching; (i) fabrication of supporting shim; (j) spray coated multi-layer paints.

A silicon oxide "window" was opened on the back side of the wafer by photolithographic techniques (Fig. 2.9d). Using an anisotropic etching on the <100> surface of silicon wafers, the edges of the window were created along <110> plane and the window resulted in a square or rectangle shape. This is because the etching rate in the <100> direction is the fastest comparing to the other directions. The wafer was then subjected to an etching solution which etches silicon fast but slows down at the p^+ Si layer (Fig. 2.9e). The etching was done in a 20% potassium hydroxide (KOH) aqueous solution at 50°C [54]. The etching time for a two-inch silicon wafer (about 250±25 μm in thickness) was typically 24-26 hours. A minimum of 6,000Å masking silicon oxide was needed in order to sustain KOH for such a long time. The etching time can be reduced to about 4 hours as the etching temperature is increased to 80°C. However, the faster etching rate gives a rougher surface on the p^+ silicon layer, which causes the difficulty of uniformly removing the p^+ Si layer in a later step. In addition, thicker silicon oxide (about 1 μm) is needed for etching at 80°C.

The silicon dioxide layer was removed afterwards using hydrofluoric acid (Fig. 2.9f). An adhesion promoter was spun on the wafers before PI was spun to increase the adhesion between PI and silicon. This adhesion promoter contained 0.5% γ-aminopropyltriethoxysiliane in methanol(95%)/water(5%) and was prepared 20 hours before usage. The polyamic acid was spun at 6000 rpm for 120 seconds. It was then baked at 130°C for 10 minutes to remove solvents and to start imidization. Additional coats were deposited and baked with the same procedure to make thick PI films. After two coats were deposited, the wafers were then cured at 400°C in a nitrogen environment for one hour to complete imidization (Fig. 2.9g). Finally, the boron doped layer is removed by sulfur hexafluoride (SF_6) plasma etching to form single-layer PI suspended films (Fig. 2.9h). Thickness of PI was about 4μm.

These samples either were glued to a lucite plate and were then ready for the blister test; or, were subjected to spray coating for making multi-layer samples (described in the next section). To glue the PI sample to a plate, the BIPAX® epoxy was used (#BB-F156, from Tra-con, Inc., Medford, Massachusetts). The epoxy was cured at room temperature for 24 hours.

The sizes of the square samples were determined in such a way that the working pressure range for the blister tests fell in the middle range of the pressure sensor. That is, the maximum pressure in the test should not be over or too close to the limit of the pressure sensor (5 psi, in this study) and nor should it fall into a very small pressure range (e.g. <0.1 psi) which would increase the error of pressure measurement. Hence, the size of samples were varied from 2.8x2.8mm to 5.3x5.3mm, depending on the number of layers and the thickness of samples.

2.3.2 Multi-layer Square Suspended Films

When PI single-layer suspended films were made, silicon shims were also fabricated in the other part of wafer (Fig. 2.10a). Each pair of shims and suspended films were fabricated from the same wafer since the variation of wafer thickness (±10%) from one wafer to another caused misfit between shims and holes under the PI suspended films. These shim structures were designed for supporting the PI film to sustain the high pressure from the spraying gun when paints are coated onto PI films. Spraying technique was selected in this study to deposit coatings because it is the method used to coat these paints in industry, and the spraying was carried out in the DuPont Marshall Laboratory. However, a few samples were coated by the spin technique and the difference in properties of the coatings was insignificant (Chapter 5). These two coating techniques (spinning and spraying) are discussed in Section 2.7.1.

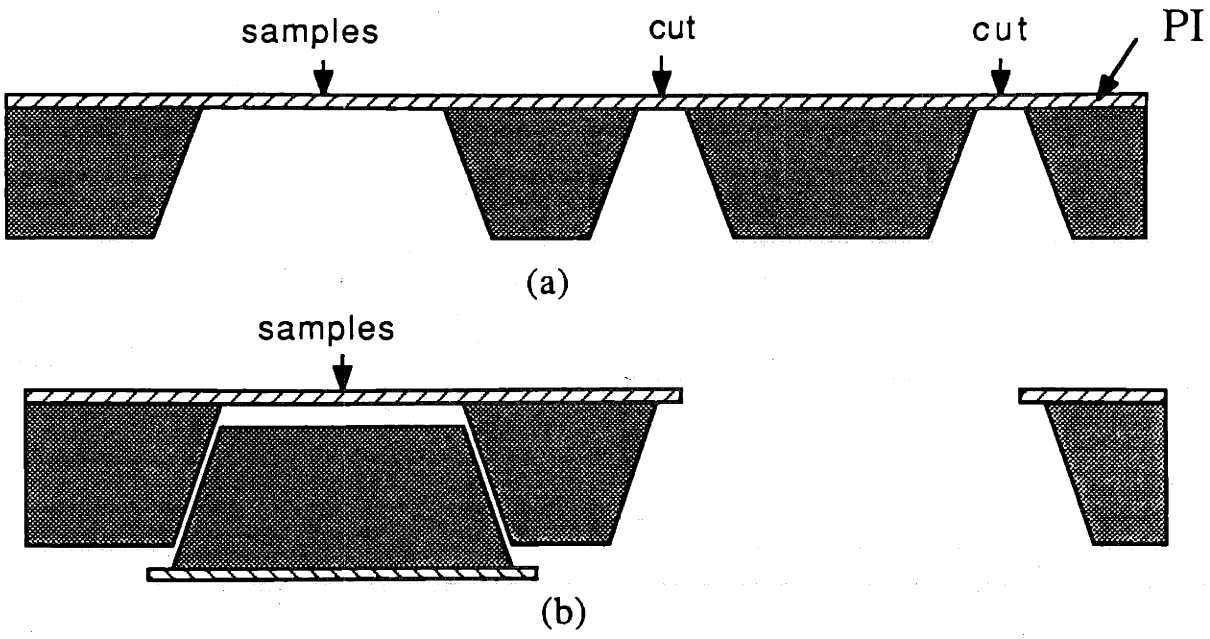

Figure 2.10 The fabrication of supporting shims. (a) cross-section of shim structure; (b) shim fills the entire space under the polyimide suspended film.

The anisotropic etching of silicon wafer resulted in a <111> plane. Therefore, the angles of the etching corners are always 54.74° (Fig. 2.10a). Hence, the shims created from the same wafer were in up-side-down positions; they were flipped over and fitted into the holes (Fig. 2.10b). The accuracy of shim sizes is precisely controlled by photolithography. Figure 2.11 shows photographs of a two-inch wafer with shims and suspended films. Note that the four corners of the shims were the convex corners of two <111> Si planes and were slightly etched away in the the KOH solution due to the higher accessibility of Si atoms at corners to the etchant. However, this did not affect the supporting function of the shim. The shims were then taped onto the back of the PI films (Fig. 2.9i).

The PI films with shims were then subjected to spray coating. After being sprayed, coatings were subjected to a cure process at 250°F for 30 minutes. The PI+coating two-layer suspended films were made after the curing step. The thickness of coatings was around 1-2 mil (25-50 μm). The samples were then subjected to this spraying and curing cycle for different coatings until all the designed layers were coated. The shims were removed afterwards. Figure 2.9j shows the schematic structure of the multi-layer suspended films. The multi-layer samples were then glued to lucite plates, as described in the previous section. Note that in the multi-layer samples there were masked regions, preserving areas of the original layer, to allow thickness measurements of subsequent layers. These measurements were taken by using a surface profilometer in a later step (Section 2.5).

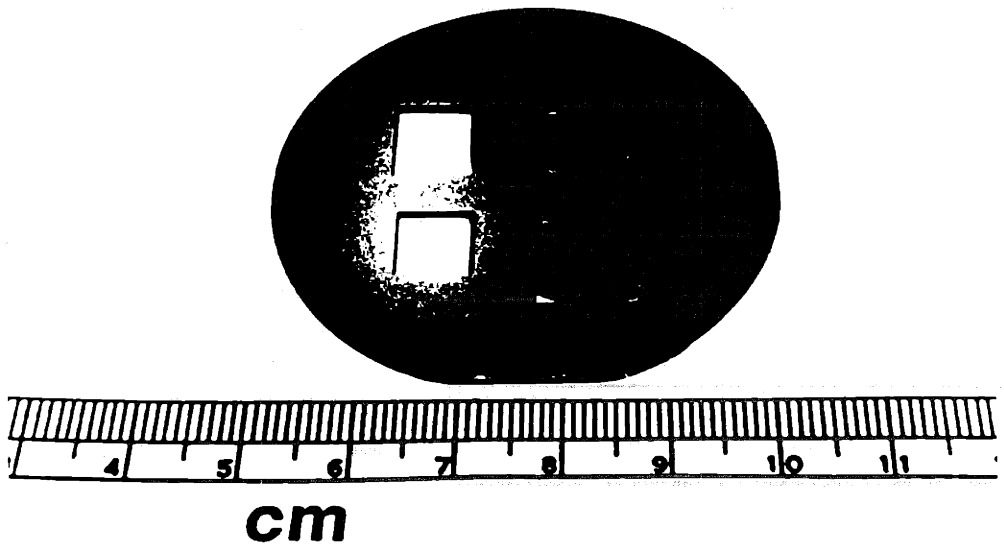

Figure 2.11 Photograph of a wafer with polyimide suspended films and the supporting shims.

As seen in Table 2.6, eight different types of layers were fabricated. As described, polyimide is always the bottom layer in multi-layer samples.

Number of Layers	Sample Types		
1	PI		
2	PI+APC,	PI+APC-D,	PI+PEU
3	PI+APC+APC-D,	PI+APC-D+PEU,	PI+PEU+APC
4	PI+APC+APC-D+PEU,	PI+PEU+APC+APC-D	

Table 2.6 Types of square single-layer and multi-layer samples

2.3.3 Solvent Effect

During the fabrication of multi-layer samples, a top-layer coating was sprayed onto an already-cured bottom-layer coating. That is, the bottom-layer coating was covered with a wet coating before the top-layer coating was fully cured. Whether or not the solvent molecules of top-layer diffused into the bottom layer and changed its mechanical properties is not known. The purpose of this test was to examine whether or not the solvent of the top layer affected the mechanical properties of the bottom layer. Hence, the procedure for this test was to compare the mechanical properties of samples with and without solvent treatment.

Polyimide single-layer samples were chosen for this test since PI is always the bottom layer. Two different polyimides were chosen for this experiment: BTDA-MPDA(20%)/ODA(80%) and BTDA-MPDA(40%)/ODA(60%). These five solvents:

xylene, heptane, methanol, butanol, and water were found in greatest amounts in the coatings and, therefore, were selected for this test. The blister test was used to measure the mechanical properties of PI.

The procedure of solvent treatment is as follows. The polyimide films, before being bonded to the lucite plates, were soaked in solvents for 30 minutes at room temperature. The films were then dried in a ventilated hood for three hours. Next, the samples were heated to remove the rest of the solvents in a 250°F oven for 30 minutes, mimicking the condition for curing paints. Then the PI samples were glued to the plates for blister tests. Six different wafers coated with BTDA-MPDA(20%)/ODA(80%) and five wafers coated with BTDA-MPDA(40%)/ODA(60%) were fabricated for this test. For each type of PI samples, one of the wafers was the standard (no solvent treatment) and the rest were individually treated with one of the five solvents.

2.4 Fabrication of Circular Samples

Circular suspended films have several advantages over square suspended films. First, there are no corners in circular films eliminating the problem of high stress concentration at corners. Hence, the deflection of films is not limited by material failure at corners. Second, the simplicity of circular geometry (axial symmetry) makes the mathematical analysis of mechanical behavior easier. This advantage is described in detail in both Chapters 3 and 4.

The process shown here is modified from the existing industrial method (coat-and-peel method) of sample preparation for free-film tensile tests. The schematic process is shown in Fig. 2.12. First, polyvinyl fluoride (PVF) films, (or Tedlar®, a trade name of DuPont) were wrapped and taped to steel panels (Fig. 2.12a). PVF was selected for its

low adhesion to the coatings used in this study. The coatings were then spray coated onto the PVF films and cured at 250°F for 30 minutes. This spray-cure cycle was repeated until all the desired coatings were deposited (Fig. 2.12b).

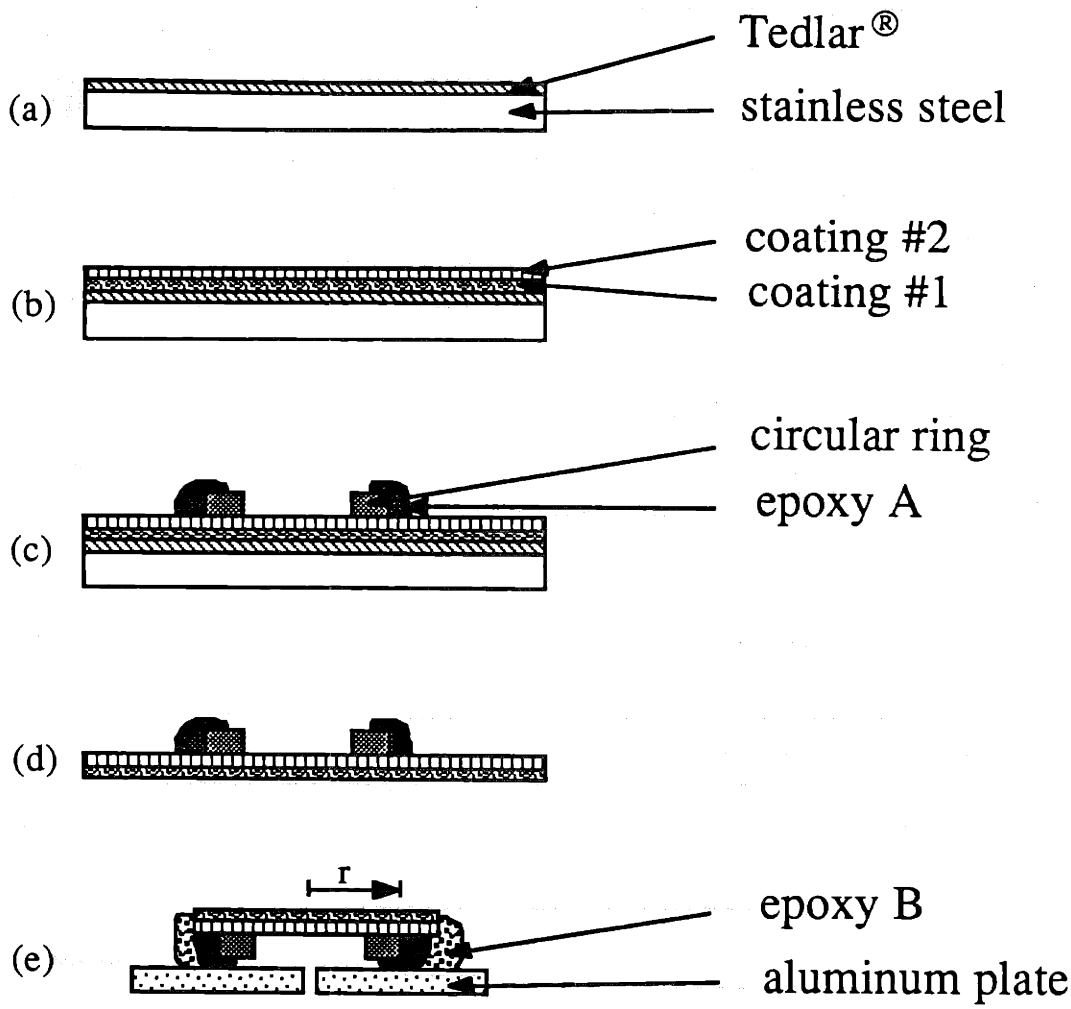

Figure 2.12 The fabrication of multi-layer circular suspended film. (a) Tedlar® wrapped steel panel; (b) spray coated multi-layer paints; (c) circular ring glued to the surface of the coating; (d) removal of Tedlar® and steel panel; (e) a mounted sample.

Metal rings, with the polished surface facing downward, were glued to the coatings using a gum-like epoxy (SM-100 Master Mend™ Epoxy, by Loctite Corporation, Cleveland, Ohio) (Fig. 2.12c). In principle, any circular rings can be used to obtain the circular shape for the coatings. In this work, inexpensive metal washers were chosen. These washers were polished by a series of sand papers (the finest grade was #600). The purpose of polishing the rings was to have sharp and clear boundaries around the rings so that the sizes of circular films can be precisely measured. The epoxy was pressed against the edge of the metal rings to have good contact between epoxy and rings. The epoxy was cured overnight at room temperature. There are several reasons for using this type of epoxy. First, this non-liquid epoxy does not diffuse into the interface of ring and coating. This makes a very clear edge and reduce the error of measuring the size of rings. Second, this epoxy has a high modulus and hardness so that when the films are deflected in the blister tests the boundaries of the films do not move. Third, the adhesion of this epoxy to both metal and plastics (polymers) is very strong.

After the rings were attached to the coatings, the PVF and coatings were untaped and separated from the steel panels. The PVF films were then peeled off the coatings (Fig. 2.12d). The ring and the coatings were flipped over and then glued (with BIPAX® epoxy) to an aluminum plate with a hole at its center (Fig. 2.12e). This BIPAX® epoxy is the same as that in Section 2.3.2. It was cured at room temperature for about 24 hours.

2.5 Thickness Measurement

There are two types of samples (one containing PI and the other without PI) for the mechanical tests. The fabrication processes of these two samples are different: samples containing PI were fabricated on Si substrates, while the samples without PI were made on

PVF films. Hence, the techniques used for measuring thickness of these two samples are different.

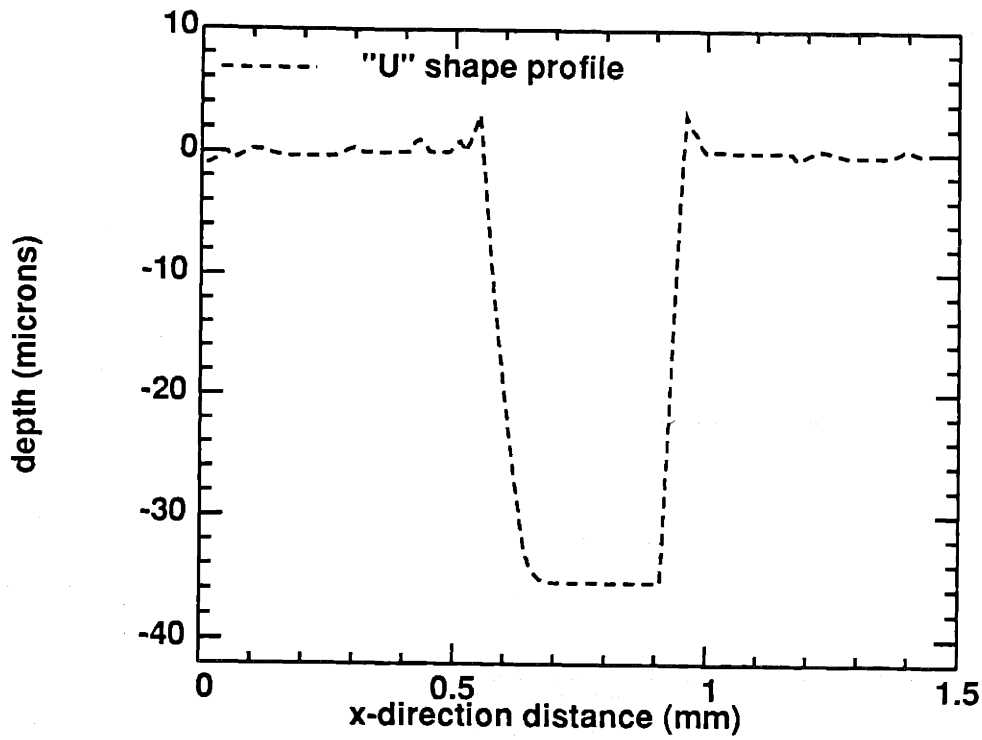

Figure 2.13 A "U" shaped profile for measuring the thickness of single-layer films using the surface profilometer.

First, a surface scanning profilometer (Dektak®) was used for measuring the thickness of polyimide and each layer of coatings on Si substrates. Two typical scanning profiles are shown in Figs. 2.13 and 2.14. The films were scratched on the Si wafer and the surface profile was "U" shaped (Fig. 2.13). For single-layer PI samples, the depth of the "U" profile is the PI thickness. However, for multi-layer samples, the measurement

only gives the overall thickness of films since the scratch went through all layers. Therefore, the other profile, a step profile (Fig. 2.14), had to be used for the thickness of each layer in multi-layer samples. This profile was obtained from scanning across the boundary between the masked and unmasked regions (Fig. 2.9j). The thickness of the individual layer was calculated from the height between two steps of the profile. The profilometer was calibrated using both 1μm and 10μm standards and the accuracy was within 1%. The maximum thickness that can be measured by this profilometer is 60μm.

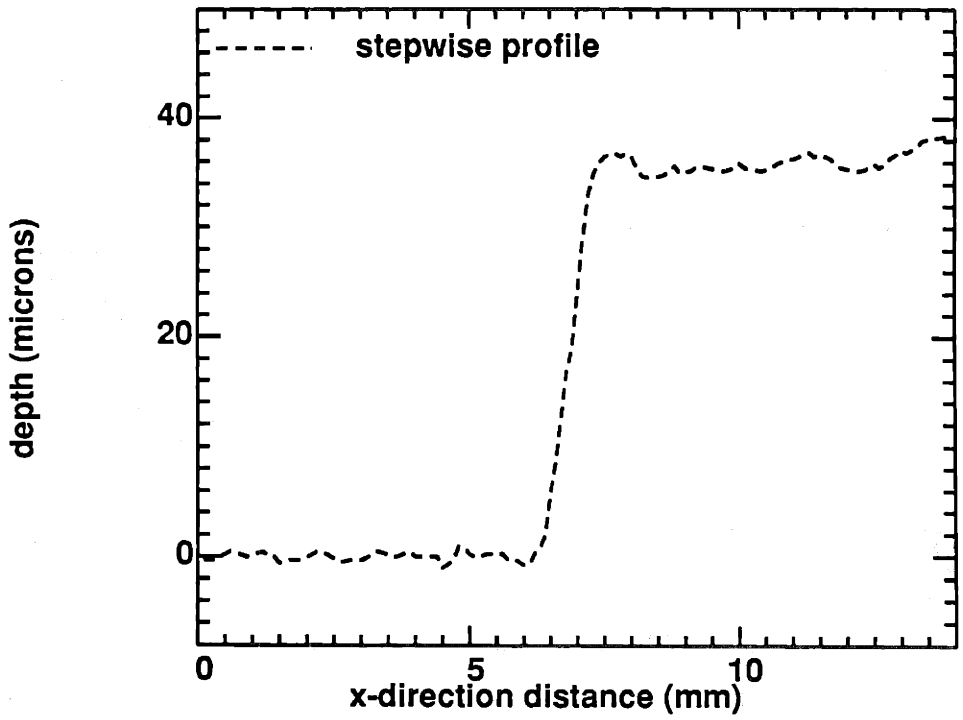

Figure 2.14 A step profile for measuring the thickness of multi-layer films using the surface profilometer.

The second type of instrument for the thickness measurement was a Mitutoyo digimatic indicator (ID-110ME). This micrometer-type instrument can be used to measure thickness up to 10mm with a resolution of ±1μm. The coatings were released from the PVF films first and the thickness was measured from a free film. The disadvantage of this measurement was that only the overall thickness can be measured. Thus, to know the thickness of each layer, the thickness of one film can be subtracted from the thickness of another film. For example, the thickness of the top layer (in a bi-layer film) can be calculated by subtracting the single-layer (bottom-layer) thickness from the bi-layer thickness. Similar subtraction can be done for three-layer films.

Thickness of coatings, especially the spray coated films, was not uniform across a wafer. Variation of thickness measurements will be discussed in Chapter 5. The problem of thickness nonuniformity in spray coated films affects accuracy in the evaluation of the mechanical properties of the coatings.

2.6 Blister Tests

2.6.1 Measurement Setup

A setup for the measurement of film deflection as a function of applied pressure for the blister method was established by Allen [47] and has been modified by Pan [55]. In the setup, a suspended film sample was clamped in a sample chamber (Fig. 2.15). The sample chamber was assembled from three pieces: the viewing plate (3 inch diameter x 1/16 inch thick), the clamping plate, and the pressure-inlet plate (4x4x0.5 inch for both). The viewing plate contained a microscope cover glass (45x50x0.15mm). The big size of the cover glass made the whole sample visible from the top of the chamber so that the center of the films were easily determined. The clamping plate was used to clamp the sample to the

o-ring at the center of the pressure-inlet plate. The pressure, from a compressed air source, was applied to the sample through the hole inside the o-ring.

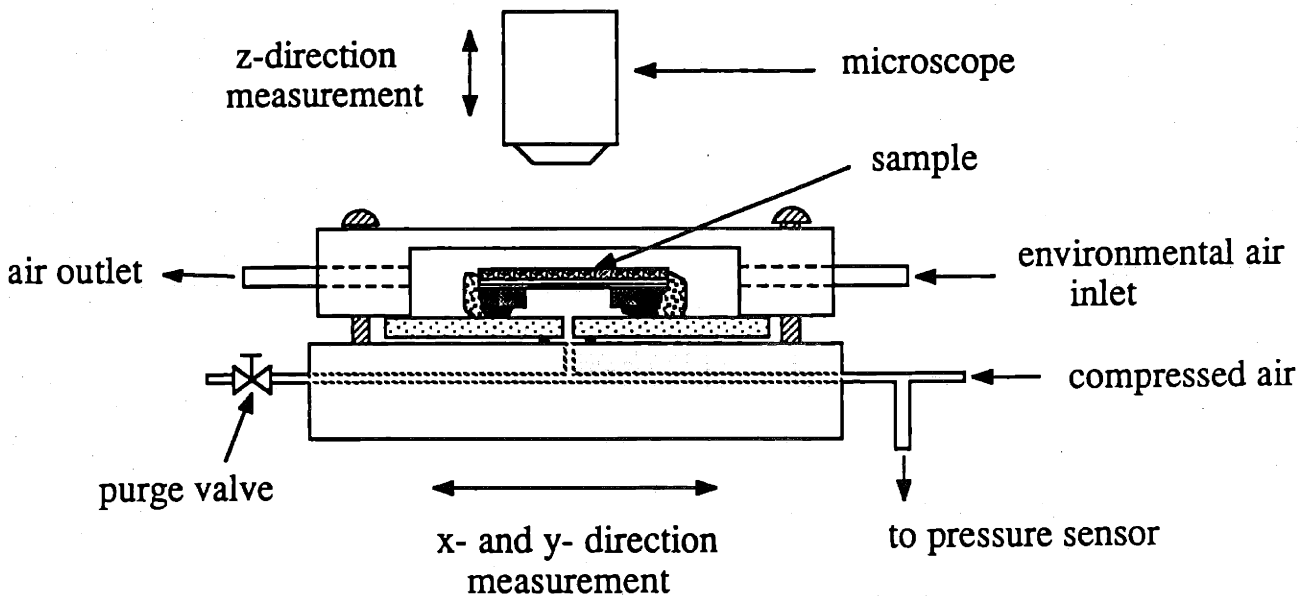

Figure 2.15 The cross-section of sample chamber. The environmental air flows over the top of the sample; the sample is deflected by pressure air from the bottom.

The pressure sensor was a differential pressure sensor (Model 142PC05G, maximum pressure 5 psi, by Honeywell) and was placed outside the pressure-inlet plate. Eight volts were supplied to the pressure sensor (by an HP 6114A precision power supply). A voltmeter was used to detect the output voltage from the pressure sensor and was interfaced to an IBM AT personal computer using an IEEE-488 parallel bus. The pressure sensor was calibrated by both water and mercury manometers.

Film deflection was measured as the vertical distance the microscope lens had to be adjusted to keep the film in focus from flat film state to bulged film state. This distance was measured by a built-in Mitutoyo digimatic indicator (ID-150ME). This indicator can measure distance up to 50 mm. It was checked against the standard blocks and other calibrated micrometers and showed good accuracy ($\pm 1\mu m$).

To measure deflection, the entire sample chamber as well as the sample itself was seated under a microscope (Nikon Measurescope UM-2). This microscope had a large space (five inches in vertical direction) for this purpose. Two special requirements were also needed for microscope lens. First, the object lens must have high numerical aperture (N. A.=0.5 here) for sufficient working distance for covering the sample with the sample chamber. The working distance of the lens was 9.8 mm. Second, the lens must have a small depth-of-field (less than $1\mu m$) for accuracy in focusing the film. These two requirements were included in this set-up. In addition, two micrometers in x- and y-direction were built on the microscope stages for measuring the size of the samples. The readout of these micrometers was linked to a computing system (QUADRA-CHEK II, by Metronics) capable of calculating the center of the film by input of points. Figure 2.16 shows the photograph of the microscope setup for the blister test.

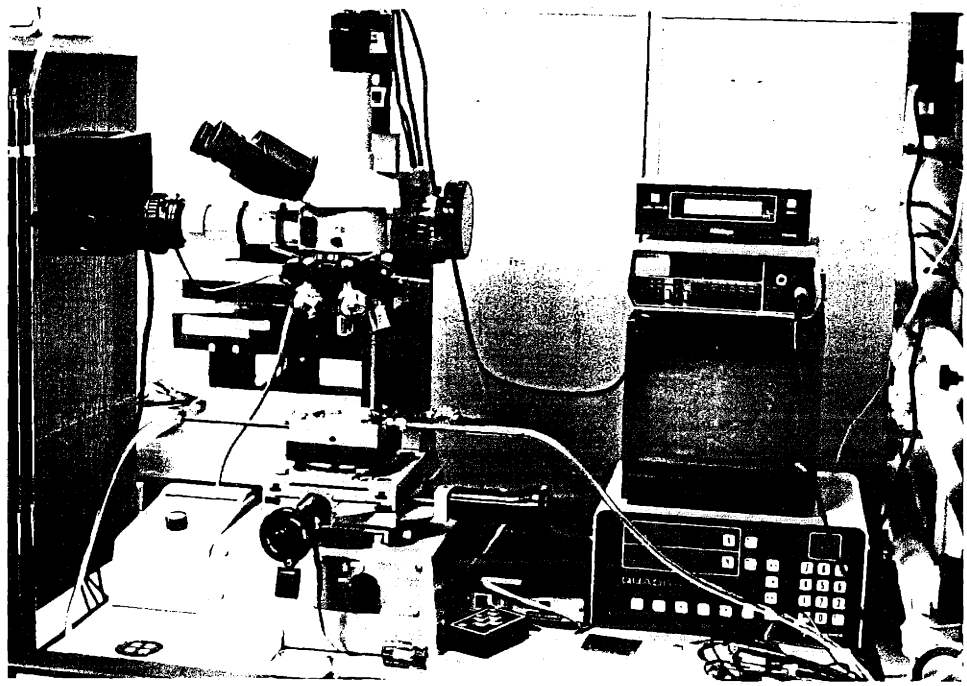

Figure 2.16 The photograph of the measurement setup for the blister test.

2.6.2 Humidity Control

Humidity control of the environment in the blister test is described in this section. A moisture generating system, which can deliver air with constant relative humidity (RH), has been built by Mario [56] and Pan [55]. Figure 2.17 shows the schematic of the system. A dry compressed air (about 100 psi) was the source for the system and was branched into two streams: one stayed dry and the other was humidified. The humid air was formed by letting dry air pass through a saturator. The humid air was then mixed with the dry air and the dew point of the air mixture was detected using a thermoelectrically-cooled optically-sensed condensation dew point hygrometer (General Eastern Model

1200AP). The RH was then calculated by dividing the saturated vapor pressure at dew point with the saturated vapor pressure at the ambient temperature. The RH of the moistened air was controlled by adjusting the flow rates of both dry and humid streams. Figure 2.18 shows both environmental air and pressure inlets of the sample chamber.

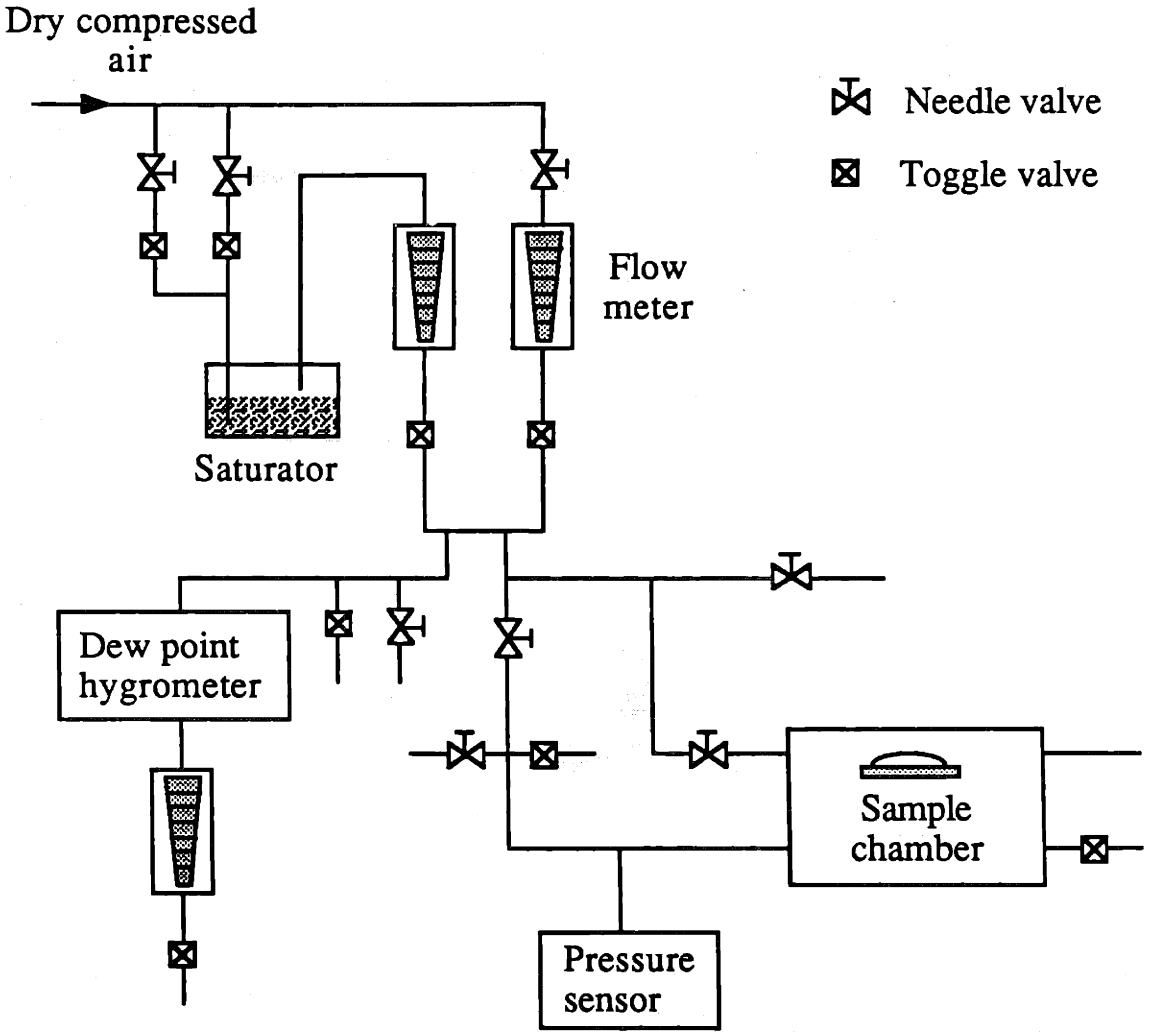

Figure 2.17 Schematic of the moistened compressed air system.

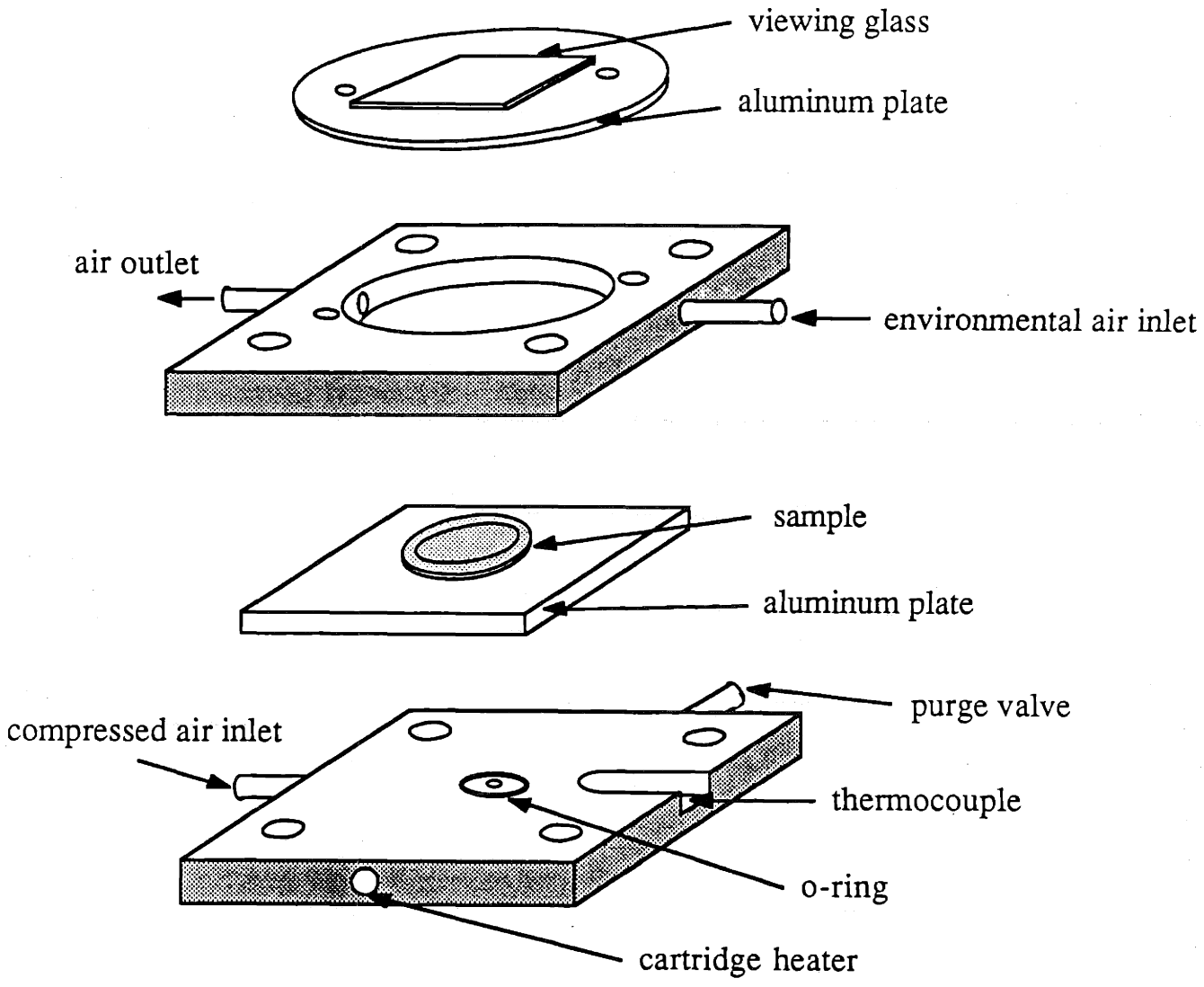

Figure 2.18 Exploded view of the test chuck with a sample.

Before being connected to the sample chamber, the moistened air was separated into two streams: one (environmental air) went to the clamping plate to keep the whole chamber at a certain humidity, and the other (pressure air) went to the pressure-inlet plate to supply pressure for the blister test. The pressure applied to the sample was adjusted using a needle valve.

2.6.3 Experimental Procedure

All the blister tests were regularly performed at room temperature (about 23°C) and room humidity (about 50% RH) except for those tests under humidity control. In the regular tests, dry compressed air was used as the pressure source and the sample was left open to the atmosphere. After the sample was placed in the sample chamber, the center of the film was determined by x- and y-micrometer and QUADRA-CHEK II. The magnification of the lens was 400x (10x for the eye piece and 40x for the object lens).

In each test, about 15-20 measurements were taken. The values of film deflection were recorded when pressure was increased incrementally until "maximum" deflection was reached. The maximum deflection was determined in such a way that the overall strain did not exceed 0.5% (e.g. about 400μm for 5x5mm, 310 μm for 4x4mm, etc.). Film deflection was set at zero before each test and the deflection after the test was recorded as an indication of the margin of error in deflection measurement. This margin of error was about 3-4 μm in average.

In tests of humidity control, the sample was placed in the sample chamber as mentioned in the previous section. The humidity of the air supply was controlled by adjusting the flow rates of dry and humid air. The flow rate of the environmental air (to the clamping plate) was set at 2 SCFH (standard cubic foot per hour). The purge valve in the

pressure plate was opened so that the existing air could be purged and the moistened air could surround the sample. The sample was kept in moistened condition for 90 minutes before performing the test. The test started from dry air (around 0% RH) and after that, the RH was increased by 20% incrementally up to 60%.

2.7 Uniaxial Tensile Tests

There were two types of samples used in the uniaxial tensile tests: (1) single-layer PI and multi-layer PI+coating samples, which were fabricated using microelectronic techniques; (2) single-layer paint samples (no PI), which were made using the coat-and-peel method.

In order to compare results of the tensile tests with blister tests, the tensile test samples were made using the same technique as the blister test samples since different sample preparation may change the film quality and properties. The method to fabricate PI films for tensile test using microelectronic techniques was first developed by Maseeh [17]. This method was slightly modified to fabricate multi-layer PI+coating samples.

2.7.1 Sample Preparation by Microelectronic Fabrication

The samples made by microelectronic fabrication were PI single-layers and PI+coating bi-layers. These samples were made on Si wafers. The procedure can be divided into two steps: (1) make PI and PI+coating suspended films; (2) fabricate ribbon shape samples from suspended films using oxygen plasma etching.

The first step was similar to the above-mentioned method (Sections 2.3.1 and 2.3.2). However, the differences are three-fold. First, the shape of suspended films used in this section was rectangular instead of square. Second, the size (0.8x1.0inch) was

bigger. Third, the paints were deposited onto PI suspended films by spin coating instead of spraying for making multi-layer samples.

The spinning was carried out in a glove box purged with dry air. The thickness of films can be varied by adjusting the speed of spinning. The relationship between the thickness of coatings and spinning speed is shown in Fig. 2.19. Before spinning, the coatings were filtered using filters attached to a syringe since dust particles inside the coatings leave marks on the surface after spinning. The filters for APC and PEU were Acrodisc® filters with 1μm pore size (Gelman Sciences, Ann Arbor, Michigan). The filters for APC-D was Millex®-LS filter with 5μm pore size (Millipore Corporation, Bedford, Massachusetts) since micro-gel in APC-D coating needs larger pore size.

The second step was to make ribbon shape PI and PI+coatings films. Figure 2.20 shows the schematic process of this step. The PI and PI+coatings suspended films were made as mentioned above (Fig. 2.20a). An "I" shaped Si mask (Fig. 2.20b) was made by photolithography and anisotropic etching of an Si wafer (Section 2.3.1, see Figs. 2.9a-e). This mask was then placed on top of the PI or PI+coatings suspended films (Fig. 2.20c). An aluminum plate and six bent beams were used to press the mask to the suspended films to prevent gapping between the mask and the film during the plasma etching (Fig. 2.20d). The photograph of the aluminum plate and the sample is shown in Fig. 2.21. The whole plate was then subjected to oxygen plasma etching to etch away PI and/or paints. The mask was then removed after etching (Fig. 2.20e). The wafer was broken according to the back side grooves made by anisotropic etching (Fig. 2.20f). This resulted in ribbon-shaped PI or PI+coatings samples (Fig. 2.20g). The photograph of the sample is shown in Fig. 2.22.

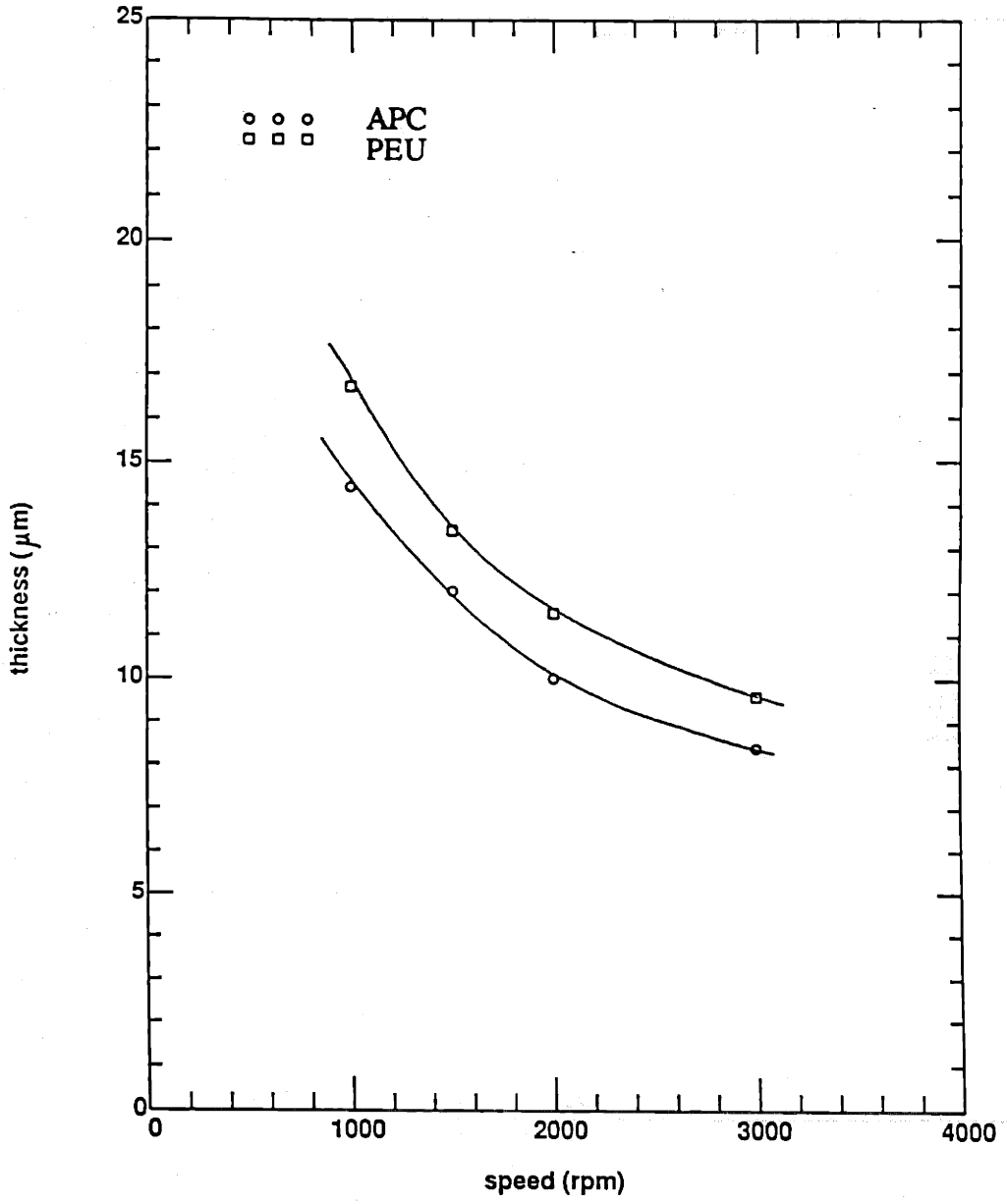

Figure 2.19 The cured coating thickness versus the spinning speed.

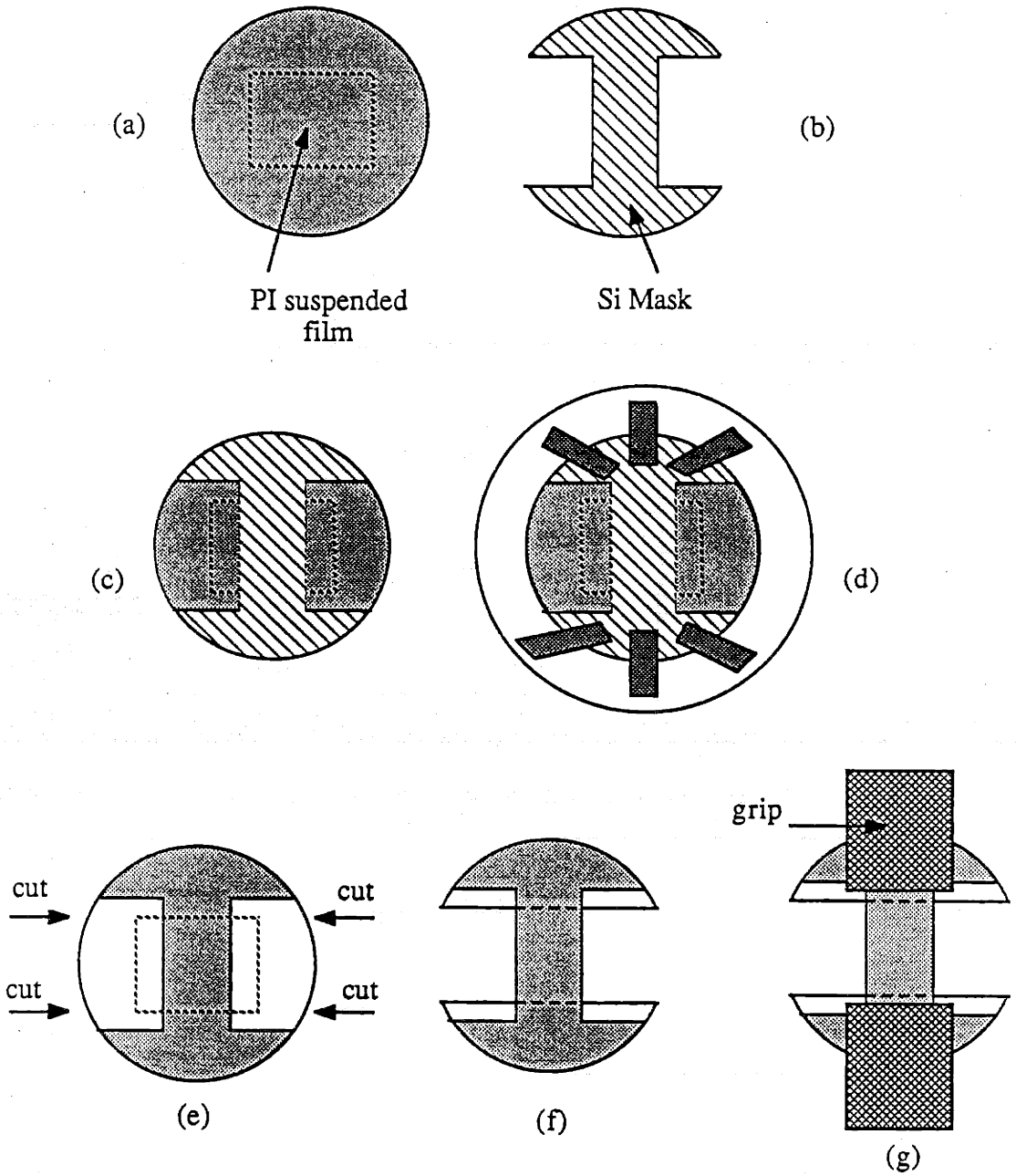

Figure 2.20 The fabrication of tensile test samples. (a) the PI or PI/paints suspended film; (b) the "I" shaped Si mask; (c) mask on top of suspended film; (d) mask and film clamped on aluminum plate; (e) removal of mask; (f) breaking wafer; (g) ribbon-shaped sample.

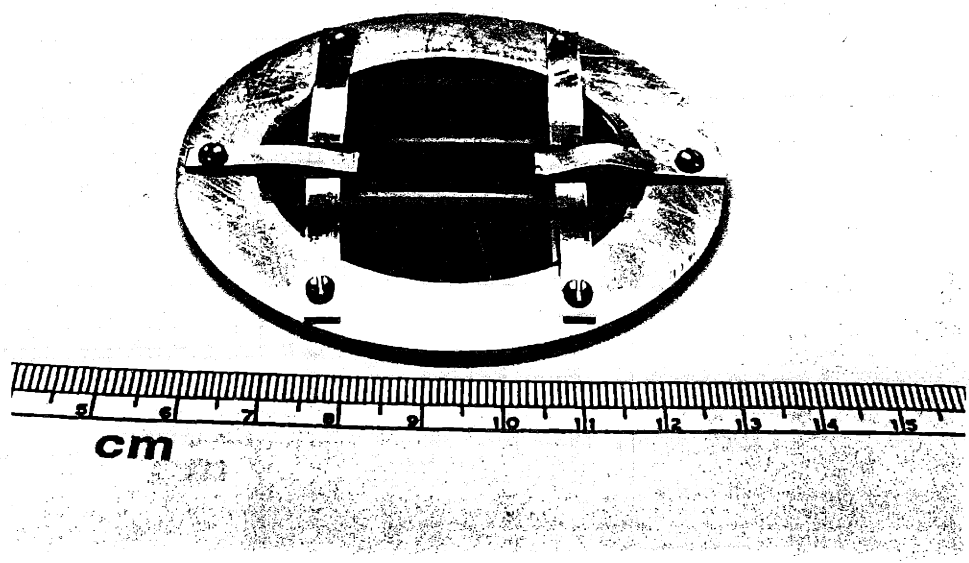

Figure 2.21 The photograph of the aluminum plate and the sample.

The advantage of this method of fabrication is that both samples of the blister test and the tensile test are made using the fabrication technique (microelectronic fabrication) so that the results of both experiments are comparable. In addition, films are fairly uniform and the dimension of samples are well controlled (by the mask). However, the disadvantages are four-fold. First, the sample preparation needs tremendous caution since the films are very delicate. Second, the sample fabrication time is very long (about 4-5 hours for each sample) even though the Si mask is re-usable. Third, both ends of the ribbon are constrained on the Si wafer, which introduces internal stress and potential cracking at both ends resulting in premature breakage in the tensile test. Forth, the maximum thickness of coatings that can be deposited is limited. That is, the high spinning

speed gives the uniformity of the thickness but also reduces the thickness. To make a regular 1 mil (25μm) thick coatings, a spin-cure cycle has to be repeated many times (like the case of PI).

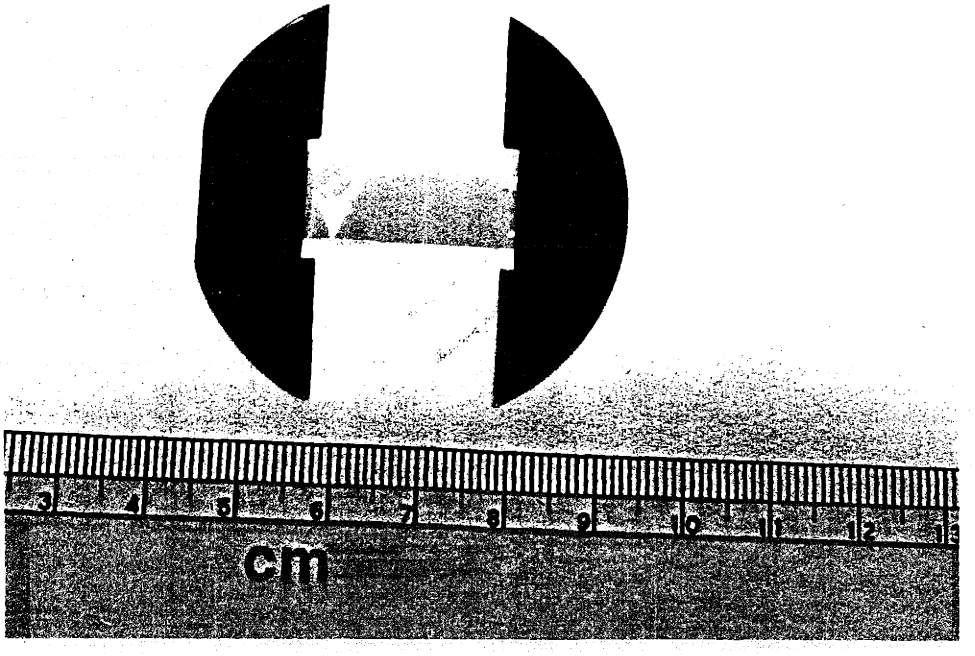

Figure 2.22 The photograph of the uniaxial test sample fabricated using microelectronic techniques.

2.7.2 Sample Preparation by Coat-and-Peel Method

The samples fabricated by this method contain no PI. This method is similar to that described in Section 2.4. The coatings were sprayed onto a steel panel wrapped with PVF film. The coatings were then cured at 250°F for 30 minutes. This procedure was repeated until all the desired coatings were deposited and cured. The PVF with coatings was then untaped and separated from the steel panel. The films were cut into strips (1x8 cm) using a

sharp surgical blade (Bard-Parker™ #11, Becton Dickinson and Company, Lincoln Park, New Jersey). This cutting tool is especially useful for cutting brittle films to prevent chipping at the edges.

The PVF were then peeled off. The coating strips were placed in a pre-cut heavy-weight paper frame with a distance of one-inch between the inner edges (Fig. 2.23). The strip of coatings was taped onto the paper frame widthwise. Thus, the sample length for the tensile test is always one inch and the width is one centimeter.

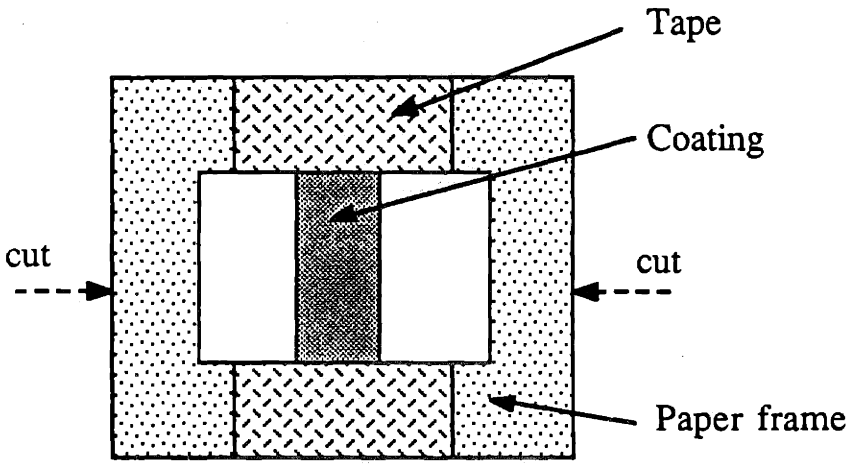

Figure 2.23 The schematic picture of the uniaxial test sample fabricated using free films and paper frames.

2.7.3 Measurement Setup

The uniaxial tensile tests were carried out using an Instron (model 1122) with a 2000-gram capacity load cell. Pneumatic grips were used to hold samples (the pressure used was 60 psi). The film samples (taped on the paper frames) were mounted between grips and then the frame edges were cut. The gauge length of the films was one inch and the strain was determined from the cross-head displacement. The cross-head speed was 0.05 mm/min (or 0.2%/min) for the APC and APC-D, and was 0.5 mm/min (or 2%/min) for PEU. All tests were performed at room temperature.

The results (load versus elongation) were collected on a chart recorder. The strain was calculated by dividing the elongation with gauge length and the stress was calculated by dividing the load with the cross section area of the sample strips. The Young's modulus was calculated as the slope of the initial linear region of the load versus elongation plot.

CHAPTER 3

Analytic Theory For Film Deflection

3.1 Introduction

In this chapter the analytical single-layer and multi-layer models for the load-deflection behavior (the relationship between applied pressure and deflection) of suspended films are developed. The purpose for this analysis is to find the functional form of the relationship between pressure and deflection in blister tests. That is, the analytic solution provides formulas for the relationship and the constants in the formulas are then determined (Chapter 4) by finite element method (FEM), since FEM provides more accurate deformed shapes.

Two different geometries of films are discussed here: circular and square shapes. To start theoretical analysis, the displacement fields of deformed films are assumed. The corresponding strain energy is then calculated and is subjected to an energy minimization approach. In Section 3.2, the single-layer models for circular films are derived. Two types of single-layer models are discussed: one, is the thin-film model and the other, is the thick-film model. In the thin-film model, membrane-like behavior is assumed. That is, the bending effect at the edge of the deformed films is neglected. However, as the films get thicker, the bending effect has to be considered; the model including this effect is then called the thick-film model. Similar models are also developed for single-layer square films in Section 3.3.

In Section 3.4, the multi-layer models of square membranes are developed. For the case of multi-layer structures, the total strain energy is found by adding up the strain energy of each layer. Then the total strain energy is subjected to energy minimization which is the same as that used for single-layer models. There are also two models for multi-layer structures. The first one is based on the thin-film single-layer model; that is, each layer in the multi-layer structure behaves like the membrane in the thin-film model. The second multi-layer model assumes that the mechanical behavior of every layer is based on the thick-film behavior. The results of single-layer models (in Sections 3.2 and 3.3) show that the relationship between pressure and deflection for square and circular films are very similar except for the constants. Therefore, the multi-layer models for circular films are not derived in this chapter; however, the constants for circular multi-layer models will be calculated in the next chapter.

3.2 Circular Films

3.2.1 The Beams' Equation

A mechanical model for deflection of circular thin film has been developed by Beams [6]. A typical cross-section of a deflected film under lateral pressure is shown in Fig. 3.1. In Beams' equation, the relationship between pressure P and stress T is assumed first that

$$P = \frac{4tT}{a^2} d \tag{3.1}$$

where T is stress along the plane of membranes, d is deflection, a is radius of membranes, and t is thickness, and P is pressure. The stress T is a sum of the stretching stress and the residual stress:

$$T = \frac{E}{1-\nu}\varepsilon + \sigma_o \tag{3.2}$$

where ε is the average strain of the membrane, E is Young's modulus, ν is in-plane Poisson ratio, and σ_o is residual stress. Substitution of Eq. 3.2 into Eq. 3.1 gives

$$\frac{Pa^2}{td} = \left(\frac{4E}{1-\nu}\right)\varepsilon + 4\,\sigma_o \tag{3.3}$$

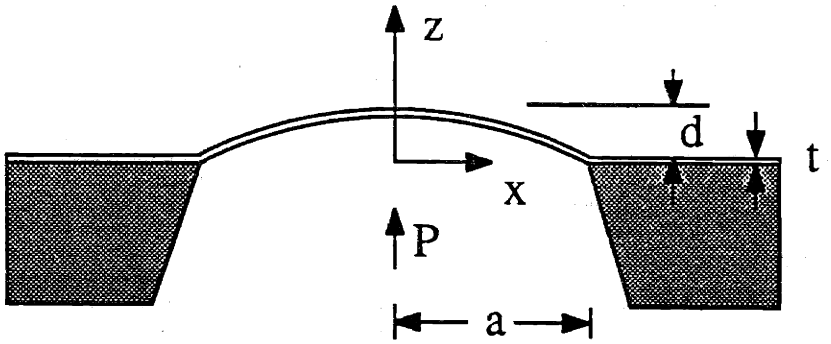

Figure 3.1 Cross-section of a suspended film undergoing a center deflection d at an applied pressure P. The half-size/radius of the film is a and the thickness is t.

By definition, the average strain of membrane can be expressed as

$$\varepsilon = \frac{R\theta - a}{a} = \frac{R\theta}{a} - 1 \tag{3.4}$$

where $R\theta$ can be approximated by

$$R\theta = R\,\sin^{-1}\left(\frac{a}{R}\right) \approx a\left(1 + \frac{a^2}{6R^2}\right) \tag{3.5}$$

The value of R can be calculated by:

$$R = \frac{a^2}{2d} + \frac{d}{2} \tag{3.6}$$

where a is the radius of the membrane. When the curvature R is much greater than the deflection d, the value of $d/2$ can be neglected in Eq.3.6 and R is approximately equal to $a^2/2d$. By substituting Eq. 3.5 into Eq. 3.4 and with the approximation of $R \approx a^2/2d$, the average strain is then given by

$$\varepsilon = \frac{2d^2}{3a^2} \ . \tag{3.7}$$

By substituting Eq. 3.7 into Eq. 3.3, the final form of Beams' equation is written

$$\frac{Pa^2}{td} = C_2 \frac{1}{a^2}\left(\frac{E}{1-\nu}\right)d^2 + C_1 \sigma_o \tag{3.8}$$

where $C_2 = 8/3$ and $C_1 = 4$. Further discussion of Eq. 3.8 is given in Section 3.2.3.

3.2.2 Thin-Film Model

In this section, an energy minimization approach for thin film deflection is introduced. Several assumptions are made in this mechanical analysis of film deflection. First, it is assumed that the thickness of film is very small compared to the size of diaphragms. In this study, the ratios of thickness-to-length for a single-layer circular membrane are in the order of magnitude of 0.01, in which case, the assumption of thin film is reasonable. The bending energy of the deflected membrane is neglected under this assumption. The model generated in this section is called thin-film model. In case of thicker films, this assumption may not be appropriate and the so-called thick-film model is further discussed in Section 3.2.3.

Second, plane stress is assumed. That is, the stress is entirely in the plane of the film as the film is deflected. Third, it is assumed that there is no adhesive failure in the interface between film and substrate as the film is deflected. This implies that displacement at the edge of the suspended film is zero. Fourth, the residual stress of the film due to the manner of fabrication is a constant and is biaxially distributed in the plane of the film. Residual stress is also assumed to be uniform throughout the thickness of the film [60,61]. Fifth, the film is assumed in the linear elastic regime as it is deflected. The maximum deflection of films in this study is controlled in such a way that the maximum overall strain is less than 0.5%. Therefore, this assumption is quite reasonable.

The model for the deformed film is calculated using an energy minimization approach. Thus, the first step is to calculate the total strain energy of a deformed film. Let a circular membrane of radius a be clamped at the edge and be subjected to a uniform load of P (Fig. 3.1). Assume that the shape of the deflected surface can be represented as a hemispheric function:

$$w = \left(R^2 - r^2\right)^{1/2} - (R-d) \tag{3.9}$$

where w is the deflection in z-direction, R is the radius of curvature of the deflected membrane (Eq. 3.6), r is the radius position on the membrane, d is the deflection at the center of the membrane. Equation 3.9 may be approximated as

$$w = R\left(1 - \frac{r^2}{2R^2} - \frac{r^4}{8R^4} \cdots\right) - (R - d) \tag{3.10}$$

Substitution of the approximate form of Eq. 3.6 ($R \approx a^2/2d$) into Eq. 3.10 gives

$$w = d\left(1 - \frac{r^2}{a^2}\right) \tag{3.11}$$

Figure 3.2 shows that Eq. 3.11 is a good approximation for Eq. 3.9 when R is much larger than d. Since Eq. 3.11 is simpler than Eq. 3.9 in the mathematical calculation and the difference is trivial, Eq. 3.11 is then used exclusively in all following calculations.

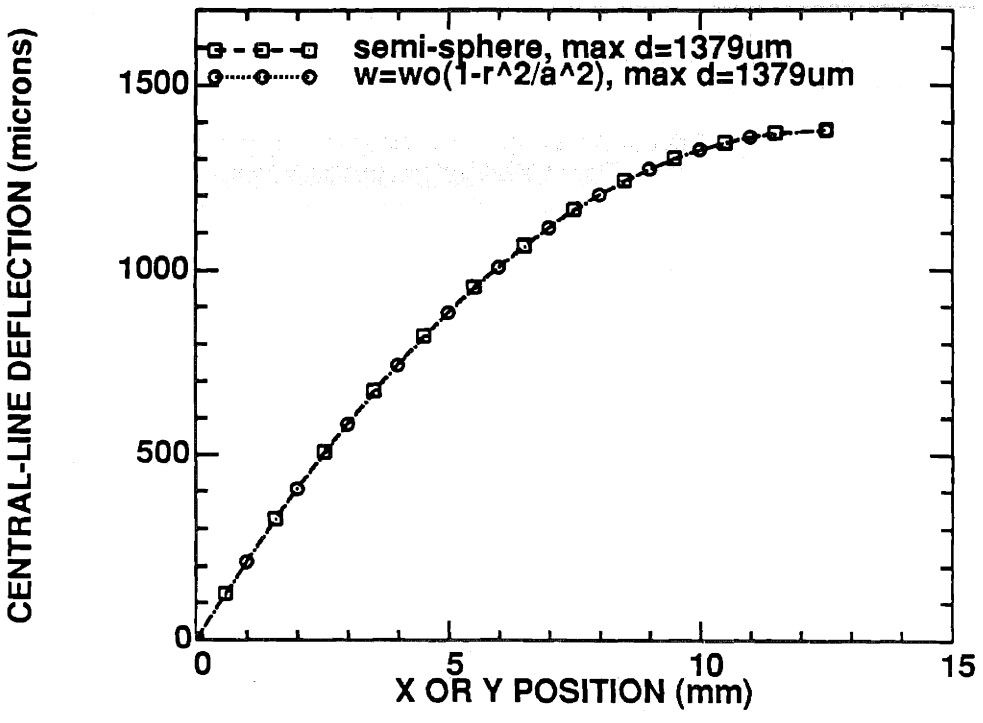

Figure 3.2 Modeled deflected shape along radius of a circular suspended film.

The displacement in r-direction u is assumed as [57]:

$$u = r\,(a-r)\,(k_1+k_2 r+k_3 r^2+\ldots) \tag{3.12}$$

which satisfies the boundary condition that u must be equal to zero both at the center and at the edge of the membranes. For Eq. 3.12, only two constants, k_1 and k_2, are used in this study. Thus, the strain in r-direction, ε_r, and the strain in the transverse direction, ε_t, are as follows (Fig. 3.3) [57]:

$$\varepsilon_r = \frac{du}{dr} + \frac{1}{2}\left(\frac{dw}{dr}\right)^2 = k_1 a + 2(k_2 a - k_1) r - 3k_2 r^2 + \frac{2d^2 r^2}{a^4} \tag{3.13}$$

$$\varepsilon_t = \frac{u}{r} = (a-r)(k_1 + k_2 r) \tag{3.14}$$

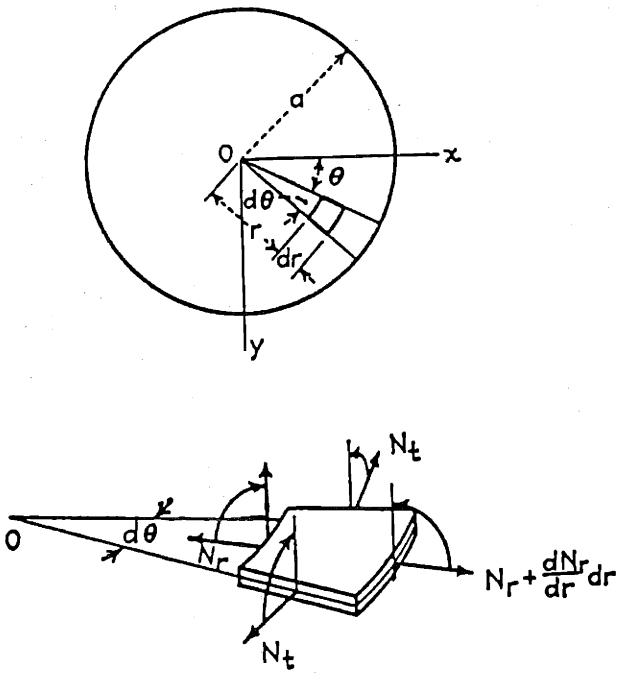

Figure 3.3 The definition of forces in a circular film [57].

By definition of the force balance (Fig. 3.3) and Hooke's law (linear elasticity), the following expressions are obtained

$$N_r = \frac{Et}{1-\nu^2}(\varepsilon_r + \nu\varepsilon_t) \tag{3.15}$$

$$N_t = \frac{Et}{1-\nu^2}(\varepsilon_t + \nu\varepsilon_r) \tag{3.16}$$

where N_r and N_t are the force per unit length in the radial and transverse direction, respectively, E is the Young's modulus, t is the thickness, and ν is the in-plane Poisson ratio. Therefore, the total forces along the plane of membrane become

$$N_r^{tot} = N_r + t\,\sigma_o \tag{3.17}$$

$$N_t^{tot} = N_t + t\,\sigma_o \tag{3.18}$$

where N_r^{tot} and N_t^{tot} are the total force per unit length in radial direction and transverse direction, respectively, and σ_o is the residual stress of the membrane. Using linear elasticity, the total strain energy V is given by

$$V = \frac{1}{2}\int_A (N_r^{tot}\varepsilon_r + N_t^{tot}\varepsilon_t)\, r\, dr\, d\theta \tag{3.19}$$

Substituting Eqs. 3.15-3.18 into Eq. 3.19, the total strain energy can be written as

$$V = \frac{\pi E t}{1-\nu^2}\int_0^a \left(\varepsilon_r^2 + \varepsilon_t^2 + 2\nu\varepsilon_r\varepsilon_t\right) r\, dr + \pi\sigma_o t\int_0^a (\varepsilon_r + \varepsilon_t) r\, dr \tag{3.20}$$

The first part of Eq. 3.20 is recognized as elastic strain energy V_{el} and the second part of it is the energy V_{res} due to the residual stress. Thus, the total strain energy can be expressed as

$$V = V_{el} + V_{res} \tag{3.21}$$

Therefore, by integrating Eq. 3.20, the elastic strain energy V_{el} due to the stretching can be obtained as

$$V_{el} = \frac{\pi E t}{1-\nu^2}\left(\frac{k_1^2 a^4}{4} + \frac{3k_1 k_2 a^5}{10} + \frac{7k_2^2 a^6}{60} + \frac{(\nu-3)k_1 a d^2}{5} + \frac{2(\nu-3)k_2 a^2 d^2}{15} + \frac{2d^4}{3a^2}\right) \tag{3.22}$$

and the strain energy due to residual stress , V_{res}, can be calculated as follows

$$V_{res} = \pi\sigma_o t d^2 \tag{3.23}$$

The constants, k_1 and k_2, are now determined using the assumption that the total strain energy of the membrane for the equilibrium position is a minimum energy. Hence, from the principle of the virtual displacement, it follows that

$$\frac{\partial V_{sys}}{\partial k_1} = \frac{\partial V_{sys}}{\partial k_2} = 0 \tag{3.24}$$

$$\frac{\partial V_{sys}}{\partial d} = 0 \tag{3.25}$$

where the system potential energy function V_{sys} is given by

$$V_{sys} = V - \int_A Pw\, r\, dr d\theta \tag{3.26}$$

The integration of Eq. 3.26 and Eq. 3.25 yields

$$\frac{\partial V}{\partial d} = \frac{\pi P a^2}{2} \tag{3.27}$$

From the two equations of Eq. 3.24, two linear equations for k_1 and k_2 are obtained.

$$k_1 = \frac{(3-\nu)d^2}{4a^3}, \qquad k_2 = \frac{(3-\nu)d^2}{4a^4} = \frac{k_1}{a} \ . \tag{3.28}$$

Substituting k_1 and k_2 into Eqs. 3.21-3.23, the total strain energy is given by

$$V = \frac{\pi E t d^4 (7-\nu)}{24a^2(1-\nu)} + \pi\sigma_o t d^2 \tag{3.29}$$

Substituting V into Eq. 3.27, the relationship between pressure and deflection becomes:

$$P = \frac{Et}{(1-\nu)}\left(\frac{7-\nu}{3a^4}\right)d^3 + \frac{4\sigma_o t}{a^2}d \tag{3.30}$$

There are two terms on the right-hand side of Eq. 3.30: biaxial modulus term (d^3 term) and residual stress term (d term). Equation 3.30 indicates that as the membrane is deflected, the biaxial modulus is associated with d^3 and the residual stress is related to d. For future convenience, Eq. 3.29 is re-written in the following manner:

$$\frac{Pa^2}{td} = C_2 f(\nu)\frac{E}{(1-\nu)}\left(\frac{1}{a^2}\right)d^2 + C_1\,\sigma_o \tag{3.31}$$

where the constants are expressed by:

$$f(\nu) = \frac{7-\nu}{8} \quad C_2 = \frac{8}{3} \quad , and \quad C_1 = 4 \tag{3.32}$$

In Eq. 3.32, the constant C_2 was chosen to be the same as the constant in Beams' equation (Eq. 3.8). Actually, the constants C_2 and $f(\nu)$ are not separable and C_2 can be any arbitrary number as long as the value of $C_2 f(\nu)$ is consistent. Equation 3.31 is the model for the single-layer circular membrane using the thin-film assumption. The convenience of the expression in Eq. 3.31 is the linear relationship between P/d and d^2. Hence, the biaxial modulus and the residual stress can be determined by the slope and intercept of a plot of P/d versus d^2, provided that all the constants are known. Equation 3.31 indicates that the coefficient of the modulus term $C_2 f(\nu)$ is a function of Poisson ratio while the coefficient of residual stress term C_1 is only a constant. The values of the constants obtained in this analysis will be compared to those from finite element method in next chapter.

3.2.3 Comparison of the Beams' Equation With Thin-film Model

In the small deflection regime (i.e. the magnitude of the deflection is smaller than the thickness), the residual stress term of Eq. 3.30 is then much bigger than the biaxial modulus term since size a is much larger than deflection d. Therefore, by neglecting the d^3 term, Eq. 3.30 can be expressed:

$$P = \frac{4\sigma_o t}{a^2} d \tag{3.33}$$

where the pressure is linearly proportional to the residual stress and to the deflection. Comparing Eq. 3.33 with Eq. 3.1, the forms of both equations are the same. This indicates these two equations are consistent in the case of small deflection.

Comparing Eq. 3.8 with Eq. 3.31, several similarities and differences are worth mentioning. First, both equations show that the general form for the relationship between pressure and deflection consists of two terms: biaxial modulus term and residual stress term. Second, the value of C_1 from both equations are exactly the same. It indicates that the residual stress evaluation is in good agreement in both calculations. Third, the function $f(\nu)$ is equal to unity in Beams' equation, while it is linearly Poisson ratio-dependent in Eq. 3.32. As mentioned above, the form of the Beams' equation is the same as the formula in the small deflection regime, which may cause certain errors. The difference may be also due to the different approach in calculating strain. The calculation of average strain in Eq. 3.32 is considered to be simplified; therefore, the Poisson ratio dependence of C_2 is eliminated. In order to narrow down error in the calculation of C_1, C_2, and $f(\nu)$, finite element method is used and shown in the next chapter.

3.2.4 Thick-Film Model

In this section, a thick-film model for circular membranes is generated. A typical cross-section of the thick deflected circular membrane is shown in Fig. 3.4. All assumptions for the deflected membranes in the previous section are still valid except the thin film assumption. For thick-film model, it is assumed that the strain functions for a thick deflected film are thickness dependent. That is, the strain on the top surface of membrane may not be the same as that on the bottom surface. This is the major difference between Fig. 3.4 and Fig. 3.1. The displacement in r-direction u is then assumed to be a function of z-axis. As Fig. 3.4 shows, if lines are drawn throughout the thickness of the membrane and perpendicularly to the surface, the lines would still be perpendicular to the surface even after deflection.

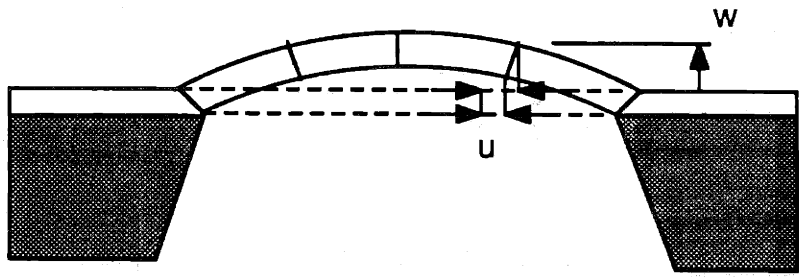

Figure 3.4 The film deflection under thick-film assumption.

To generate a z-dependent function for displacement functions, it is assumed that the difference of lateral displacement in z direction is a linear function of z and is proportional to the partial derivative of vertical displacement w. Therefore, the displacement functions w and u are expressed by

$$u = r\,(a\text{-}r)\,(k_1+k_2r) - z\frac{dw}{dr} = r\,(a\text{-}r)\,(k_1+k_2r) + \frac{2zdr}{a^2} \tag{3.34}$$

$$w = d\left(1 - \frac{r^2}{a^2}\right) \tag{3.35}$$

Notice that displacement function w is not changed from Eq. 3.11. There is one extra term in Eq. 3.34 (compared to Eq. 3.12) implying thickness effect on displacement. When z is equal to zero (i.e. a very thin film), then the extra term vanishes and Eq. 3.34 is the same as Eq. 3.12. That means for a very thin film, both models become the same. Thus, the strain in the r direction, ε_r, and the strain in the transverse direction, ε_t, are given by [57]:

$$\varepsilon_r = \frac{\partial u}{\partial r} + \frac{1}{2}\left(\frac{dw}{dr}\right)^2 = k_1a + 2(k_2a\text{-}k_1)r - 3k_2r^2 + \frac{2zd}{a^2} + \frac{2d^2r^2}{a^4} \tag{3.36}$$

$$\varepsilon_t = \frac{u}{r} = (a\text{-}r)\,(k_1+k_2r) + \frac{2zd}{a^2} \tag{3.37}$$

The strain energy due to the elastic stretching of the membrane becomes

$$V_{el} = \frac{\pi E}{1-\nu^2}\int_{-t/2}^{t/2}\int_0^a \left(\varepsilon_r^2 + \varepsilon_t^2 + 2\nu\varepsilon_r\varepsilon_t\right) r\,dr\,dz \tag{3.38}$$

Performing the integration:

$$V_{el} = \frac{\pi Et}{1-\nu^2}\left(\frac{k_1^2a^4}{4} + \frac{3k_1k_2a^5}{10} + \frac{7k_2^2a^6}{60} + \frac{(\nu\text{-}3)k_1ad^2}{5} + \frac{2(\nu\text{-}3)k_2a^2d^2}{15} + \frac{2d^4}{3a^2}\right)$$

$$+ \frac{\pi Et^2}{1-\nu}\left(\frac{d^3}{a^2} + \frac{4td^2}{3a^2}\right) \tag{3.39}$$

Strain energy due to residual stress , V_{res}, is

$$V_{res} = 2\pi\sigma_o \int_{-t/2}^{t/2}\int_0^a (\varepsilon_r+\varepsilon_t)r\, dr\, dz \tag{3.40}$$

Performing the integration,

$$V_{res} = \pi\sigma_o t d^2 \tag{3.41}$$

Comparing Eq. 3.41 to Eq. 3.23, it is found that the strain energy of residual stress is the same in both thin-film and thick-film models. This is in good agreement with the assumption of constant residual stress. Comparing Eq. 3.39 to Eq. 3.22, the extra terms in Eq. 3.39 are not a function of k_1 and k_2. Therefore, the values of k_1 and k_2 solved in Eq. 3.24 are not changed. Substituting the values of k_1 and k_2 from Eq. 3.28 into Eq. 3.39, the total strain energy V is then obtained by adding the strain energy of stretching and the strain energy due to the residual stress.

$$V = \frac{\pi E t d^4(7-\nu)}{24a^2(1-\nu)} + \frac{\pi E t^2}{1-\nu}\left(\frac{d^3}{a^2} + \frac{4td^2}{3a^2}\right) + \pi\sigma_o t d^2 \tag{3.42}$$

From the principle of virtual displacement, it follows that

$$\frac{\partial V}{\partial d} = \frac{\pi P a^2}{2} \tag{3.43}$$

Combining Eqs. 3.42 and 3.43,

$$P = \frac{Et}{(1-\nu)}\left(\frac{7-\nu}{3a^4}\right)d^3 + \frac{Et^2}{1-\nu}\left(\frac{6}{a^4}\right)d^2 + \left(\frac{16Et^3}{3a^4(1-\nu)} + \frac{4\sigma_o t}{a^2}\right)d \tag{3.44}$$

For the purpose of comparison, Eq. 3.44 is re-written as

$$\frac{Pa^2}{td} = C_2 f(\nu)\left(\frac{E}{a^2(1-\nu)}\right)d^2 + C_3\left(\frac{Et}{a^2(1-\nu)}\right)d + C_4\left(\frac{Et^2}{a^2(1-\nu)}\right) + C_1\sigma_o \qquad (3.45)$$

where the constants are

$$f(\nu) = \frac{7-\nu}{8}\ ,\quad C_2 = \frac{8}{3}\ ,\quad C_3 = 6\ ,\quad C_4 = \frac{16}{3}\ ,\ and\quad C_1 = 4 \qquad (3.46)$$

Equation 3.45 is the thick-film model for the single-layer circular membranes. Compared to Eq. 3.31, there are two extra terms on the right-hand side of Eq. 3.45: the term led by constant C_3 and the term led by constant C_4. These two extra terms are due to the bending effect of the thick films and are considered to be the thickness effect. These two terms have higher order in thickness dependence, compared to the other two original terms. Therefore, when films get thicker, the magnitude of the extra terms get bigger and are not negligible. When films are very thin, Eq. 3.45 degenerates to Eq. 3.31. Equation 3.46 also indicates that the coefficients in the extra terms, C_3 and C_4, are not a function of Poisson ratio. The values of these constants will be determined by finite element method in Section 4.3.

3.3 Square Films

3.3.1 Thin-Film Model

In square cases, the formulation is very similar to that of circular membranes. Only the geometry is different (Fig. 3.5). However, the formulation for the circular membranes is easier than that of the square membranes because of the radial symmetry of circular geometry. The assumption that used in Section 3.2.2 are used in this section as well. The functions of displacements of the deflected membrane are assumed as [58,59]:

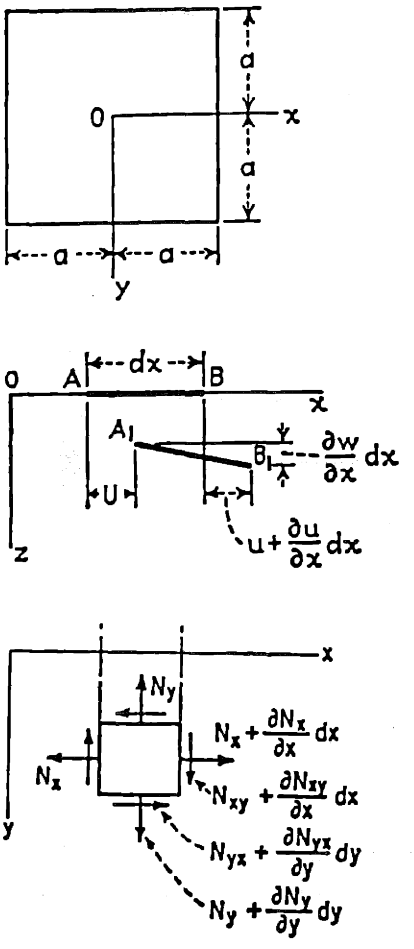

Figure 3.5 The displacements and forces in the deflection of a square film (a) the geometry of the film; (b) the displacements u and w; (c) the force balance in film deflection.

$$w = d\cos\left(\frac{\pi x}{2a}\right)\cos\left(\frac{\pi y}{2a}\right) \tag{3.45}$$

$$u = c\sin\left(\frac{\pi x}{a}\right)\cos\left(\frac{\pi y}{2a}\right) \tag{3.46}$$

$$v = c\sin\left(\frac{\pi y}{a}\right)\cos\left(\frac{\pi x}{2a}\right) \tag{3.47}$$

where the u, v, and w are the displacements along the x, y, and z axes respectively, d and c are two constants to be determined, and $2a$ is the size of diaphragm (Fig. 3.5). Notice that w fits the boundary conditions that zero at the edge and maximum at the center. Also, the displacement u and v fit the boundary conditions that zero at both the center and the edge of the membrane.

The energy minimization method based on Eqs. 3.45-3.47 is similar to the method in Section 3.2. The details of the calculation is shown in reference [58] and only the result is presented here. For a square membrane of side length $2a$, the load-deflection relation is:

$$\left(\frac{Pa^2}{td}\right) = C_2 f(\nu)\left(\frac{E}{1-\nu}\right)\left(\frac{1}{a^2}\right)d^2 + C_1\,\sigma_o \tag{3.48}$$

$$\text{where } C_2 f(\nu) = \frac{\pi^6}{32(1+\nu)}\left(\frac{5}{64} - \frac{(5-3\nu)^2}{[64(1+\nu)+9\pi^2(9-\nu)]}\right), \tag{3.49}$$

$$C_1 = \pi^4/32\ ,$$

P is the applied pressure, E is the Young's modulus, $E/(1-\nu)$ is the biaxial modulus, σ_o is the residual stress, ν is the Poisson ratio, t is the film thickness, and d is the deflection at the center of the membrane.

For the case of polyimide thin films, the Poisson ratio, ν, is assumed as 0.4. The value of $C_2 f(\nu)$ is, therefore, equal to 1.314 and Eq. 3.48 is reduced to the followings [58]:

$$\frac{Pa^2}{td} = 1.314\left(\frac{E}{1-\nu}\right)\left(\frac{1}{a^2}\right)d^2 + 3.044\,\sigma_o \tag{3.50}$$

The value of $C_2 f(\nu)$ (Eq. 3.49) is not very sensitive to the value of Poisson ratio. That is, the value of $C_2 f(\nu)$ is only changed by 3.4% when Poisson ratio is changed by 10% ($\pm$0.05) [47].

3.3.2 Thick-Film Model

In this section the thickness effect of the square membranes is discussed. The condition is similar to the circular case. The strain of the membrane is now assumed as a function of z. That is, the strain at the top surface is not the same as that at the bottom surface (Fig. 3.4). Thus, the lateral displacements, u and v, are not constant along the z-axis. As discussed in Section 3.2.4, it is also assumed that the difference of lateral displacements in z direction is a linear function of z and is proportional to the partial derivative of the vertical displacement w:

$$w = d\cos\left(\frac{\pi x}{2a}\right)\cos\left(\frac{\pi y}{2a}\right) \tag{3.51}$$

$$u = c\sin\left(\frac{\pi x}{a}\right)\cos\left(\frac{\pi y}{2a}\right) - z\frac{\partial w}{\partial x} \tag{3.52}$$

$$v = c\sin\left(\frac{\pi y}{a}\right)\cos\left(\frac{\pi x}{2a}\right) - z\frac{\partial w}{\partial y} \tag{3.53}$$

where z is the vertical position on z-axis (Fig. 3.4). In this study, the origin of z axis is at the center of the film. It is important to know that the lateral displacements, u and v, are no longer zero at the edge of the diaphragm. The elastic strain in x-direction and y-direction are given as [59]:

$$\varepsilon_x = \frac{\partial u}{\partial x} + \frac{1}{2}\left(\frac{\partial w}{\partial x}\right)^2 \tag{3.54}$$

$$\varepsilon_y = \frac{\partial v}{\partial y} + \frac{1}{2}\left(\frac{\partial w}{\partial y}\right)^2 \tag{3.55}$$

$$\gamma_{xy} = \frac{\partial u}{\partial y} + \frac{\partial v}{\partial x} + \frac{\partial w}{\partial x}\frac{\partial w}{\partial y} \tag{3.56}$$

The force per unit length in the membrane are given as:

$$N_x = \frac{Et}{1-\nu^2}(\varepsilon_x + \nu\varepsilon_y) \tag{3.57}$$

$$N_y = \frac{Et}{1-\nu^2}(\varepsilon_y + \nu\varepsilon_x) \tag{3.58}$$

$$N_{xy} = 2tE(1+\nu)\,\varepsilon_{xy} \tag{3.59}$$

For the linear elastic case, the total strain energy V can be expressed by

$$V = \frac{1}{2}\int_V (N_x\varepsilon_x + N_y\varepsilon_y + N_{xy}\gamma_{xy})\,dx\,dy\,dz + \int_V \sigma_o(\varepsilon_x + \varepsilon_y)\,dx\,dy\,dz \tag{3.60}$$

The first part of the right-hand side of Eq. 3.60 is the strain energy of elastic force and the second part of the right-hand side is the energy due to the residual stress. Substitute Eqs. 3.54-3.59 into Eq. 3.60, the elastic strain energy and residual stress strain energy become

$$V_{el} = \frac{E}{2(1-\nu^2)}\int_{-t/2}^{t/2}\int_{-a}^{a}\int_{-a}^{a}\left(\varepsilon_x^2 + \varepsilon_y^2 + 2\nu\varepsilon_x\varepsilon_y + \frac{1}{2}(1-\nu)\gamma_{xy}^2\right)dx\,dy\,dz \tag{3.61}$$

$$V_{res} = \sigma_o\int_{-t/2}^{t/2}\int_{-a}^{a}\int_{-a}^{a}(\varepsilon_x + \varepsilon_y)\,dx\,dy\,dz \tag{3.62}$$

Therefore, the elastic strain energy due to the stretching can be obtained by performing the integration:

$$V_{el} = \frac{Et}{2(1-\nu^2)}\left(\frac{16(1+\nu)c^2}{9} + \frac{\pi^2(9-\nu)c^2}{4} + \frac{5\pi^4d^4}{256a^2} + \frac{(3\nu-5)\pi^2d^2c}{6a}\right) +$$

$$\frac{Et^2}{2(1-\nu^2)}\left(\frac{\pi^4(2-\nu)d^2t}{24a^2} + \frac{4\pi^2dc}{3a} + \frac{\pi^2(1+3\nu)d^3}{9a^2}\right) \tag{3.63}$$

The strain energy due to the residual stress , V_{res}, can be calculated as the following:

$$V_{res} = \frac{\pi^2 \sigma_o t d^2}{4} \tag{3.64}$$

The constant c is determined from the condition that the total strain energy of the membrane for a equilibrium position is in a minimum energy. Hence from the principle of the virtual displacement, it follows that

$$\frac{\partial V_{sys}}{\partial c} = \frac{\partial V_{sys}}{\partial d} = 0 \tag{3.65}$$

where the system potential energy function given by

$$V_{sys} = V - \int_A Pw \; dx \; dy \tag{3.66}$$

Performing the integration, Eq. 3.66 becomes

$$\frac{\partial V_{sys}}{\partial d} = \frac{16Pa^2}{d} \tag{3.67}$$

From the first part of Eq. 3.65, c can be solved.

$$c = \frac{(5-3\nu)d^2}{12a\left(\frac{16(1+\nu)}{9\pi^2} + \frac{(9-\nu)}{4}\right)} \tag{3.68}$$

Substituting V and c into Eq. 3.67, it becomes:

$$\frac{Pa^2}{td} = C_2 f(\nu)\left(\frac{E}{1-\nu}\right)\left(\frac{1}{a^2}\right)d^2 + C_3(\nu)\left(\frac{E}{1-\nu}\right)\left(\frac{t}{a^2}\right)d + C_4(\nu)\left(\frac{E}{1-\nu}\right)\left(\frac{t^2}{a^2}\right) + C_1 \sigma_o \tag{3.69}$$

where $C_3(\nu) = \frac{\pi^4}{16(1+\nu)}\left(\frac{12(5-3\nu)\pi^2}{[64(1+\nu)+9\pi^2(9-\nu)]} + \frac{1+3\nu}{3}\right)$, (3.70)

$$C_4(\nu) = \frac{\pi^6}{32(1+\nu)}\left(\frac{2-\nu}{4} - \frac{128}{[64(1+\nu)+9\pi^2(9-\nu)]}\right), \tag{3.71}$$

and C_1 and $C_2 f(\nu)$ are the same as Eq. 3.49.

For the case of $\nu = 0.4$, the values of C_3 and C_4 are 5.48 and 5.366, respectively. Recall that the values of $C_2 f(\nu)$ and C_1 are 1.314 and 0.308, respectively. Therefore, Eq. 3.69 can be reduced as:

$$\frac{Pa^2}{td} = 1.314\left(\frac{E}{1-\nu}\right)\left(\frac{1}{a^2}\right)d^2 + 5.48\left(\frac{E}{1-\nu}\right)\left(\frac{t}{a^2}\right)d + 5.365\left(\frac{E}{1-\nu}\right)\left(\frac{t^2}{a^2}\right) + 3.044\,\sigma_o \quad (3.72)$$

The Eq. 3.72 is very similar to the Eq. 3.49 except two extra terms. These two terms are negligible when the thickness t is much smaller than the deflection d. It means Eq. 3.49 is still a good approach when the thickness is very small. The values of constants will be re-calculated using FEM and the discussion of the relative magnitude of these constants will also be given in next chapter.

3.4 Multi-layer Models

From above calculation, it is found that the mathematical formula for the load-deflection of circular and square membranes are the same except the coefficients in the formula. Therefore, in this section only the multi-layer models for square membranes are derived. The multi-layer model for circular membranes is assumed to be the same formula as those for square membranes except the coefficients. Two different methods to calculate the strain energy of multi-layer membranes are introduced here. The first model is under the assumption of thin film. That is, each layer behaves like a thin film in Section 3.3.1. The second model considers that each layer behaves like a thick film in Section 3.3.2.

3.4.1 Thin Film Assumption in Multi-layer Model

In the case of multi-layer thin films, each layer has its own material parameters. The subscript i is used in the following to indicate the parameters of *i-th* layer and there are totally n different layers in each sample. It is assumed that no adhesive failure occurs in the interface of layers. The deflection behavior is shown in Fig. 3.6.

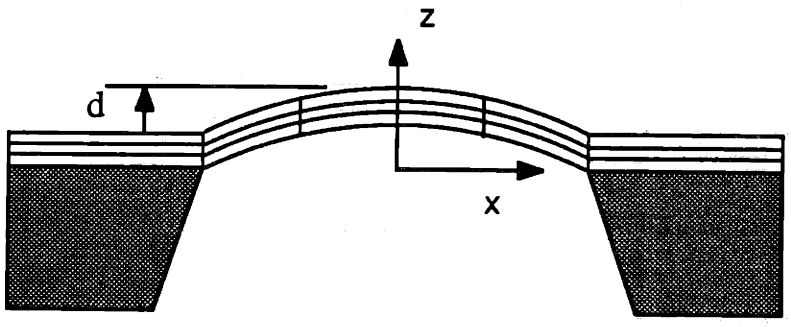

Figure 3.6 The deflection of a multi-layer suspended film under the thin-film assumption.

For a thin-film multi-layer model, it is assumed that there is no differences in lateral displacements through the thickness. That is, the lines which are perpendicular to x-y plane before deflection would still be perpendicular to x-y plane after deflection (Fig. 3.6). The displacements along x and y axes (u and v) for different layers are all the same:

$$w_i = d\cos\left(\frac{\pi x}{2a}\right)\cos\left(\frac{\pi y}{2a}\right) + \sum_{k=1}^{i-1} t_k \tag{3.73}$$

$$u_i = c\sin\left(\frac{\pi x}{a}\right)\cos\left(\frac{\pi y}{2a}\right) \tag{3.74}$$

$$v_i = c\ sin\left(\frac{\pi y}{a}\right) cos\left(\frac{\pi x}{2a}\right) \tag{3.75}$$

As shown in Eq. 3.73, the extra term of w_i is not a function of x and y. Therefore, $\partial w_i/\partial x$ and $\partial w_i/\partial y$ are the same as those in the Eq 3.51. The strain energy of each layer in a multi-layer membrane is computed from the single-layer model. The total strain energy of multi-layer membranes can be calculated by summation of the strain energy of each layer. Using the same energy minimization approach, the mathematic analysis of n-layer thin films showed the following relations:

$$\frac{Pa^2}{d} = C_2(\nu_i, E_i, t_i)\left(\frac{1}{a^2}\right)d^2 + C_1 \sum_{i=1}^{n} \sigma_i t_i \tag{3.76}$$

$$\text{where } C_2(\nu_i, E_i, t_i) = \left(\frac{5\pi^6}{2048}\right)\sum_{i=1}^{n} E_i t_i/(1-\nu_i^2) - \frac{\frac{\pi^6}{32}\left(\sum_{i=1}^{n} E_i t_i(5-3\nu_i)/(1-\nu_i^2)\right)^2}{64\sum_{i=1}^{n} E_i t_i/(1-\nu_i) + \sum_{i=1}^{n} E_i t_i 9\pi^2(9-\nu_i)/(1-\nu_i^2)}$$

$$C_1 = \frac{\pi^4}{32}$$

Notice that the residual term is still a simple summation of the residual stress of each layer while the biaxial modulus term turns into a very complicate result due to the difference of Poisson ratio and thickness in each layer. It is also found that the value of C_1 in the multi-layer model is the same as the value in the single-layer model. This is a big benefit for calculating the residual stress of multi-layer membranes from experimental data since the coefficient is only a constant (see also chapter 5). When the number of layers n is equal to 1, Eq. 3.76 reduces to the single-layer thin-film model (Eq. 3.48).

Assume the Poisson ratio of each layer is the same: $\nu_i = \nu$. Therefore, Eq. 3.76 can be reduced as

$$\frac{Pa^2}{d} = C_2(E_i,t_i)\left(\frac{1}{a^2}\right)d^2 + C_1\sum_{i=1}^{n}\sigma_i t_i \tag{3.77}$$

$$\text{where } C_2(E_i,t_i) = \frac{\pi^6}{32(1+\nu)}\left(\frac{5}{64} - \frac{(5-3\nu)^2}{[64(1+\nu)+9\pi^2(9-\nu)]}\right)\sum_{i=1}^{n}E_i t_i \quad , \tag{3.78}$$

$$C_1 = \frac{\pi^4}{32}$$

Equation 3.77 has a very similar form to Eq. 3.48 and the constants are also exactly the same as Eq. 3.48. This indicates that the multi-layer thin-film model is a summation form of the single-layer thin-film model. The constants in multi-layer model are the same as those in single-layer model provided that the Poisson ratios of each layer are all the same. Otherwise , the constants ends up in a very complicated form (Eq. 3.76).

3.4.2 Thick Film Assumption in Multi-layer Models

The schematic deflection for thick-film multi-layer is shown in Fig. 3.7. The assumptions used in the previous section are also used here except the thin film assumption. That is, in this section, each layer in the multi-layer structure behaves as the thick film in Section 3.3.2. Therefore, the strain of each layer may not be the same and is a function of the z-axis position. The functional forms of displacements are very similar as Eqs. 3.73-3.75 and are expressed by

$$w_i = d\cos\left(\frac{\pi x}{2a}\right)\cos\left(\frac{\pi y}{2a}\right) + \sum_{k=1}^{i-1}t_k \tag{3.79}$$

$$u_i = c\sin\left(\frac{\pi x}{a}\right)\cos\left(\frac{\pi y}{2a}\right) - z_i\left(\frac{\partial w_i}{\partial x}\right) \tag{3.80}$$

$$v_i = c\sin\left(\frac{\pi y}{a}\right)\cos\left(\frac{\pi x}{2a}\right) - z_i\left(\frac{\partial w_i}{\partial y}\right) \tag{3.81}$$

where z_i is the position in z-direction for the i-th layer, and $\sum_{k=1}^{i-1} t_k < z_i < \sum_{k=1}^{i} t_k$.

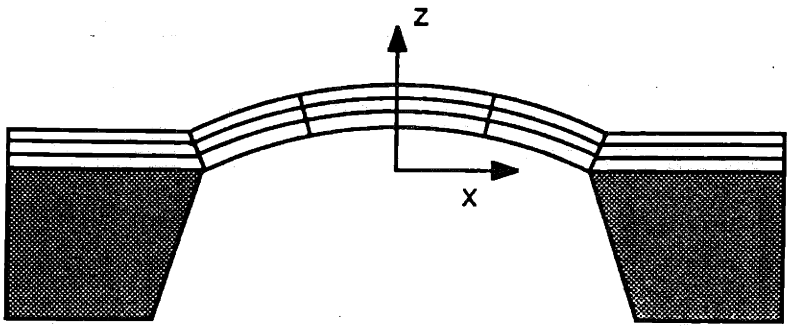

Figure 3.7 The deflection of a multi-layer suspended film under the thick-film assumption.

Follow the method shown in the previous section, the relationship between deflection d and pressure P is shown as follows :

$$\frac{Pa^2}{d} = \left(\frac{\pi^2}{16a^2}\right)\left(B_1 d^2 + B_2 d\right) + \left(\frac{\pi^2}{16a^2} B_3 + \frac{\pi^4}{32} \sum_{i=1}^{n} \sigma_i t_i\right) \tag{3.82}$$

where $B_1 = 4\sum_{i=1}^{n} E_i t_i p_i - (\sum_{i=1}^{n} E_i t_i q_i)^2 / \sum_{i=1}^{n} E_i t_i r_i$, (3.83)

$$B_2 = 3\sum_{i=1}^{n} E_i t_i \gamma_i g_i - \frac{3}{2}(\sum_{i=1}^{n} E_i t_i \beta_i g_i)(\sum_{i=1}^{n} E_i t_i q_i) / \sum_{i=1}^{n} E_i t_i r_i , \tag{3.84}$$

$$B_3 = 2\sum_{i=1}^{n} E_i t_i \alpha_i h_i - (\sum_{i=1}^{n} E_i t_i \beta_i g_i)^2 / (2\sum_{i=1}^{n} E_i t_i r_i) , \tag{3.85}$$

$$f_i = \sum_{k=1}^{i-1} t_k , \quad g_i = \frac{t_i}{2} + f_i , \quad h_i = (f_{i+1}^2 + f_{i+1} f_i + f_i^2)/3 , \tag{3.86}$$

$$p_i = \frac{5\pi^4}{512(1-\nu_i^2)}, \quad q_i = \frac{(3\nu_i-5)\pi^2}{12(1-\nu_i^2)}, \quad r_i = \frac{64(1+\nu_i) + 9\pi^2(9-\nu_i)}{72(1-\nu_i^2)}, \tag{3.87}$$

$$\alpha_i = \frac{(2-\nu_i)\pi^4}{16(1-\nu_i^2)}, \quad \beta_i = \frac{4\pi^2}{3(1-\nu_i^2)}, \quad \gamma_i = \frac{(1+3\nu_i)\pi^2}{9(1-\nu_i^2)}. \tag{3.88}$$

Although Eq. 3.82 is extremely complicated, it is noted that the similarity of the formula between the single-layer thick-film model (Eq. 3.69) and the multi-layer thick-layer model (Eq. 3.82). As mentioned in the above section, the complexity of this equation is party due to the difference in the Poisson ratio of each layer. As also seen in Section 3.3.2, two extra terms are shown in Eq. 3.82. These two terms are due to the bending effect in the thick-film assumption. It is also noted that the coefficient of the residual term is still the same as that in Eq. 3.69.

CHAPTER 4

Finite Element Method for Film Deflection

4.1 Introduction

In this chapter. the finite element method (FEM) is introduced for the simulation of load-deflection behavior of suspended films. This simulated load-deflection relationship was used for calculating the geometry and Poisson ratio-dependent constants in the mathematical models derived in the previous chapter. It is believed that the constants calculated using FEM are more accurate than using analytic solutions due to more accurate deflected shapes predicted by FEM simulations.

The first half of this chapter discusses the fundamentals and the verification of FEM used for calculating film deflection. The basic concepts of FEM are briefly described in Section 4.2. The use of FEM is verified in Section 4.3 which describes the details such as types of the elements, the number of elements, and the comparison of the film deflections from experiments, FEM, and analytic solutions.

The second half of this chapter describes FEM for calculating the constants in the mathematical models derived in Chapter 3. These models include both thin-film and thick-film models for circular (Section 4.4) and square samples (Section 4.5). The difference between thin-film and thick-film models is called the thickness effect and is also discussed in Sections 4.4.and 4.5. The constants of multi-layer models are determined in Section 4.6.

The work of comparing deflected shapes (in Section 4.3.4) was carried out in collaboration with Jeffrey Y. Pan and Fariborz Maseeh. This work has been reported by Pan et al. in the 1990 IEEE Solid State Sensor and Actuator Workshop at Hilton Head Island, South Carolina [62].

4.2 Basic Concepts of Finite Element Method

The finite element method (FEM) is generally applicable for numerical solutions [63-66]. Problems of continuum mechanics, electric fields, heat transfer, and fluid flow have been solved using FEM [67,68]. In this study, FEM is used solely for mechanical analysis of film deflection. The FEM used in this study is the commercially available ADINA program (ADINA Engineering Inc., Watertown, Massachusetts).

The basic concepts of FEM are summarized and only the most general situation is described here. To solve a general problem of solid mechanics using FEM, several steps are followed: (1) discretize the body of solid, (2) select an interpolation model for elements, (3) calculate the element stiffness matrices and the overall equilibrium equations, (4) solve the nodal displacements, and (5) calculate stresses and strains.

In the first step, the actual body of solid (the film) is represented as a group of subdivisions called finite elements. These elements are considered to be interconnected at specified joints called nodes or nodal points. The nodes are usually distributed on element boundaries and/or inside elements. The nodes on the boundaries are shared with adjacent elements. The choice of type, number, size, and arrangement of the elements depends on the characteristics of the problem.

Next, it is assumed that the variation of the field variable (e.g. displacement, stress, etc.) inside a finite element can be approximated by a simple polynomial function (called

interpolation model). For example, if displacement is assumed, the model is called the assumed displacement model. In the third step, using the assumed displacement model and equilibrium equations, the element stiffness matrices and load vectors of an element are derived . Then, these individual element stiffness matrices and load vectors are assembled to form the overall equilibrium equations for the entire body.

Fourth, the overall equilibrium equations for the whole body are then incorporated into boundary conditions. At this point, a set of simultaneous equations (in a matrix form) are generated. By solving these equations, the nodal values of the field variable (e.g., displacement) can be obtained. Finally, once the displacement field is known, other field variables (such as stress, strain, etc.) throughout the whole group of elements can then be calculated.

The ADINA program was run on a SUN-4 workstation. The discretization of the elements, the material properties and the boundary conditions are needed as input for each run. The films were modeled as linear elastic materials with uniform biaxial residual stress. The residual stress of films was generated as thermal stress by a temperature difference between the film and the reference temperature. The film deflection was treated as a nonlinear large-deflection small-strain problem, and therefore, the pressure loads were increased incrementally to allow the geometrical convergence [69.70].

4.3 Finite Element Analysis on Film Deflection

In this section, the FEM simulations for film deflection are presented. The purposes are two-fold: (1) to find the correct element types for FEM analysis; (2) to verify that FEM is more accurate than analytic solutions.

4.3.1 Types of Elements

In this study, deflection of thin films by lateral pressure was simulated by FEM. Several types of elements were used to solve this problem. The types of elements and the number of nodes selected for this work are shown in Table 4.1. Different elements were used to check the consistency between elements. The geometries, shapes, and boundary conditions of elements are described in this section.

Film Shape	Element Type	Nodes per Element	Number of Elements	Number of Nodes	Ratioed Elements	Triangle Elements
Circular	2D solid	8	250	1005	yes	no
	2D solid	9	250	1255	no	no
	Shell	4	1200	1261	no	no
	Shell	4	1024	1057	no	yes
	Shell	16	105	1000	yes	no
	Shell	16	64	569	yes	yes
Square	Shell	4	576	625	no	no
	Shell	4	576	625	yes	no
	Shell	16	64	625	yes	no
	3D solid	20	256	1955	yes	no

Table 4.1 The types of elements used in FEM for film deflection.

Four different types of elements were chosen for square films: shell 4-node elements with two geometries, shell 16-node elements, and 3D-solid 20-node elements. For circular films, more choices were available. Six types of elements were used (Table 4.1): shell 4-node elements with two geometries, shell 16-node elements also with two geometries, as well as 2D-solid 8-node and 9-node elements (with axial symmetry).

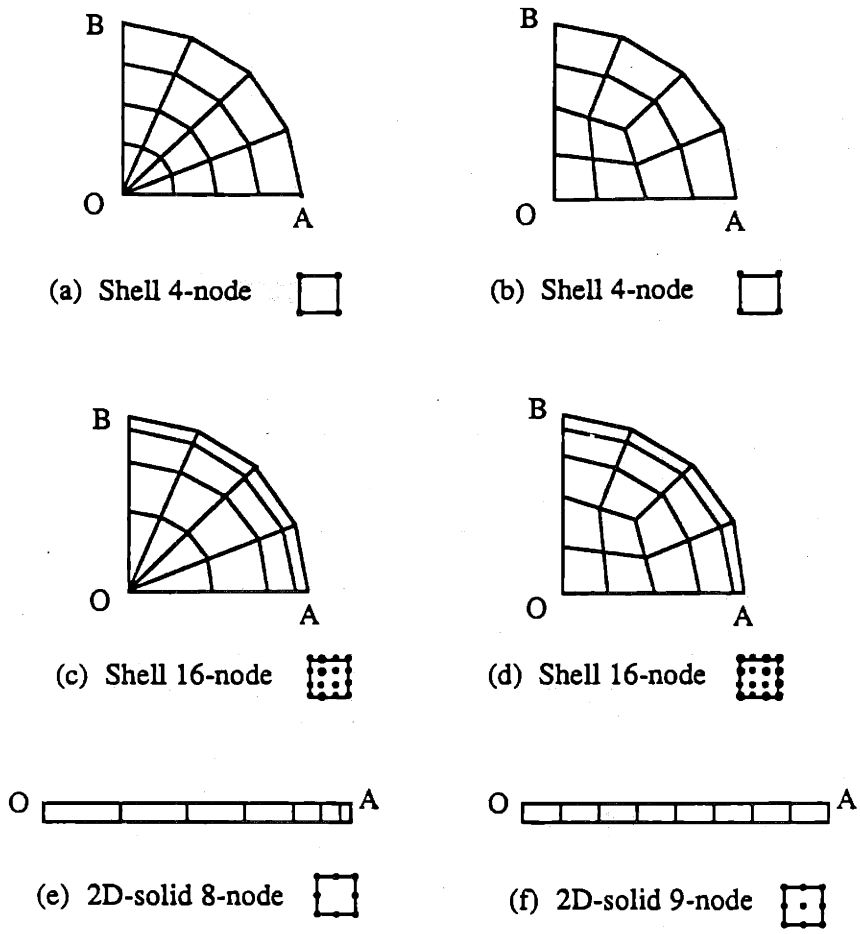

Figure 4.1 The geometries of elements for circular films. (a) shell 4-node with triangle elements; (b) shell 4-node without triangle elements; (c) shell 16-node with triangle and ratioed elements; (d) shell 16-node with ratioed elements; (e) 2D-solid 8-node ratioed elements; (f) 2D-solid 9-node regular elements. The point O is the center of the film and arc AB is the edge of the film.

Figures 4.1 and 4.2 show the schematic geometry of circular and square elements, respectively. For each type of shell element in circular films, there were two different types of mesh: one with triangle elements and the other without. The mesh with triangle elements was straightforward, while the mesh without triangle elements was made from three quadrilateral subgroups (Fig. 4.1). Ratioed elements were selected for several different

elements (Figs. 4.1 and 4.2). The use of ratioed elements makes the size of the elements along the film edges smaller than the element size at the center of film. It was found that these small size elements were essential for shell 16-node and 3D-solid 20-node elements to reduce edge displacement error which led to an offset in the center deflection. For 2D-solid and shell 4-node elements, the difference in deflection results between regular and ratioed elements was very small (~0.15%). Examples and more discussion about ratioed elements are given in Section 4.3.2.

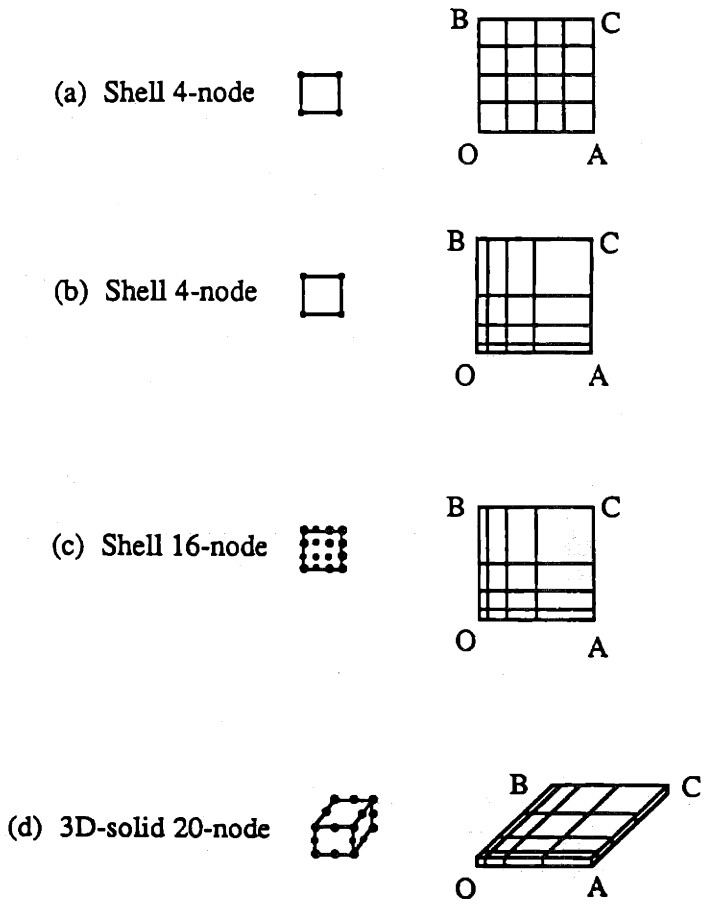

Figure 4.2 The geometries of elements for square films. (a) shell 4-node regular elements; (b) shell 4-node ratioed elements; (c) shell 16-node ratioed elements; (d) 3D-solid 20-node elements. The point O is the corner of the film and the point C is the center of the film.

3D-solid elements are usually used for a bulky, 3-dimensional body of matter. In order to use them for solving the problem of thin film (a sort of 2-dimensional geometry), a fine mesh approach is necessary. That is why the number of nodes for 3D-solid elements was the highest in Table 4.1, and its computing time was also the most among those elements.

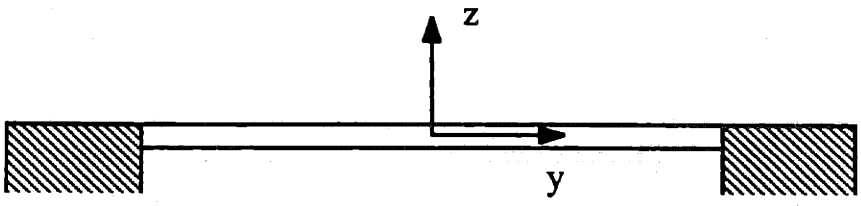

(a) Boundary conditions in z-direction

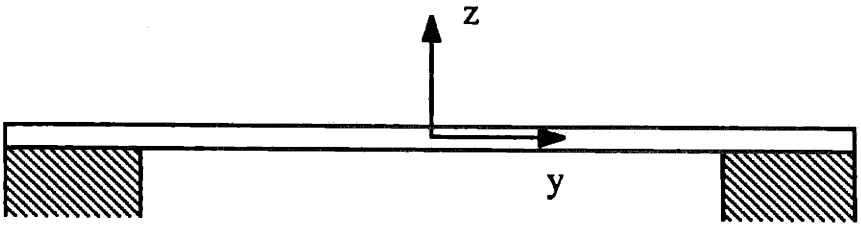

(b) Boundary conditions in y-direction

Figure 4.3 The boundary conditions for 2D-solid elements. (a) boundary conditions in z-direction; (b) boundary conditions in y-direction.

The edges of suspended films were considered to be clamped edges and the boundary conditions were fixed at film edges for zero degree of freedom. That is, all the six degrees of freedom (x-, y-, z-axis translations and rotations) were fixed along the

edges. However, the mesh of 2D-solid elements (with axial symmetry) in circular films were the cross-section of the film, which was different from other elements. Hence, there were two choices of boundary conditions for 2D-solid elements (Fig. 4.3): the boundary conditions were fixed along z-axis (the same as other elements) or along y-axis. In the actual fabricated samples, the suspended films were adhered onto substrates or rings, and the y-direction boundary conditions were closer to the real situation in film deflection. Nevertheless, this kind of boundary conditions (in y-direction) is applicable only for 2D-solid elements in circular films. The boundary conditions along z-axis had to be used for all other types of elements. The comparison between these two different boundary conditions are shown in Fig. 4.4. The difference in film deflection was found to be insignificant.

4.3.2 Convergence of the Film Deflection

In this section, the FEM simulated film deflections using different elements are discussed. First, the center deflection as a function of the number of elements is described. The purpose of these FEM simulations is to find out the numbers of elements that are necessary for different elements in order to have convergence in FEM analysis. Second, the results of FEM deflected shapes using different elements are compared.

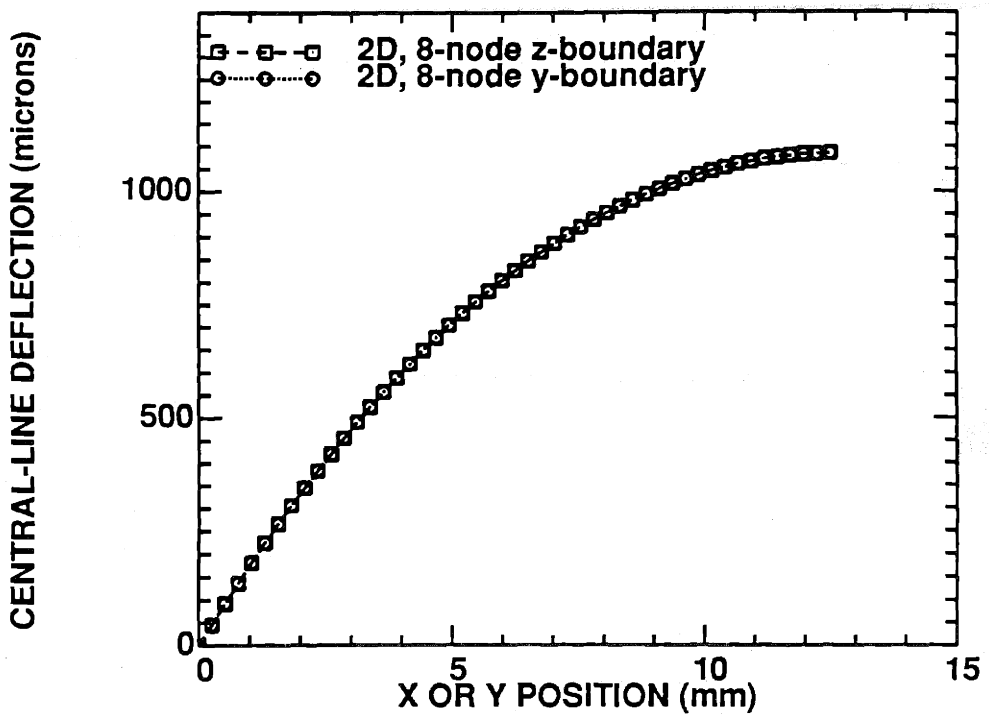

Figure 4.4 The deflection shapes for 2D-solid 8-node elements with boundary conditions in y- and z-direction.

Figure 4.5 shows the convergence of the center deflection in square films, simulated by FEM. These simulations were done by assuming the film properties and geometries as: a=4mm, E=2910MPa, ν=0.25, σ_o=28.7MPa, and t=8.5μm. Four different types of elements were used: three ratioed elements (shell 4-node, shell 16-node, and 3D 20-node) and one regular element (shell 4-node). Figure 4.5 shows that the difference between the results of these element types is less than 0.3% in a very fine mesh. Two things are worth mentioning here. First, for shell 4-node elements, the difference between ratioed and regular is indistinguishable (about 0.15%). Second, the 3D-solid element has higher number of nodes (20 nodes) per element, and therefore, it needs a large number of

nodes to converge. It is concluded that the FEM analysis converges to the same deflection regardless of the element type when the mesh is fine enough.

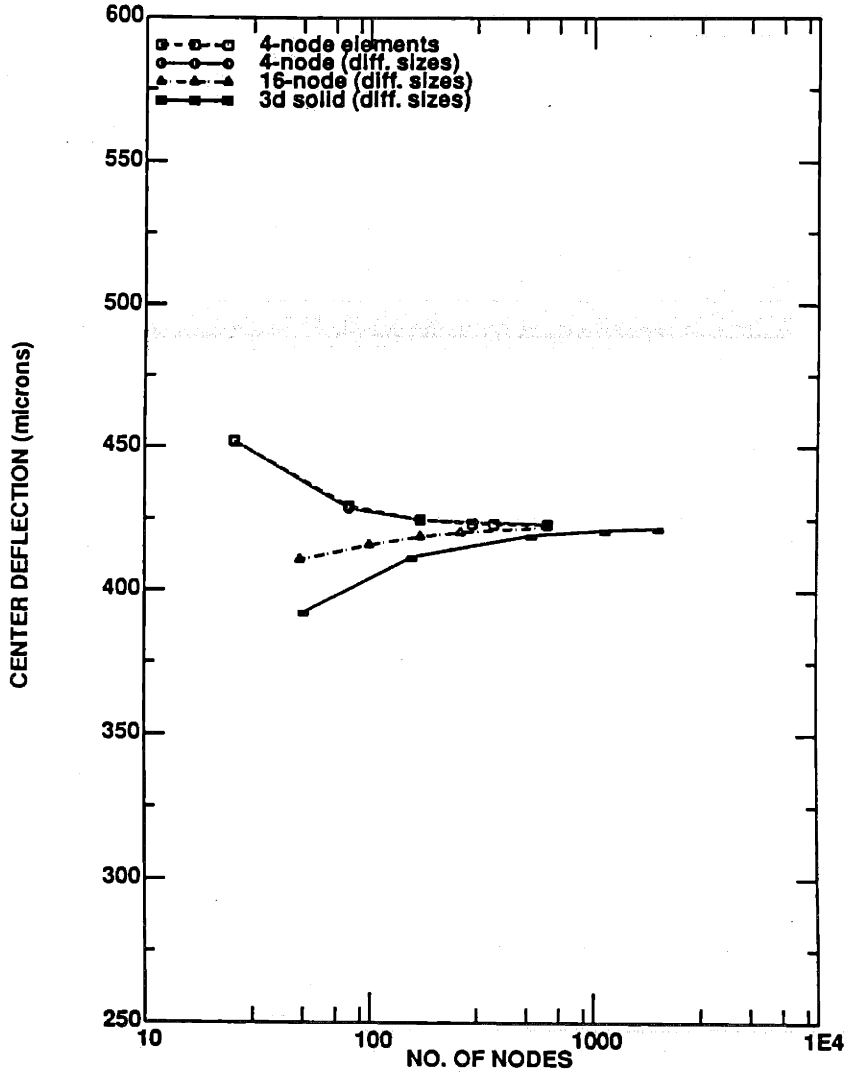

Figure 4.5 The center deflection versus number of nodes for square films with four different elements: shell 4-node (with two geometries) elements, shell 16-node elements, and 3D-solid 20-node elements.

Another way of investigating the convergence of different elements is to look at the simulated deflected shapes using different elements. The FEM simulation of the deflected shapes of square film is shown in Fig. 4.6a. These simulations were also carried out by assuming: a=4mm, E=2910MPa, ν=0.25, σ_o=28.7MPa, and t=8.5μm. Three different types of elements were used. The numbers of elements for each type of element are shown in Table 4.1. The difference in the center deflection between these types of elements was indistinguishable (less than 0.3%). As mentioned above, for the types of shell 16-node element and 3D-solid 20-node element, the element sizes along the edges had to be small enough, otherwise the displacement error at the edge would lead to an offset in the center deflection. In this study, the smallest size for shell 16-node element was 0.047mm, or 1.2%, and for 3D solid element was about 0.058mm, or 1.6% (the entire size of the film was 4mm).

The results of the circular film were similar to square films and are shown in Fig. 4.6b. Again the difference in the center deflection among these different types of elements was also less than 0.3%. This indicates that our FEM analysis was quite consistent among these element types. Again, the ratioed elements were found necessary for two shell 16-node elements, which is the same case as in the square films. Since the differences among these types of elements were extremely small, the following FEM analyses were performed using shell 4-node regular elements for square films and 2D-solid ratioed 8-node elements (with y-axis boundary conditions) for circular films in order to save computing time.

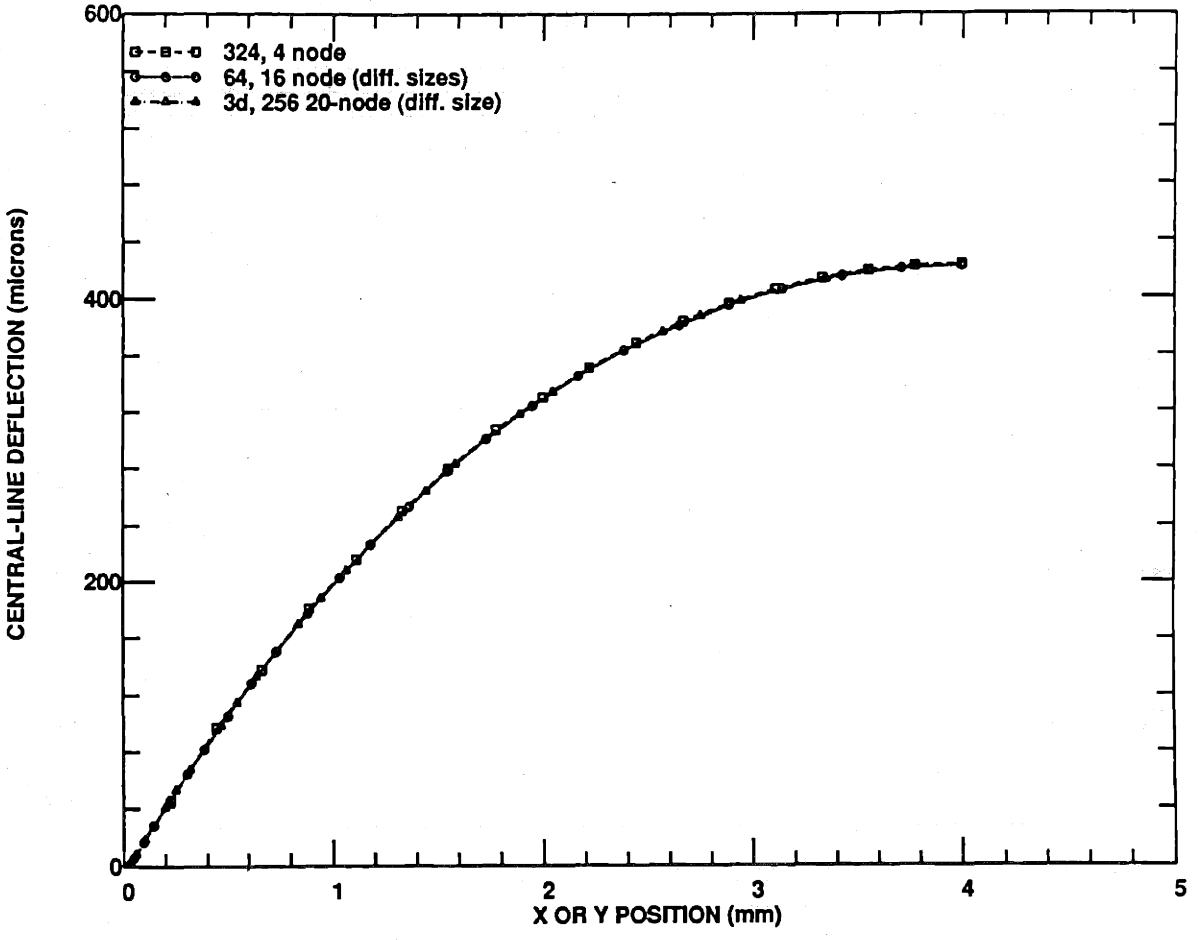

Figure 4.6a The deflection shapes for square films with three different elements: shell 4-node , shell 16-node , and 3D-solid 20-node elements.

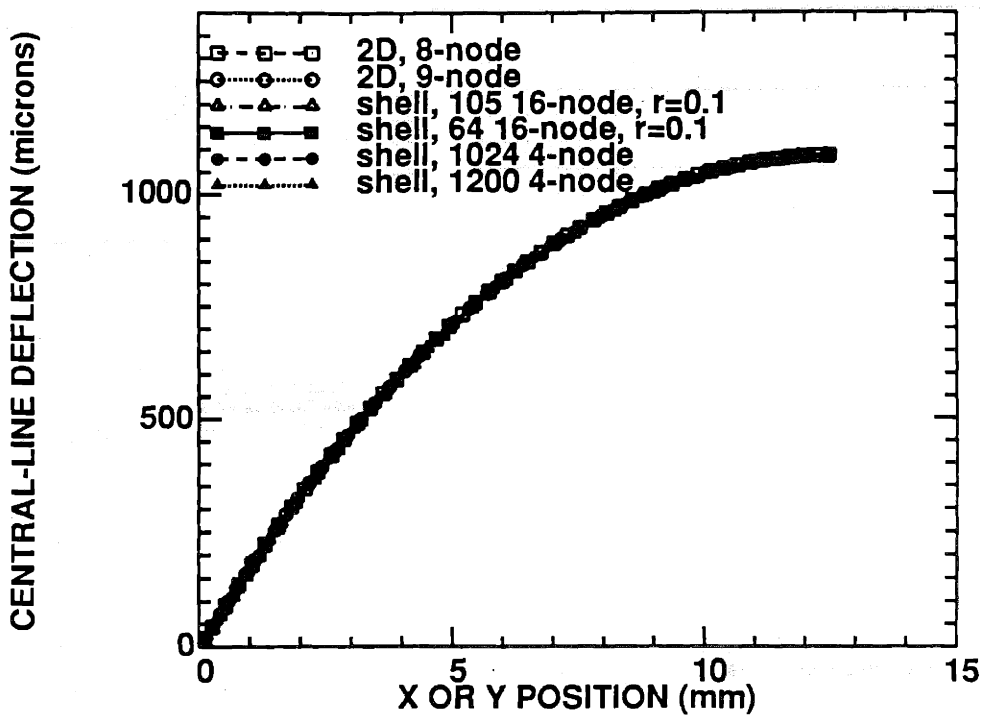

Figure 4.6b The deflection shapes for circular films with six different elements: shell 4-node (with and without triangle elements), shell 16-node (with and without triangle elements), 2D-solid 8-node and 2D-solid 9-node elements.

4.3.3 Normalized Deflected Shapes

According to load-deflection relationship (Chapter 3), the center deflection of films is a function of film properties and geometries when pressure is constant. This section examines whether the deflected shapes are changed with film properties. Several deflected shapes were obtained from FEM by inputting different material properties. Table 4.2 shows the material parameters used and the corresponding center deflections. These shapes were normalized with the center deflection and the normalized shapes were then compared with each other.

Sample	Young's Modulus (MPa)	Poisson Ratio	Residual Stress (MPa)	Thickness (μm)	Center Deflection (μm)
standard	900	0.25	10	1	340.6
change E	4500	0.25	10	1	83.1
change ν	900	0.45	10	1	349.5
change σ_o	900	0.25	50	1	84.1
change t	900	0.25	10	5	82.9

Table 4.2 The change of material properties for the comparison of deflected shapes. The film radius was 6.5 mm for all samples.

Figure 4.7 shows the normalized deflection shapes with different material parameters. One of the deflected shapes in Fig. 4.7 was called the standard. There were other four deflected shapes from different material properties (Table 4.2). For each of these four deflected shapes, only one material parameter was changed. It was found that the normalized shapes were almost the same despite the difference in deflections. That means the shapes after normalization were still the same, even though the center deflections

were changed with different material properties. More discussion about the deflection shape is presented in Section 4.3.5.

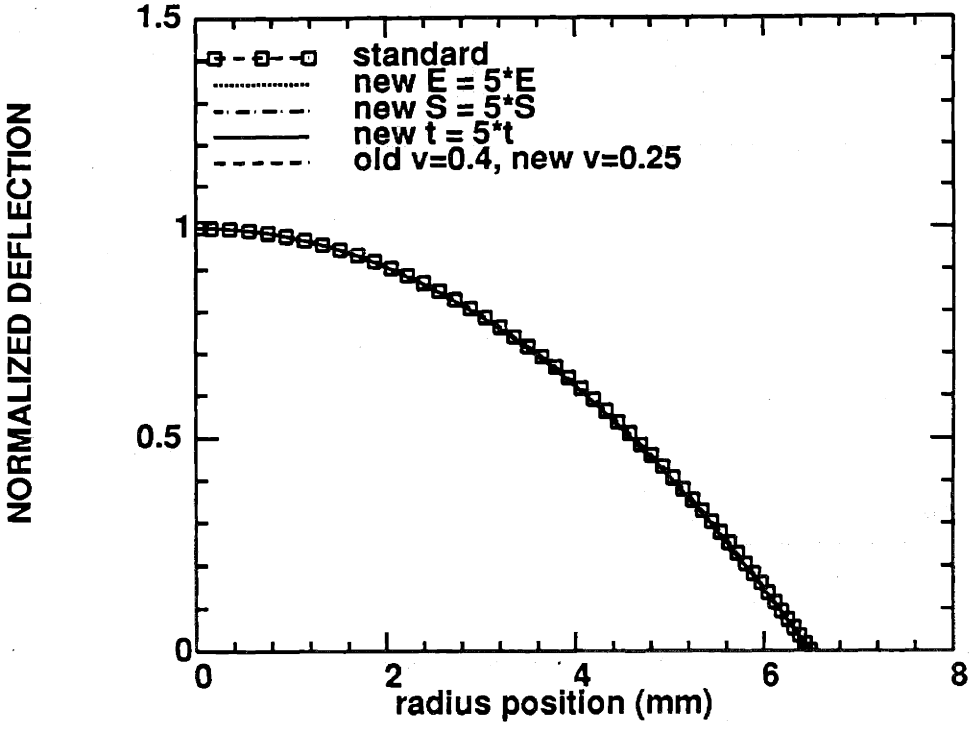

Figure 4.7 The normalized deflection shapes for circular films with different material properties. The material properties were shown in Table 4.2.

4.3.4 Comparison of Deflected Shapes

Figure 4.8 shows the comparison of the normalized deflected (square) shapes from experiments with those predicted from FEM and analytical models. Two different deflected shapes were plotted: center-to-midpoint shapes (Fig. 4.8a), and diagonal of the deflected shapes (Fig. 4.8b). The diagonal deflected shapes in Fig. 4.8b show a lower slope at corners, which implies a higher degree of constrains at corners. The analytical model for Fig. 4.8 was from Eq. 3.45:

$$w = d\cos\left(\frac{\pi x}{2a}\right)\cos\left(\frac{\pi y}{2a}\right) \tag{4.1}$$

where x and y are the position in x- and y-direction, d is the center deflection, and w is the deflection height. As seen in Fig. 4.8, the difference between the experimental data and the FEM results is within 0.5% in both diagonal and center-to-midpoint shapes. The difference between the experimental data and the analytical model is over 10% at the normalized position around 0.6.

Figure 4.9 is the comparison of the normalized deflected shapes for circular films among experimental data, FEM simulation, and the analytical model. The shape from analytic solutions was assumed to be a hemispheric function (Eqs. 3.1 and 3.2)

$$w = \left(R^2 - r^2\right)^{1/2} - (R-d) \tag{4.2}$$

where r is the radius position on the film, R the radius of curvature of the deflected membrane, and d the center deflection. The value of R can be calculated by

$$R = \frac{a^2}{2d} + \frac{d}{2} \tag{4.3}$$

where a is the radius of the circular film. It was found that both FEM and analytical model were in good agreement with the experimental data (Fig. 4.9). The difference among them was within 3%. This indicated that the actual circular deflected shape was very close to a hemispheric function.

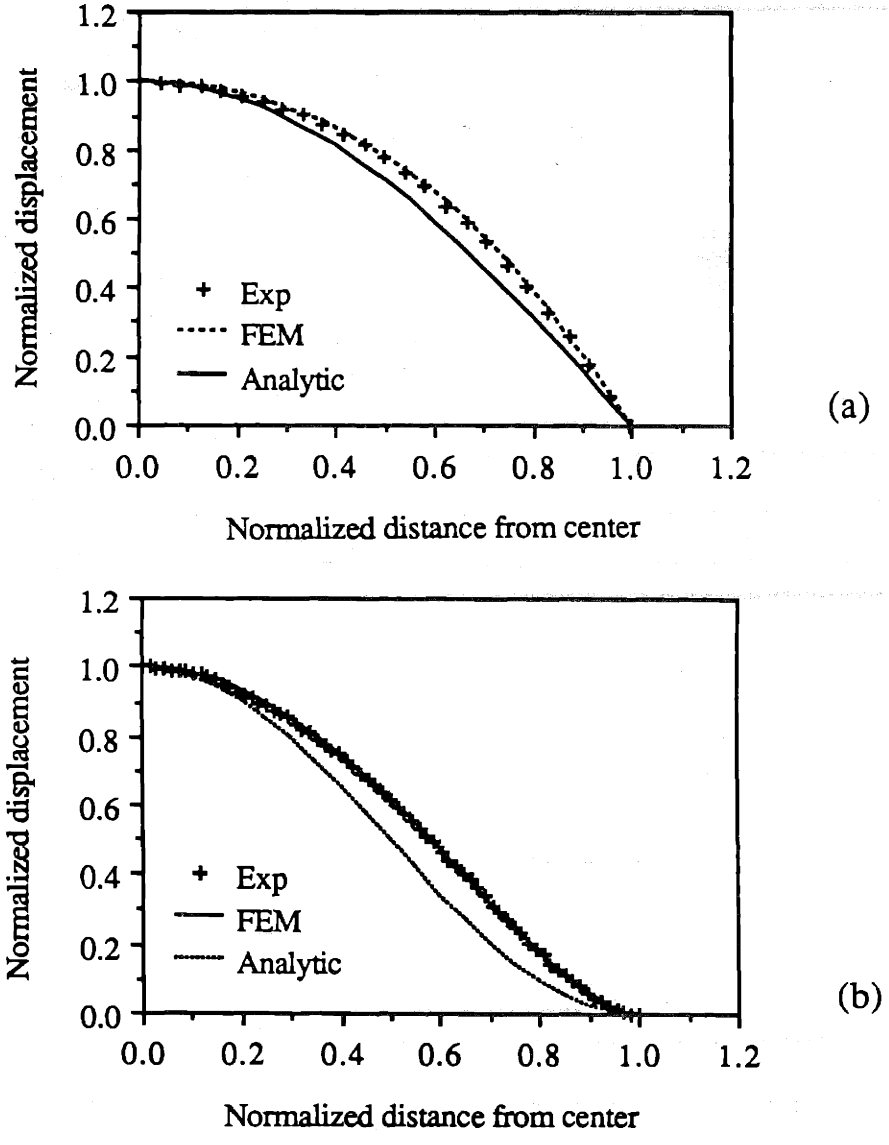

Figure 4.8 Experimental deflected shape versus FEM results and analytical model for square films: (a) along center-to-midside; (b) diagonal.

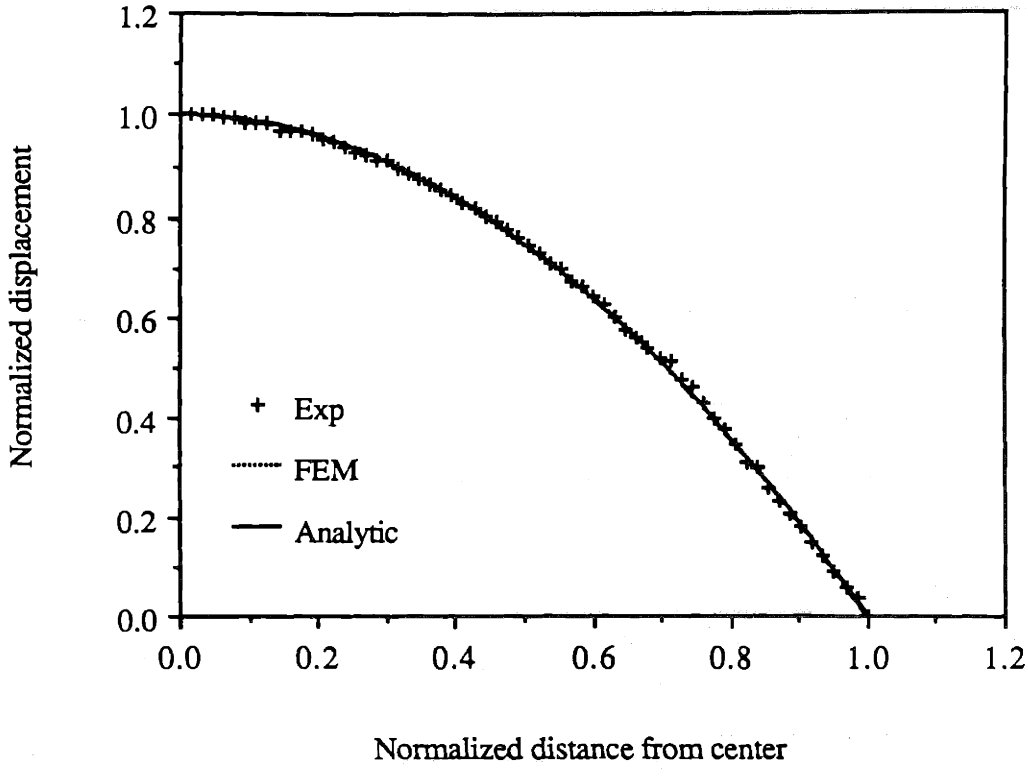

Figure 4.9 Experimental deflected shape versus FEM results and analytical model for circular films.

From the comparison of the shapes mentioned above, it is concluded that FEM generates the actual deflected shapes in both square and circular films. Hence, using FEM simulation to calculate the constants (C_1 and C_2, and $f(\nu)$) in the mathematical models is more accurate than using analytical solutions. The evaluation of the constants is presented in Sections 4.4 and 4.5.

4.3.5 Deflection Shape Change With Geometry

In the previous section, it was shown that the deflected shape predicted by a hemispheric function is very close to the FEM simulation. In this section, the FEM was used to simulate different deflected shapes with different geometries (such as thickness, and film size). The purpose is to show that the hemispheric function in the analytic solution can be used to predict the deflected shapes only when the film is very thin and/or the film size is very large.

The difference in deflected shapes between thin and thick films are shown in Fig. 4.10. It was found that when the film was very thick (e.g. 420μm), the slope of the deflection at edges was much lower (like a plate deflection), since thicker films have higher bending stiffness. For the case of thin film deflection (4.2μm, Fig. 4.10), the deflection at edges curves up very quickly. That is why the deflection shapes can be approximated by a hemispheric function (Section 4.3.4) since the hemispheric function results in a finite slope at film edges.

When using a larger film (i.e. the thickness-to-length ratio was decreased), the membrane-like deflection shape appeared again (Fig. 4.10). Therefore, it is concluded that the deflection shapes changes with thickness and/or with the thickness-to-length ratio of films, especially the radius of curvature at film edges is changed.

The results of this FEM analysis indicates that the normalized deflected shapes shown in Section 4.3.4 are a function of geometry. The hemispheric function is no longer valid for deflection shapes when films get thicker and/or when thickness-to-length ratio increases. Hence, using FEM is still the best available method to calculate the constants in the mathematical models.

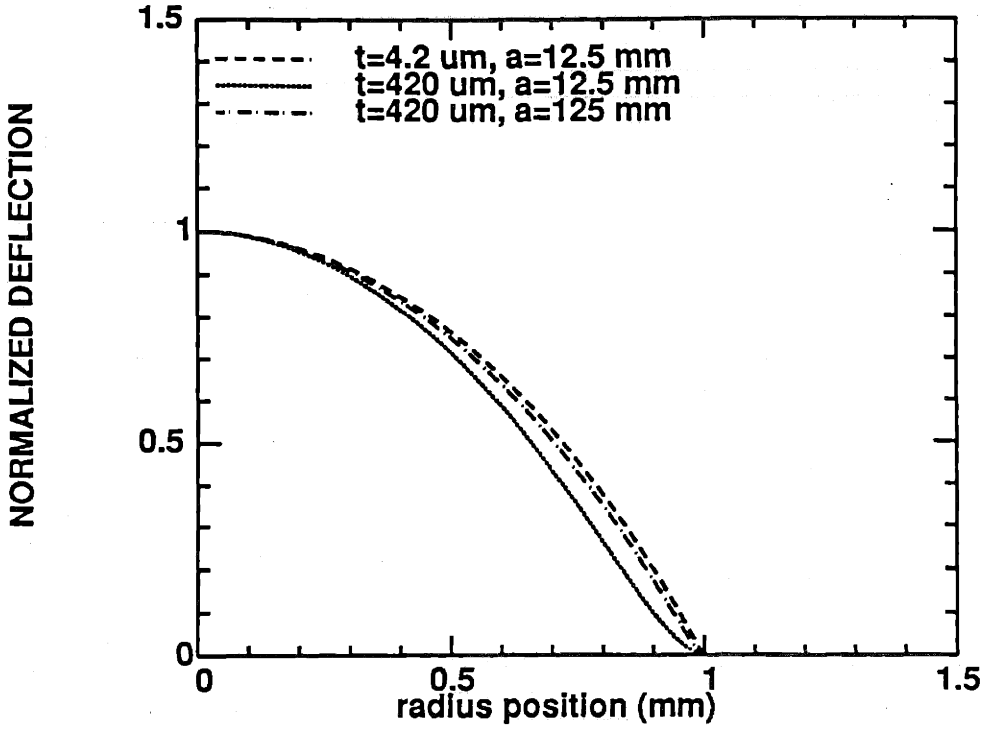

Figure 4.10 Deflected shapes from FEM with different film geometries.

4.4 Load-Deflection Behavior for Circular Single-Layer Films

In Chapter 3, two different models for circular single-layer films were developed: thin-film and thick-film models. In this section, the constants in these models are calculated using FEM. The procedures are as follows: (1) assume material properties of films as the input for FEM; (2) obtain the FEM results as a set of pressure-deflection data; (3) plot the FEM pressure-deflection data (details follow) and use the least-square curve fitting method to extract the constants from the fitting results.

4.4.1 The Constants in the Circular Thin-Film Model

Figure 4.11 shows the typical FEM results of pressure versus deflection. From the thin-film model (Eq. 3.25), the relationship between pressure and deflection is

$$\frac{Pa^2}{td} = C_2 f(\nu) \frac{E}{(1-\nu)} \left(\frac{1}{a^2}\right) d^2 + C_1 \sigma_o \tag{4.4}$$

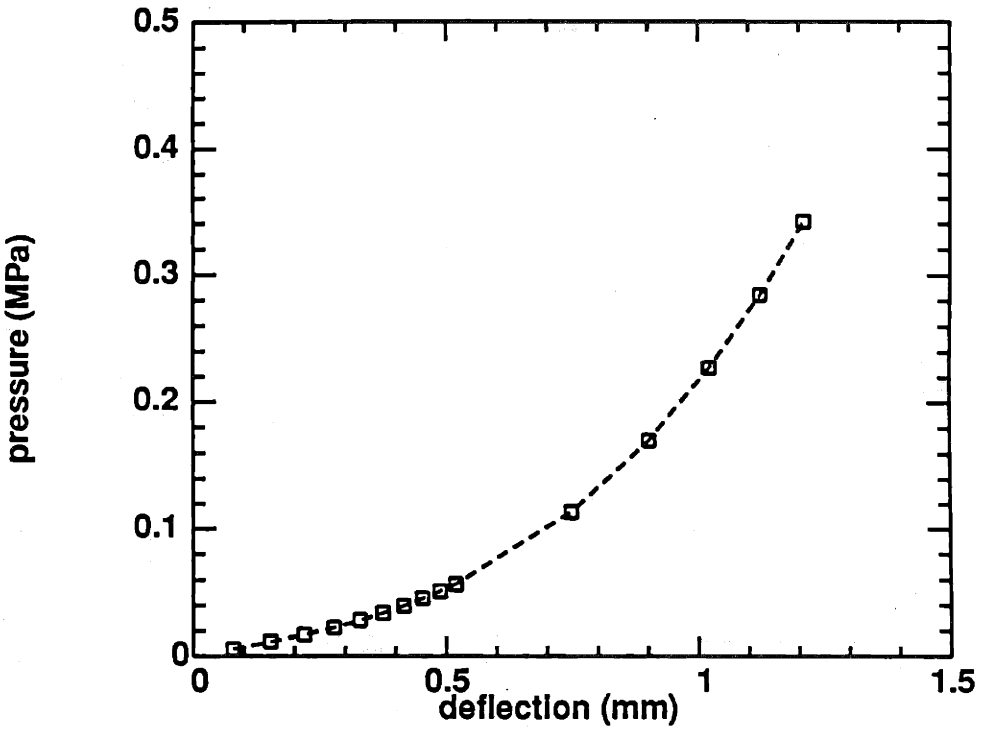

Figure 4.11 Typical FEM results in a P versus d plot.

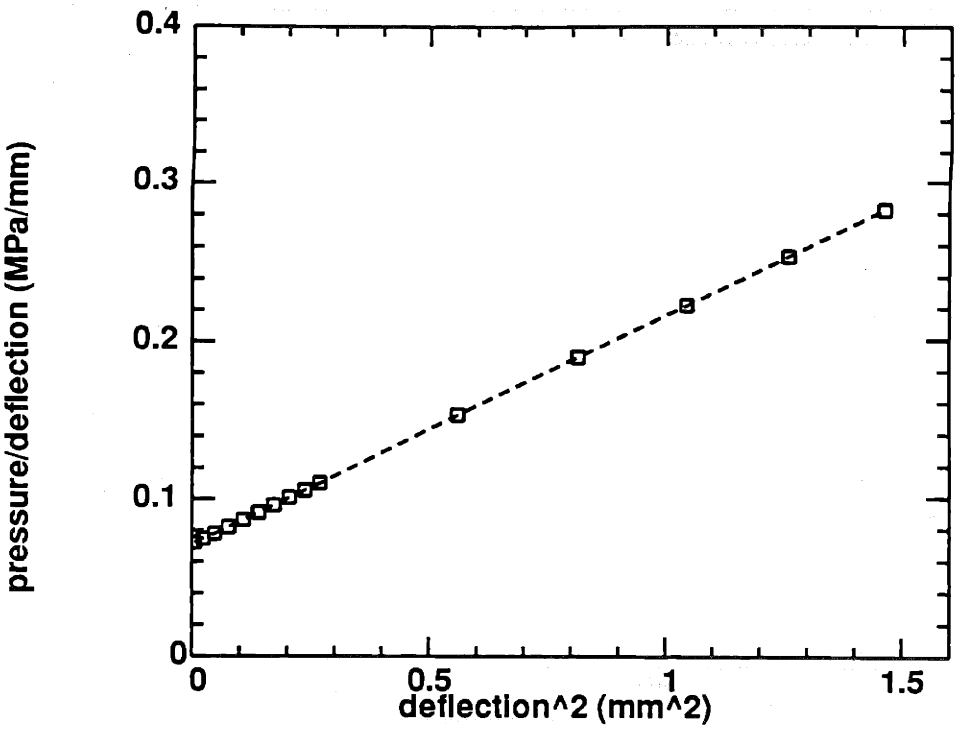

Figure 4.12 Typical FEM results in a P/d versus d^2 plot.

Figure 4.12 shows the FEM pressure-deflection results in a Pa^2/td versus d^2 plot. Therefore, a least-square fitting for a straight line was generated. Since the material properties and geometries of films were already known (such as t, a, E, ν, and σ_o), two constants ($C_2 f(\nu)$ and C_1) were calculated from the slope and the intercept of the linear fitting. Since the constant $C_2 f(\nu)$ was Poisson ratio-dependent, several different sets of material properties including different Poisson ratios were used in FEM analysis. The entire procedure for calculating the constants was then repeated to obtain the Poisson ratio-dependent function. The results are shown in Eq. 4.5 [62]:

$$C_2 = 2.667, \quad f(\nu) = \frac{1}{1.026 + 0.233\nu}, \quad C_1 = 4.00 \tag{4.5}$$

For convenience, the constant C_2 in Eq. 4.5 was chosen to be the same as the constants in Beams' equation (Eq. 3.8). Actually, the constants C_2 and $f(\nu)$ are not separable and C_2 can be any arbitrary number as long as the value of $C_2 f(\nu)$ is consistent. The constant C_1 was found not to be a function of Poisson ratio, as predicted by the analytic model (Eq. 3.31) and confirmed by FEM. As also shown in analytic models, these constants are not a function of material properties and film sizes (such as σ_o, E, t, and a). This was also verified by FEM analysis using different material properties and sizes as FEM input.

4.4.2 The Constants in the Circular Thick-Film Model

When the thickness of films is increased, the thin-film model may not be valid (details in Section 4.4.3). Thus, the thick-film model has to be used (Eq. 3.45)

$$\frac{Pa^2}{td} = C_2 f(\nu)\left(\frac{E}{a^2(1-\nu)}\right)d^2 + C_3\left(\frac{Et}{a^2(1-\nu)}\right)d + C_4\left(\frac{Et^2}{a^2(1-\nu)}\right) + C_1\sigma_o \tag{4.6}$$

$$= C_2 f(\nu)\left(\frac{E}{a^2(1-\nu)}\right)d^2 + C_3\left(\frac{Et}{a^2(1-\nu)}\right)d + C \tag{4.7}$$

where C, in Eq. 4.7, is the summation of the two d-independent terms in the right-hand-side of Eq. 4.6. There are now two more terms in the pressure-deflection relationship (Eq. 4.6): the terms led by constants C_3 and C_4. Then the linear least-square fitting was not suitable for the plot of P/d versus d^2. Hence, a second order polynomial curve fitting for the P/d versus d plot has to be used. The values of C_2, C_3, and C in Eq. 4.7 were determined from the coefficients of the fitting.

Through a series of FEM simulations with different film thickness (and no change of the material properties), the values of C_2, C_3, and C were obtained as a function of thicknesses. Figure 4.13 shows the FEM results on a plot of P/d versus d with different film thickness. The calculated constants for the thick-film model are shown in Table 4.3. Since the value of C was a function of thickness, a plot of C versus t^2 was obtained (Fig. 4.14). From the linear least-square fitting on such a plot, the values of C_4 and C_1 were calculated from the slope and the intercept. The values of C_4 and C_1 were found to be 13.3 and 4.00, respectively. It is seen in Table 4.3 that the constant C_3 changes as thickness is changed. This is partially because the C_3 term is relatively small compared to the C_2 term (The C_3 term is only about 1.2%-2.8% of the C_2 term for the FEM analyses shown in Table 4.3). Therefore, the variation in determining the constant C_3 through the curve fitting of P/d versus d is higher.

Thickness (μm)	$C_2 f(\nu=0.4)$	C_3	C (MPa)
5	2.332	5.62	40.040
20	2.316	2.53	40.261
50	2.314	1.29	41.246
70	2.331	0.65	42.348

Table 4.3 The results of FEM simulations for circular thick-film model with different thickness. The FEM inputs were: a=6.5mm, E=900MPa, ν=0.25, and σ_o=10MPa. Using a polynomial curve fitting, the values of C_4 and C_1 were calculated to be 13.3 and 4.005, respectively.

Using different Poisson ratios as the FEM input, the Poisson ratio-dependence was examined. The values of $C_2 f(\nu)$ was found to be the same as Eq. 4.5 within 1%. The values of C_3 and C_4 (at ν=0.25 and t=70μm) were calculated to be 0.80 and 13.2, respectively. Comparing these values with the values at ν=0.4 (C_3 and C_4 were 0.65 and

13.3, respectively, in Table 4.3), it is found that the constant C_4 is almost independent of Poisson ratio. Whether the constant C_3 is Poisson ratio dependent is not clear since the variation in determining the value of C_3 is high (Table 4.3), but in any event, it will be shown that the C_3 term can be neglected even in the thick-film model.

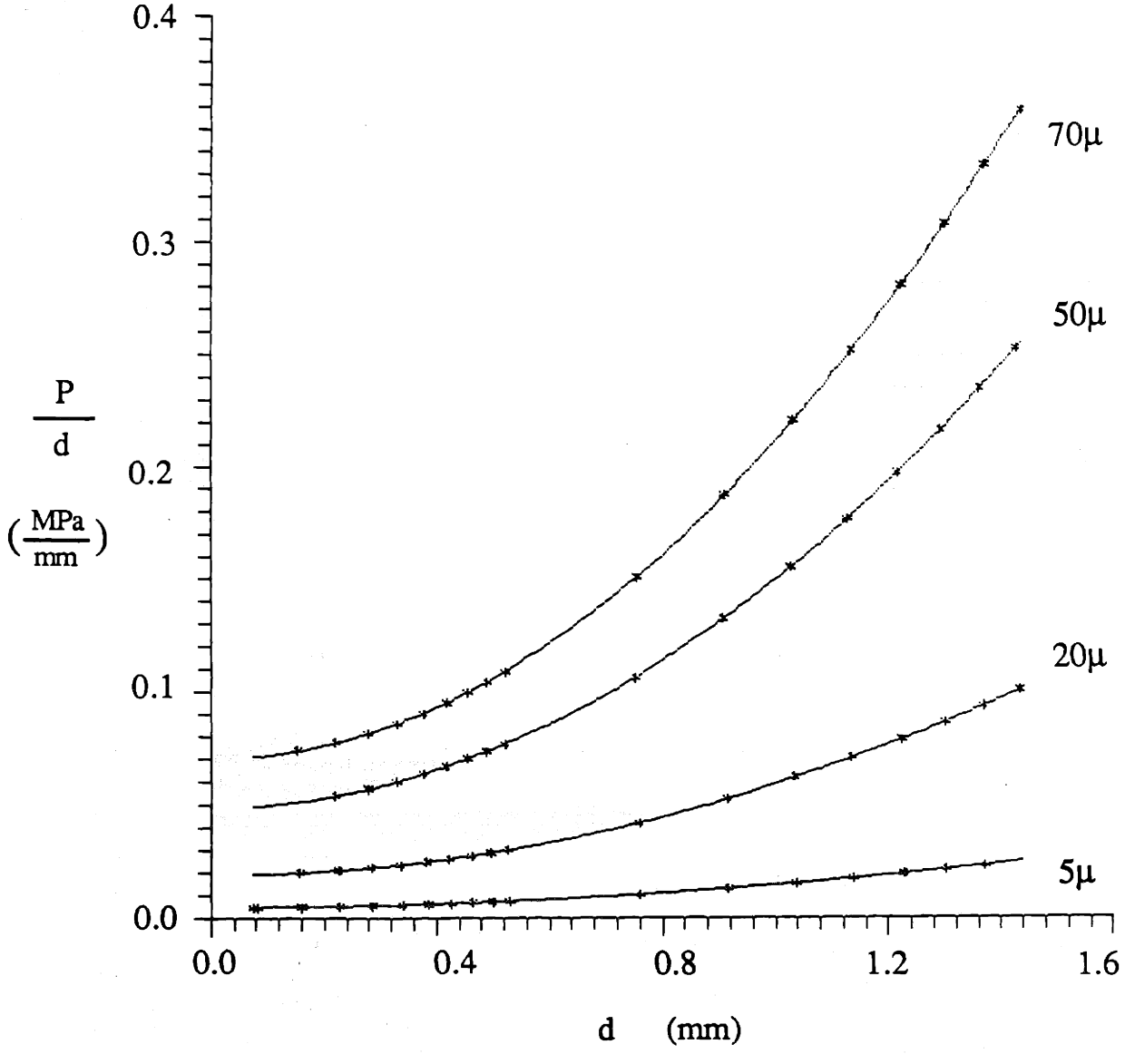

Figure 4.13 The FEM results in a P/d versus d plot with different thicknesses.

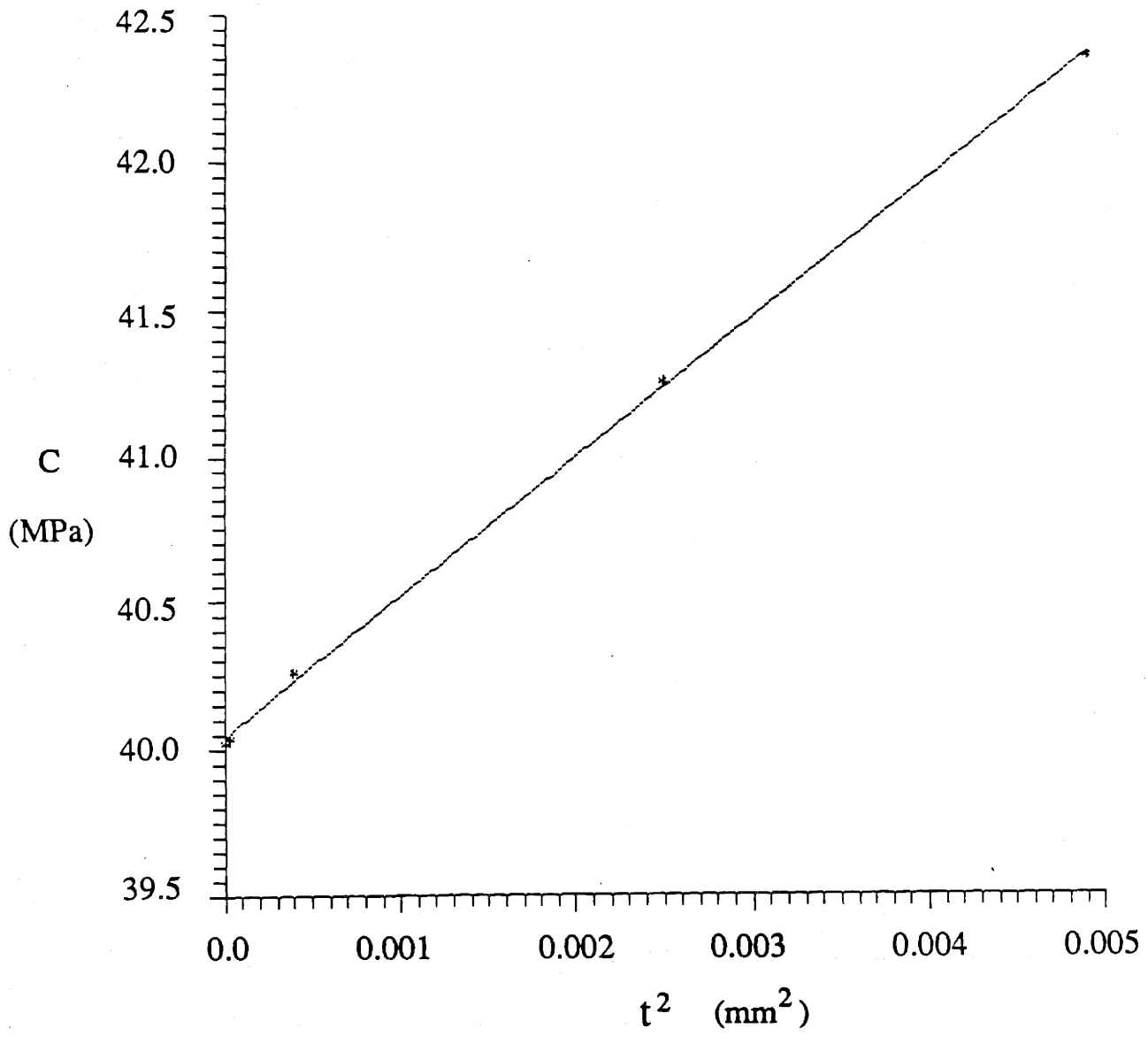

Figure 4.14 The constant C versus the square of the thickness. The constants C_4 and C_1 can be calculated for the slope and the intercept.

With the C_3 term omitted, the relationship of pressure and deflection is

$$\frac{Pa^2}{td} = C_2 f(\nu)\left(\frac{E}{a^2(1-\nu)}\right)d^2 + C_4\left(\frac{Et^2}{a^2(1-\nu)}\right) + C_1\sigma_o \qquad (4.8)$$

$$= C_2 f(\nu)\left(\frac{E}{a^2(1-\nu)}\right)d^2 + C \qquad (4.9)$$

Where the constant C is the same as that in Eq. 4.7. Equation 4.8 is called the simplified thick-film model. A new set of constants was calculated from a plot of P/d versus d^2 using linear least-square fitting without C_3. The results are shown in Table 4.4. The constants C_4 and C_1 were evaluated from a plot of C versus t^2 and were 14.4 and 4.045, respectively. After dropping the whole C_3 term, the changes of the constants C_2 and C_1 were within 1%, while the change of the constant C_4 was about 8% (Tables 4.3 and 4.4). The relatively large change of the values of C_4 is partly due to the small C_4 term compared to the C_1 term. More discussion about these different models is given in the following section.

Thickness (μm)	$C_2 f(\nu=0.4)$	C (MPa)	C_4 term/C_1 term
5	2.335	40.245	0.03%
20	2.344	40.770	0.47%
50	2.354	41.973	3.1%
70	2.359	42.828	6.2%

Table 4.4 The results of FEM simulations fitted without the C_3 term (for the simplified thick-film model). The FEM inputs were the same as those in Table 4.3. The values of C_4 and C_1 were 14.4 and 4.045, respectively.

4.4.3 Discussion of Models for Circular Films

The summary of the constants in thin-film (Eq. 4.4), thick-film (Eq. 4.6), and simplified thick-film (Eq. 4.8) models is shown in Table 4.5. Several conclusions are drawn from a comparison of the constants in these models.

Model	C_2 f(ν=0.4)	C_3	C_4	C_1
thin-film	2.35	-	-	4.00
thick-film	2.323	1.85	13.44	4.005
simplified thick-film	2.348	-	14.40	4.045

Table 4.5 Summary of the constants for three different models. The Poisson ratio was assumed to be 0.25 in all models.

First, the values of $C_2 f(\nu)$ and C_1 are very consistent no matter which models are used. This indicates that the difference in the biaxial modulus evaluated from any model is within 1%. Second, the values of $C_2 f(\nu)$, C_4, and C_1, in simplified thick-film model are in good agreement with the values of thick-film model constants. The differences between these constants are less than 1% except for the value of C_4 (about 8%, Tables 4.3 and 4.4). This confirms the assumption that the C_3 term in thick-film model is insignificant.

Third, using thin-film model to solve residual stress in a thick film causes a problem of accuracy. Comparing the thin-film and simplified thick-film models (Eqs. 4.4 and 4.8), both are a straight line in a P/d versus d^2 plot. However, the intercept of the straight line contains both C_4 and C_1 terms in the simplified thick-film model, while it only contains the C_1 term in the thin-film model. When the entire C_4 term is small (i.e. thickness is small), the evaluation of residual stress from either model is about the same. When the film is thick, residual stress would be overestimated if the thin film model is

applied to thick films. The higher the C_4 term is, the larger the error is. Equation 4.10 shows the ratio of the C_4 term over the C_1 term.

$$\frac{C_4 \text{ term}}{C_1 \text{ term}} = \frac{C_4 E t^2}{C_1 \sigma_o a^2 (1-\nu)} \tag{4.10}$$

The ratio of C_4 term over C_1 term indicates the overestimated error of using thin-film model for thick-film deflection. In the example shown in Table 4.4, there is about 6.2% error in using a thin-film model to calculate the residual stress of a 70μm film. This error is called the thickness effect, since the thickness of film plays an important role (The C_4 term depends on the square of film thickness). As seen in Eq. 4.10, this ratio also varies with other material properties and film sizes; it increases as the biaxial modulus increases or, as the residual stress and/or the film size decreases.

4.5 Load-Deflection Behavior for Square Films

The forms of pressure-deflection relationship for square films are the same as those for circular films. Thus, the procedures for determining the constants in the mathematical models for square films are also the same as the procedures shown in Section 4.4 for circular films. As mentioned in previous sections, there are three mathematical models to be discussed: thin-film, thick-film, and simplified thick-film models. All the constants in these three models for square films are calculated in Sections 4.5.1 to 4.5.3.

4.5.1 The Constants in the Square Thin-Film Model

The thin-film model for square films is given as Eq. 4.4 (Section 4.4.1).

$$\frac{Pa^2}{td} = C_2 f(\nu) \frac{E}{(1-\nu)} \left(\frac{1}{a^2}\right) d^2 + C_1 \sigma_o \tag{4.4}$$

The simulation was done using the following film properties and geometries: half-size=4.826mm, $E/(1-\nu)$=5740MPa, σ_o=33.87MPa, and t=5.2μm. The FEM simulated results were plotted as P/d versus d^2. Since the material properties were known, the constants (C_1 and $C_2 f(\nu)$) at certain Poisson ratio were calculated. The constants (C_1 and $C_2 f(\nu)$) were evaluated as a function of Poisson ratio by changing the values of Poisson ratio from 0.1 to 0.5. Using curve fitting, the constant $C_2 f(\nu)$ was presented as a function of Poisson ratio:

$$C_2 f(\nu) = 1.981 - 0.585\ \nu\ ; \qquad C_1 = 3.41 \tag{4.11}$$

For convenience, the constant C_2 was arbitrarily chosen as $C_2 f(\nu=0.25)$. Thus, Eq. 4.11 can be rewritten as

$$C_2 = 1.37\ ; \qquad f(\nu) = 1.446 - 0.427\ \nu\ ; \qquad C_1 = 3.41 \tag{4.12}$$

4.5.2 The Constants in the Square Thick-Film Model

The thick-film model is applied to the deflection of a thick film (Eqs. 4.6 and 4.7, in Section 4.4.2):

$$\frac{Pa^2}{td} = C_2 f(\nu)\left(\frac{E}{a^2(1-\nu)}\right)d^2 + C_3\left(\frac{Et}{a^2(1-\nu)}\right)d + C_4\left(\frac{Et^2}{a^2(1-\nu)}\right) + C_1\sigma_o \tag{4.6}$$

$$= C_2 f(\nu)\left(\frac{E}{a^2(1-\nu)}\right)d^2 + C_3\left(\frac{Et}{a^2(1-\nu)}\right)d + C \tag{4.7}$$

Again, the P/d versus d plots were used since there were two more terms in the pressure-deflection relationship. Hence, from a second order polynomial curve fitting of the FEM pressure-deflection results, the values of $C_2 f(\nu)$, C_3, and C in Eq. 4.7 were determined. The calculated constants for the thick-film model are shown in Table 4.6.

Thickness (μm)	C_2 f(ν=0.45)	C_3	C (MPa)
5.2	1.728	-0.86	115.70
20	1.728	-0.25	117.96
50	1.727	-0.12	122.87
70	1.725	-0.09	126.42

Table 4.6 The results of FEM simulations for square thick-film model with different thickness. The FEM inputs were: a=4.826mm, E=3157MPa, ν=0.45, and σ_o=33.87MPa. Using a polynomial least-square fitting, the values of C_4 and C_1 were calculated to be 8.57 and 3.44, respectively.

Through a series of FEM simulations with different film thicknesses, a plot of C versus t^2 was obtained. From the linear least-square fitting on the plot of C versus t^2, the values of C_4 and C_1 were calculated from the slope and the intercept. The values of C_4 and C_1 were 8.57 and 3.44, respectively.

Using different Poisson ratios as the FEM input, the Poisson ratio-dependence of the value of $C_2 f(\nu)$ was found to be the same as Eq. 4.12 within 1%. The values of C_3 and C_4 (at ν=0.25 and t=5.2μm) were calculated to be -0.89 and 8.56, respectively. Comparing these values with the values at ν=0.45 (C_3 and C_4 were -0.80 and 8.57, respectively), it is again found that the constant C_4 is almost independent of Poisson ratio. The Poisson ratio dependence of the constant C_3 is not clear due to a large variation in determining the value of C_3 (Table 4.6).

However, as shown in previous sections, the C_3 term can be neglected since the value of the C_3 term is small compared to the C_2 term. This leads to the simplified thick-film model (Eqs. 4.8 and 4.9):

$$\frac{Pa^2}{td} = C_2 f(\nu)\left(\frac{E}{a^2(1-\nu)}\right)d^2 + C_4\left(\frac{Et^2}{a^2(1-\nu)}\right) + C_1\,\sigma_o \tag{4.8}$$

$$= C_2 f(\nu)\left(\frac{E}{a^2(1-\nu)}\right)d^2 + C \tag{4.9}$$

Revised constants for these equations were determined from the plot of P/d versus d^2. As shown previously, a series of FEM simulations were done as a function of thickness, so that the constant C_4 and C_1 can be calculated by linear curve fitting to a plot of C versus t^2. The results are shown in Table 4.7.

Thickness (μm)	C_2 f(ν=0.45)	C (MPa)	C_4 term/C_1 term
5.2	1.715	115.63	0.049%
20	1.714	117.88	0.072%
50	1.710	122.79	0.45%
70	1.707	126.33	0.89%

Table 4.7 The results of FEM simulations fitted without the C_3 term (for the simplified thick-film model). The FEM inputs were the same as those in Table 4.6. The values of C_4 and C_1 were 8.56 and 3.44, respectively.

4.5.3 Discussion of Models for Square Films

The summary of thin-film (Eq. 4.4), thick-film (Eq. 4.6), and simplified thick-film (Eq. 4.8) models is shown in Table 4.8. The values of $C_2 f(\nu)$ and C_1 are very consistent for all the three models. Comparing the thick-film model with the simplified thick-film model, the change in all the constants ($C_2 f(\nu)$, C_4, and C_1) is within 1%. This confirms the assumption that the C_3 term in thick-film model is insignificant. The situations are the same as for circular films.

Model	C_2 f(ν=0.45)	C_3	C_4	C_1
Thin-Film	1.718	-	-	3.41
Thick-Film	1.727	-0.3	8.57	3.44
Simplified Thick-Film	1.712	-	8.56	3.44

Table 4.8 Summary of the constants for three different models. The Poisson ratio was assumed to be 0.45 in all models.

The ratios of the C_4 term over the C_1 term are shown in Table 4.8. Compared to Table 4.4, these ratios are smaller than those for circular films. As shown in Eq. 4.10, the ratio is dependent on material properties and film geometries. Hence, this indicates that the examples shown in Table 4.8 have a very low thickness effect which is discussed in Section 4.4.3.

4.6 Mathematical Models for Multi-layer Films

In the following sections, the mathematical models for the load-deflection behavior of multi-layer films are generated. As shown in Chapter 3, multi-layer models for both circular and square films were derived from analytical solutions. Since the deflected shapes predicted by analytic solutions were not accurate (Section 4.3.4), FEM analysis is used here to derive the pressure-deflection relationship for both square and circular multi-layer films.

4.6.1 Circular Films

The FEM simulation was done using 2D-solid 8-node elements and each layer has 250 elements (Table 4.1). A bi-layer structure was built for FEM analysis. The properties of these two layers are shown in Table 4.9. Each layer has different biaxial modulus,

thickness, and residual stress. Figure 4.15 shows the deflection results of FEM of the bi-layer with reverse sequences. The results show that the difference between two sequences was very small (less than 0.3%). This indicates that a summation type of formula is suitable for the deflection of multi-layer films. Actually, the analytic solution also predicted a similar formula for multi-layer films (Eqs. 3.77 and 3.78, Chapter 3). Therefore, the pressure-deflection relationship can be expressed as

$$\frac{Pa^2}{d} = \left(\frac{d^2}{a^2}\right)\sum_{i=1}^{n}\left(\frac{C_{2i}f(\nu_i)E_it_i}{1-\nu_i}\right) + \left(\frac{d}{a^2}\right)\sum_{i=1}^{n}\left(\frac{C_{3i}E_it_i^2}{1-\nu_i}\right) + \left(\frac{1}{a^2}\right)\sum_{i=1}^{n}\left(\frac{C_{4i}E_it_i^3}{1-\nu_i}\right) + C_1\sum_{i=1}^{n}\sigma_{oi}t_i \tag{4.13}$$

where the subscript i indicates the i-th layer of the films and there are n total layers in the multi-layer structure.

Layers	Young's Modulus (MPa)	Poisson Ratio	Thickness (μm)	Residual Stress (MPa)
first	900	0.4	5	10
second	100	0.4	25	1.1

Table 4.9 The properties of the circular bi-layer films for FEM analysis. The radius of the circular film was 6.5mm.

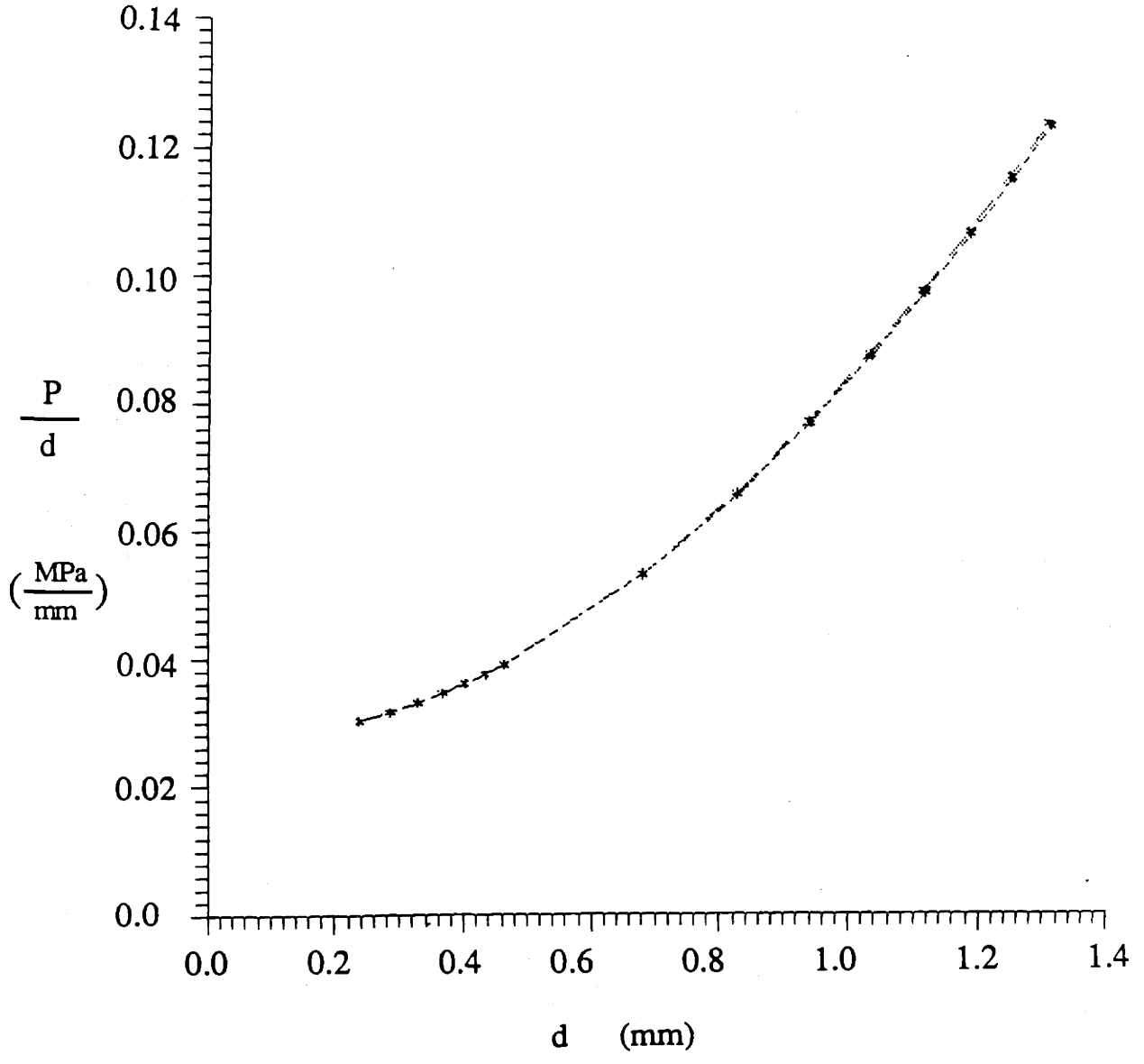

Figure 4.15 The FEM results of circular bi-layer films with reverse sequences. The material properties of films were shown in Table 4.9.

To prove Eq. 4.13, the results in Fig. 4.15 were subjected to a second order polynomial curve fitting. The expression for the curve was given as

$$P/d = 0.0542\, d^2 + 0.00146\, d + 0.0265 \qquad \text{(MPa/mm)} \qquad (4.14)$$

Using the material parameters of individual layers listed in Table 4.9 and the constants available for the single-layer model (Eq. 4.5 and Table 4.4), Eq. 4.13 was given by

$$P/d = 0.0549\, d^2 + 0.00154\, d + 0.0265 \qquad \text{(MPa/mm)} \qquad (4.15)$$

The difference (between Eq. 4.14 and Eq. 4.15) in the d^2 term is within 1.3% and no significant difference was found in the d-independent term. The difference in the d term was about 5%, which is partly due to the relatively small size of the d term. The comparison between Eqs. 4.14 and 4.15 indicates that Eq. 4.13 can be used to predict multi-layer load-deflection behavior using material parameters of individual layers.

As seen in the simplified thick-film model, the C_3 term was neglected since the C_3 term is very small compared to the C_1 term (Eq. 4.8). Thus, Eq. 4.13 can be simplified as

$$\frac{Pa^2}{d} = \left(\frac{d^2}{a^2}\right)\sum_{i=1}^{n}\left(\frac{C_{2i}f(\nu_i)E_it_i}{1-\nu_i}\right) + \left(\frac{1}{a^2}\right)\sum_{i=1}^{n}\left(\frac{C_{4i}E_it_i^3}{1-\nu_i}\right) + C_1\sum_{i=1}^{n}\sigma_{oi}t_i \qquad (4.16)$$

As shown in the previous sections, the constants of the simplified thick-film model (Eq. 4.16) were the same as those in the thick-film model (Table 4.4). Equation 4.16 is used as the multi-layer model in Chapter 5 to evaluate the biaxial modulus and residual stress for circular films.

4.6.2 Square Films

As expected, the multi-layer model for deflection of square films has the same form as circular films (Eq. 4.13). A bi-layer structure was built for FEM analysis. Table 4.10 shows the material parameters for individual layers in the bi-layer film. Both 3D-solid ratioed elements and shell 4-node regular elements were used for FEM analysis (Table 4.1). For shell elements, an artificial linkage between two layers was needed due to the nature of the element. The results are shown in Fig. 4.16. The difference between these two types of elements was less than 0.5%. This indicates that the FEM was consistent using these two types of elements.

Layers	Young's Modulus (MPa)	Poisson Ratio	Thickness (μm)	Residual Stress (MPa)
first	2910	0.25	5	28.7
second	900	0.4	25	10

Table 4.10 The properties of the circular bi-layer films for FEM analysis. The size of the square film was 8x8 mm.

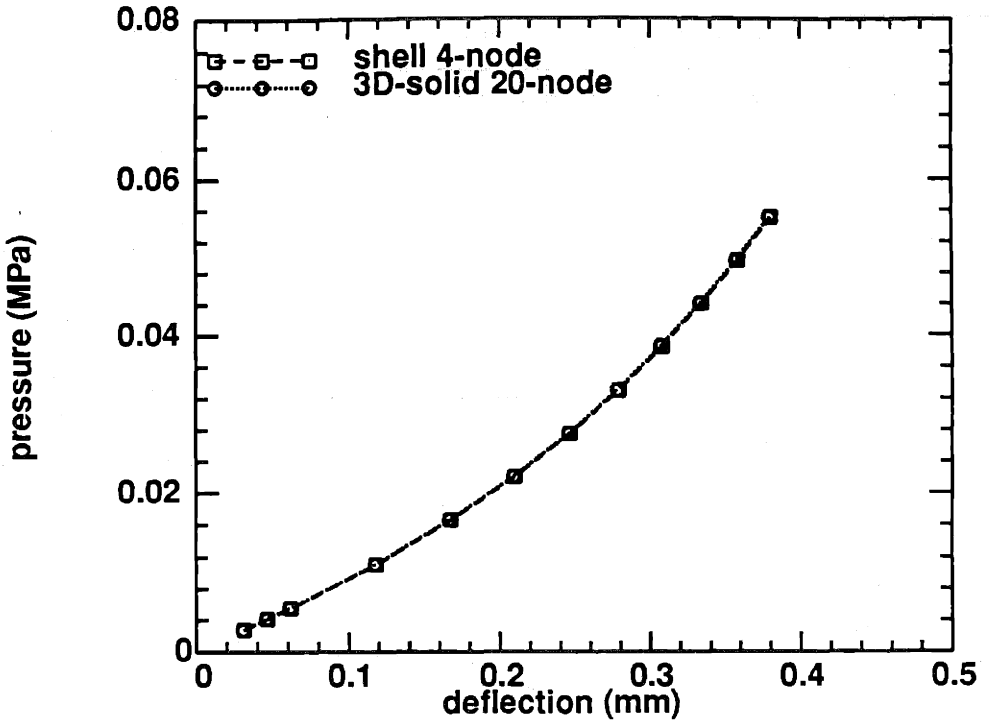

Figure 4.16 The FEM results of square bi-layer films with different elements. The material properties of films were shown in Table 4.10.

Figure 4.17 shows the deflection results of FEM of the bi-layer with reverse sequences. Again, the results show that the difference between two sequences was very small (less than 0.3%). Therefore, the pressure-deflection relationship was expressed as Eq. 4.13:

$$\frac{Pa^2}{d}=\left(\frac{d^2}{a^2}\right)\sum_{i=1}^{n}\left(\frac{C_{2i}f(\nu_i)E_it_i}{1-\nu_i}\right)+\left(\frac{d}{a^2}\right)\sum_{i=1}^{n}\left(\frac{C_{3i}E_it_i^2}{1-\nu_i}\right)+\left(\frac{1}{a^2}\right)\sum_{i=1}^{n}\left(\frac{C_{4i}E_it_i^3}{1-\nu_i}\right)+C_1\sum_{i=1}^{n}\sigma_{oi}t_i \tag{4.13}$$

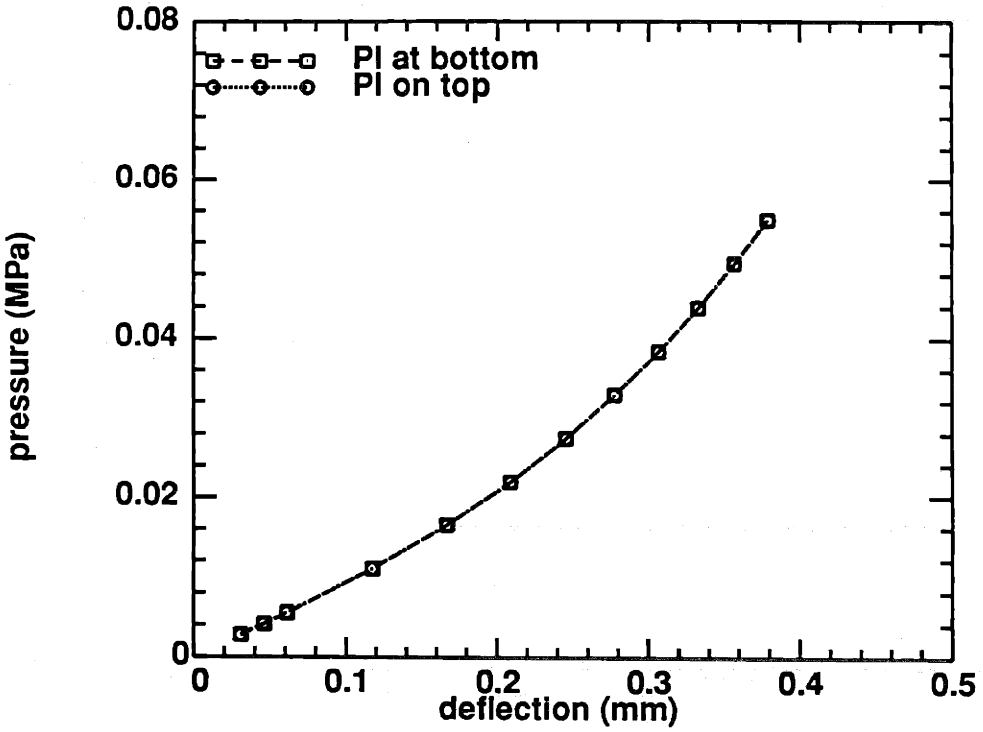

Figure 4.17 The FEM results of square bi-layer films with reverse sequences. The material properties of films were shown in Table 4.10.

To check the validity of Eq. 4.13 for square films, one of the curves in Fig. 4.17 was subjected to a second order polynomial curve fitting. The expression for the fitting was given as

$$P/d = 0.399\, d^2 - 0.0022\, d + 0.0877 \qquad \text{(MPa/mm)} \qquad (4.17)$$

Using the material parameters of individual layers listed in Table 4.10 and the constants available for the single-layer model (Eq. 4.12 and Table 4.6), Eq. 4.17 was expressed by

$$P/d = 0.0395\, d^2 - 0.0016\, d + 0.0840 \qquad \text{(MPa/mm)} \qquad (4.18)$$

The difference between Eq. 4.17 and Eq. 4.18 was within 1% in the d^2 term was about 4% in the d-independent term. The difference in the d term was larger since the d term was relatively small. Compared to Eq. 4.15 (circular equation), Eq. 4.18 (square equation) shows a slightly large error in the d-independent term. Nevertheless, the comparison between Eqs. 4.17 and 4.18 indicates that Eq. 4.13 is still reasonably good to use for predicting the load-deflection behavior of square multi-layer films.

Equation 4.16 is the simplified thick-film model for square multi-layer films:

$$\frac{Pa^2}{d} = \left(\frac{d^2}{a^2}\right)\sum_{i=1}^{n}\left(\frac{C_{2i}f(\nu_i)E_it_i}{1-\nu_i}\right) + \left(\frac{1}{a^2}\right)\sum_{i=1}^{n}\left(\frac{C_{4i}E_it_i^3}{1-\nu_i}\right) + C_1\sum_{i=1}^{n}\sigma_{oi}t_i \qquad (4.16)$$

where the constants are shown in Table 4.8. This equation is also used as the multi-layer model in Chapter 5 to evaluate the biaxial modulus and residual stress for square films.

CHAPTER 5

Mechanical Property Measurements

5.1 Introduction

The results of mechanical property measurements are presented in three sections: load-deflection behavior for single-layer films, load-deflection behavior for multi-layer films, and uniaxial tensile tests. Both square and circular films were fabricated for single-layer and multi-layer samples. From load-deflection experiments, the biaxial modulus and the residual stress of films were evaluated using the single-layer and the multi-layer models derived in Chapter 4. The results are presented in Section 5.2 (single-layer films) and in Section 5.3 (multi-layer films). From uniaxial tensile tests, Young's moduli of films were measured (Section 5.5). The in-plane Poisson ratios of films were calculated by comparing the values of Young's modulus and of the biaxial modulus (Section 5.5.5).

Several discussions about using the load-deflection technique are presented in this chapter as well. First, the errors in the load-deflection experiments were investigated (Section 5.2.3). Next, the solvent and the processing effects on the mechanical properties are discussed in Sections 5.2.4 and 5.2.5. Third, sensitivity of the mechanical measurements was analyzed in Sections 5.4.2 and 5.4.3, to understand whether the results of load-deflection tests are sensitive to the variation in thickness and material properties. Fourth, the variation in thickness was measured and discussed in Section 5.4.1. Finally, the effect of the strain rate on the measurements of the load-deflection test is given in Section 5.4.4.

		Sample Condition	E/(1-ν),or E GPa	σ_o, MPa	ε, %	Section #
Blister Test	APC (Circular)	As 1st layer	2.2±0.2	1.4±0.15	0.06±0.02	5.2.2
		As 2nd layer	2.1±0.3	1.5±0.4	0.07±0.03	5.3.2
		As 3rd layer	2.6±1	1.2±0.4	0.05±0.02	5.3.2
		Twice-cured	2.5±0.2	1.8±0.15	0.07±0.01	5.2.5
		Slow Strain Rate	1.94	1.43	0.074	5.4.4
	APC (Square)	As 2nd layer	2.3±0.3	11±2	0.48±0.15	5.3.2
		As 3rd layer	3.1±1	8.7±1.8	0.28±0.14	5.3.2
		As 4th layer	-	-	-	5.3.2
Tensile Test	APC single-layer	As 1st layer	1.20±0.01	-	-	5.5.2
	APC on PI	As 2nd layer	1.44±0.19	-	-	5.5.3
	APC single-layer	Twice-cured	1.44±0.08	-	-	5.5.4

Table 5.1 The summary of the precessing conditions and the corresponding results for APC.

Table 5.1 summarizes all the mechanical measurements for APC. The locations of the details of measurements are also listed in Table 5.1. Both APC-D and PEU were subjected to the similar mechanical tests and their results are shown in individual sections.

Table 5.2 summarizes the results of the mechanical measurements for PI. The results of solvent effect tests for PI are not shown here and will be shown in Table 5.4.

		Sample Condition	E/(1-ν),or E GPa	σ_o, MPa	ε, %	Section #
Blister Test	PI (Square)	As single-layer	5.38±0.4	33.4±3	0.62±0.02	5.2.2
		Test of Solvent Effect	-	-	-	5.2.4
Tensile Test	PI	As single-layer	3.2±0.3	-	-	5.5.2

Table 5.2 The summary of the precessing conditions and the corresponding results for PI. The results of solvent effect are listed in Table 5.4.

The results of mechanical properties of multi-layer coatings in Sections 5.2 and 5.3 were reported by Lin et al. at the 1990 Material Research Society Spring Conference [71]. The study of errors in the blister test (in Section 5.2.3) was carried out in conjunction with Mark G. Allen, Jeffrey Y. Pan, and Fariborz Maseeh of MIT.

5.2 Blister Tests on Single-Layer Films

5.2.1 Types of Samples

Both circular and square single-layer samples were fabricated for the blister test. PI (polyimide, BTDA-MPDA(40%)/ODA(60%)) was used to fabricate square samples. Circular films were made using three different coatings: acrylic polymer coating (APC), acrylic polymer coating with dispersed resin (APC-D), and polyester urethane (PEU). The

thickness was about 4 μm for PI and was about 30 μm for coatings. The details of sample fabrication are shown in Sections 2.3.1 and 2.4.

5.2.2 Residual Stresses and Biaxial Moduli of Polyimide and Coatings

The maximum deflection for polyimide with/without coatings did not exceed about 0.5% elongation on average (for experimental procedures, see Section 2.6.3). This ensured that the films remained in the linear elasticity regime when they were deflected. Therefore, the linear elasticity assumption for mathematical models was still valid. More discussion is given in Section 5.5.2.

For each type of film, at least four samples were measured. The load-deflection data for single-layer PI samples are shown in Fig. 5.1, plotted as Pa^2/dt versus $(d/a)^2$. Since the thicknesses of these single-layer samples were small, the thickness effect of these films was negligible (FEM analyses in Tables 4.4 and 4.8). Hence, the thin-film model (Eq. 4.4) was used to evaluate mechanical properties:

$$\frac{Pa^2}{dt} = C_2 f(\nu) \left(\frac{E}{1-\nu}\right)\left(\frac{1}{a^2}\right) d^2 + C_1 \sigma_o \tag{5.1}$$

where P is the applied pressure, d the center deflection, t the thickness, a the radius or half-edge of the membrane, E the Young's modulus, ν the in-plane Poisson ratio, $E/(1-\nu)$ the biaxial modulus, and σ_o the residual stress. The Poisson ratio of PI was assumed to be 0.4 and the Poisson ratios for APC, APC-D, and PEU were assumed to be 0.42, 0.34, and 0.3, respectively. Later in Section 5.5.5, uniaxial tensile tests confirm these assumptions. From the plot of Pa^2/dt versus d^2, the slope and the intercept can be expressed as:

$$Slope = C_2 f(\nu) \left(\frac{E}{1-\nu}\right)\frac{1}{a^2} \tag{5.2}$$

$$Intercept = C_1 \sigma_o \tag{5.3}$$

where the constants C_1 and $C_2 f(\nu)$ were obtained from Eq. 4. 11 for square films (PI) and from Eq. 4.5 for circular films (coatings). Therefore, biaxial modulus and residual stress were calculated from slopes and intercepts, respectively. Table 5.3 shows the average and the deviation of results for PI and coatings. The residual strain, ε, was calculated by dividing residual stress by biaxial modulus. The information about residual strain indicates how much the film has been stretched after it is cured. The average results of six PI samples were 5.38 GPa for biaxial modulus and 33.4 MPa for residual stress. These results were in good agreement with previous reports [72, 10].

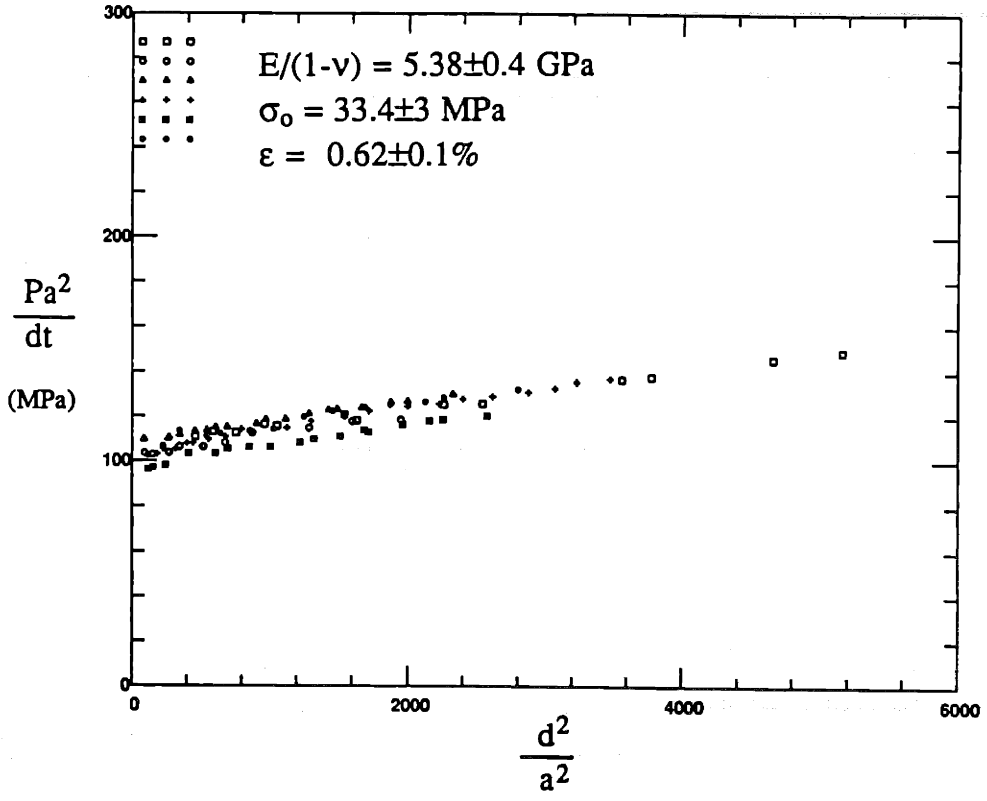

Figure 5.1 The pressure-deflection data for PI using blister test.

Samples	PI	Once-cured			Twice-cured		
		APC	APC-D	PEU	APC	APC-D	PEU
$E/(1-\nu)$, GPa	5.38±0.4	2.2±0.2	1.85±0.19	0.06±0.01	2.5±0.2	2.1±0.2	0.116±0.02
σ_o, MPa	33.4±3	1.4±0.15	1.3±0.15	0.88±0.17	1.8±0.15	1.6±0.15	1.1±0.1
ε, %	0.62±0.1	0.06±0.02	0.07±0.02	1.5±0.5	0.07±0.01	0.08±0.08	0.95±0.2

Table 5.3 The biaxial modulus and residual stress of polyimide, once-cured coatings, and twice-cured coatings. The measurements of twice-cured coatings are described in Section 5.2.5.

5.2.3 Errors in Load-Deflection Measurements

The purpose of this section is to analyze the reproducibility of the blister method. First, a repeated test was made on the same sample. A typical reproduced measurement is shown in Fig. 5.2 and the difference between these two measurements was within 3%. This indicates that the repeated measurements on the same sample were in good agreement. Another way of testing reproducibility is to perform measurements on the same sample by different people. In this case, a PI square sample was used. The standard deviation among the four people's measurements was 4.3% for residual stress and 3.6% for biaxial modulus [73]. This indicates the measuring technique was consistent.

To understand the reproducibility in sample fabrication, five different PI samples fabricated by different people were tested by one person. The standard deviation was 2.5% for residual stress measurement and was 2.6% for biaxial modulus measurement [73]. This implies that the sample fabrication technique for PI was also very consistent.

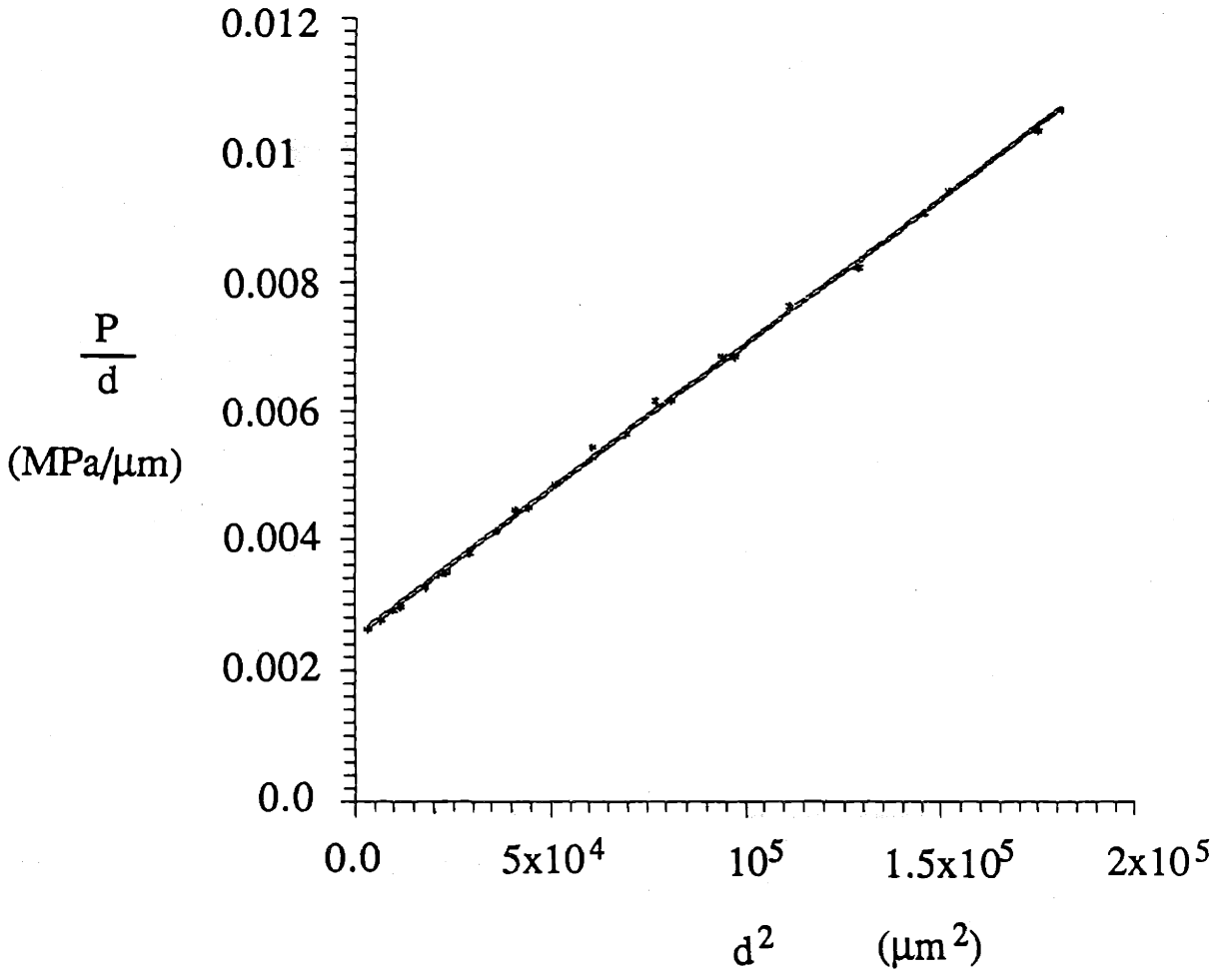

Figure 5.2 The typical reproduced load-deflection measurements on same samples.

There were other variations in the load-deflection tests such as using different pressure calibration curves, and the elimination of small pressure readings in data analysis. The standard deviation among these variations was 2.6% for residual stress and was 2.8% for biaxial modulus.

Measurements of film size and thickness were also needed for evaluating mechanical properties of films. The film size was measured using an x- and y-direction micrometer built on the microscope stage. The resolution of the micrometer is 1 μm and the edges of film are reasonably sharp (the variation was less than ±50 μm). Therefore, the error in size measurement was usually less than 0.8%. For film thickness, PI films were very uniform (less than 3% variation), while the coatings fabricated from spraying were not as uniform. Thickness variation of coatings was about ±10%, even though the measuring techniques had a good resolution. More discussion about the thickness variation is presented in Section 5.4.1.

It is concluded that the measurement technique for the blister test is very consistent. The variations in mechanical measurements due to personal error (e.g., to focus the film through a microscope) is less than 4% usually. Hence, in the case of sprayed coatings, the error due to the variation in thickness is probably the major error in this mechanical measurement.

5.2.4 Solvent Effect on Mechanical Properties of Polyimide

The purpose of this section is to analyze whether solvents and the thermal curing of coatings during the spray coating process affect the mechanical properties of PI. Square single-layer PI samples were fabricated for the blister test. Two PIs were used: BTDA-MPDA(20%)/ODA(80%) and BTDA-MPDA(40%)/ODA(60%). Five different solvents were chosen for this study: xylene, heptane, methanol, butanol, and water. PI was soaked in these solvents and then was dried at 250°F for 30 minutes to mimic the spray coating process. Details of experimental procedures are described in Section 2.3.3.

The results are shown in Table 5.4. For BTDA-MPDA(20%)/ODA(80%), the values of the biaxial modulus slightly dropped 7-8% when PI films were treated with heptane or methanol, while xylene and water did not affect the biaxial modulus significantly (less than 3%). The residual stress of BTDA-MPDA(20%)/ODA(80%) decreased 10-14% when the films were soaked with xylene, methanol, or water, while the residual stress of the heptane-treated PI was not affected.

For BTDA-MPDA(40%)/ODA(60%), the values of the biaxial modulus did not change significantly (less than 5% on average). The changes in residual stress were also within 5% except for the one treated with water (8.6%).

An unusual phenomenon was observed when PI samples were soaked in solvents. Both types of PI films were strongly affected by methanol. The suspended tensile films started to lose their tensile residue stress after they were immersed in methanol. The films became wrinkled, suggesting either the development of compressive stress (buckling) or, that the methanol had caused lateral swelling. After the films were dried, the wrinkles disappeared and the films returned to a tensile stress state. In addition, the residual stress still remained at a very high value.

In conclusion, the changes in the biaxial modulus of PI caused by the solvent treatment were usually less than 5%, with an exception at about 8%. The change in the residual stress was generally larger and the maximum decrease was about 14%. This indicates that the treatment of solvents affects residual stress more than the biaxial modulus. This is reasonable since the PI is under a tensile residual stress, and the driving force for absorbing solvent molecules is thermodynamically favorable. The decrease in the residual stress is possibly due to the increase in the residual solvent content in PI films. This possibility has not been systematically investigated.

	Materials	E/(1-v) (GPa)	ΔE/E	S (MPa)	ΔS/S
PI-2555	pure PI	6.27+0.2		36.8±0.3	
	xylene treated PI	6.42±0.2	+2.3%	33.3+0.2	-9.5%
	heptane treated PI	5.85±0.1	-6.7%	36.2±0.2	-0.2%
	methanol treated PI	5.7±0.05	-8.3%	31.7±0.3	-13.8%
	water treated PI	6.0±0.15	-3%	32+0.15	-13%
PI-2525	pure PI	5.80±0.05		32.5±0.3	
	xylene treated PI	5.8±0.05	+0.5%	31.9±0.1	-1.8%
	heptane treated PI	6.0+0.1	+4.5%	32.1±0.7	-1.2%
	methanol treated PI	5.8±0.15	+1.3%	34±0.15	+4.6%
	water treated PI	6.11±0.15	+5.4%	35.3±0.15	+8.6%
	butanol treated PI	5.7±0.05	-1.1%	33.9±0.3	+4.3%

Table 5.4 The biaxial modulus and residual stress of polyimides subjected to solvent treatment. PI-2555 is BTDA-MPDA(20%)/ODA(80%) and PI-2525 is BTDA-MPDA(40%)/ODA(60%).

The change in mechanical properties of PI will be reflected as a calculation error in evaluating the mechanical properties of multi-layer coatings in Section 5.3. Further discussion of the calculation error is given in Section 5.4.3.

5.2.5 Process Effect on Mechanical Properties of Coatings

In the processing of multi-layer films, the first layer was coated first and cured in the oven; then the second layer was coated and cured. That is, a new coating is always deposited onto an already-cured coating. This is the so-called wet-on-dry coating process. In this case, the first layer was actually cured twice in a process of fabricating bi-layer films. Therefore, it is essential to understand whether or not the mechanical properties of the first layer were changed after the second curing.

Three different coatings were used in this study: APC, APC-D, and PEU. These films were fabricated with normal procedures except that they were cured twice, for a total of 60 minutes. Circular single-layer samples were made for the blister test. The mechanical measurements of these twice-cured coatings are shown in Table 5.3. It was found that both the biaxial modulus and the residual stress of coatings were increased in the long curing process. The values of the biaxial modulus were increased by 15%-18% for APC and APC-D, and were increased by about 93% for PEU. The values of residual stress for all three coatings were increased by 26%-29%. The increase in the biaxial modulus is possibly due to the higher degree of crosslinking after a longer cure [74]. As mentioned in the previous section, the residual solvent content may affect the value of residual stress. The increase in residual stress may be due to the decrease in residual solvent content in the long curing process.

The mechanical properties of coatings obtained from single-layer samples were used for calculating the mechanical properties of multi-layer films. Hence, the properties of twice-cured coatings should be used instead of those of once-cured coatings (see Table 5.3), since the first layer of coating was really cured twice during sample fabrication. As seen in Table 5.4, the change in mechanical properties by this prolonged cure process for PI (BTDA-MPDA(40%)/ODA(60%)) was much less than for coatings. Thus, the mechanical properties of PI shown in Table 5.3 were still usable for calculating mechanical properties of multi-layer films. The calculation for multi-layer films is given in the next section.

5.3 Mechanical Properties of Multi-layer Films Using Blister Method

5.3.1 Types of Samples

All multi-layer samples in this study are listed in Table 5.5. For square samples, eight types of films were fabricated. PI was always used as a bottom layer and three coatings were deposited on top of it. There were three types of two-layer films: PI+APC, PI+APC-D, and PI+PEU. There were three types of three-layer films: PI+APC+APC-D, PI+PEU+APC, and PI+APC-D+PEU, and two types of four-layer samples: PI+APC+APC-D+PEU and PI+PEU+APC+APC-D.

For circular samples, there were three types of two-layer films: APC-D+APC, APC+PEU, and PEU+APC-D; and two types of three-layer films: PEU+APC-D+APC, and APC-D+APC+PEU.

Shape	2 layers	3 layers	4 layers
Square	PI+APC PI+APC-D PI+PEU	PI+APC+APC-D PI+APC-D+PEU PI+PEU+APC	PI+APC+APC-D+PEU PI+PEU+APC+APC-D
Circular	APC-D+APC PEU+APC-D APC+PEU	APC-D+APC+PEU PEU+APC-D+APC	

Table 5.5 The types of square samples for mechanical property measurements. PI is polyimide; APC is acrylic polymer coating; APC-D is acrylic polymer coating with dispersed resins; PEU is polyester urethane. PI+APC+APC-D means that PI is the bottom layer, APC is in the middle, and APC-D is the top layer.

5.3.2 Mechanical Measurements for Multi-layer Coatings

The typical results of multi-layer coatings are shown in Fig. 5.3. The equation used to solve the multi-layer structure was from Eq. 4.16:

$$\frac{Pa^2}{d} = \left(\frac{d^2}{a^2}\right)\sum_{i=1}^{n}\left(\frac{C_{2i}f(\nu_i)E_i t_i}{1-\nu_i}\right) + \left(\frac{1}{a^2}\right)\sum_{i=1}^{n}\left(\frac{C_{4i}E_i t_i^3}{1-\nu_i}\right) + C_1\sum_{i=1}^{n}\sigma_{oi}t_i \qquad (5.4)$$

where the constants C_1, $C_2f(\nu)$ and C_4 were obtained from Table 4.9 for square films and from Table 4.5 for circular films. The subscript i stands for the i-th layer. For example, for a PI+APC sample, the value of i is 1 for PI and is 2 for APC. From Eq. 5.4, the slope and intercept of the plot of Pa^2/d versus d^2 can be expressed as:

$$Slope = \left(\frac{1}{a^2}\right)\sum_{i=1}^{n}\left(\frac{C_{2i}f(\nu_i)E_i t_i}{1-\nu_i}\right) \qquad (5.5)$$

$$Intercept = \left(\frac{1}{a^2}\right)\sum_{i=1}^{n}\left(\frac{C_{4i}E_i t_i^3}{1-\nu_i}\right) + C_1\sum_{i=1}^{n}\sigma_{oi}t_i \quad . \tag{5.6}$$

To calculate the Poisson ratio-dependent constants, the Poisson ratio of PI was assumed to be 0.4 and the Poisson ratios for APC, APC-D, and PEU were assumed to be 0.42, 0.34, and 0.3, respectively. These assumptions are the same as in Section 5.2.2.

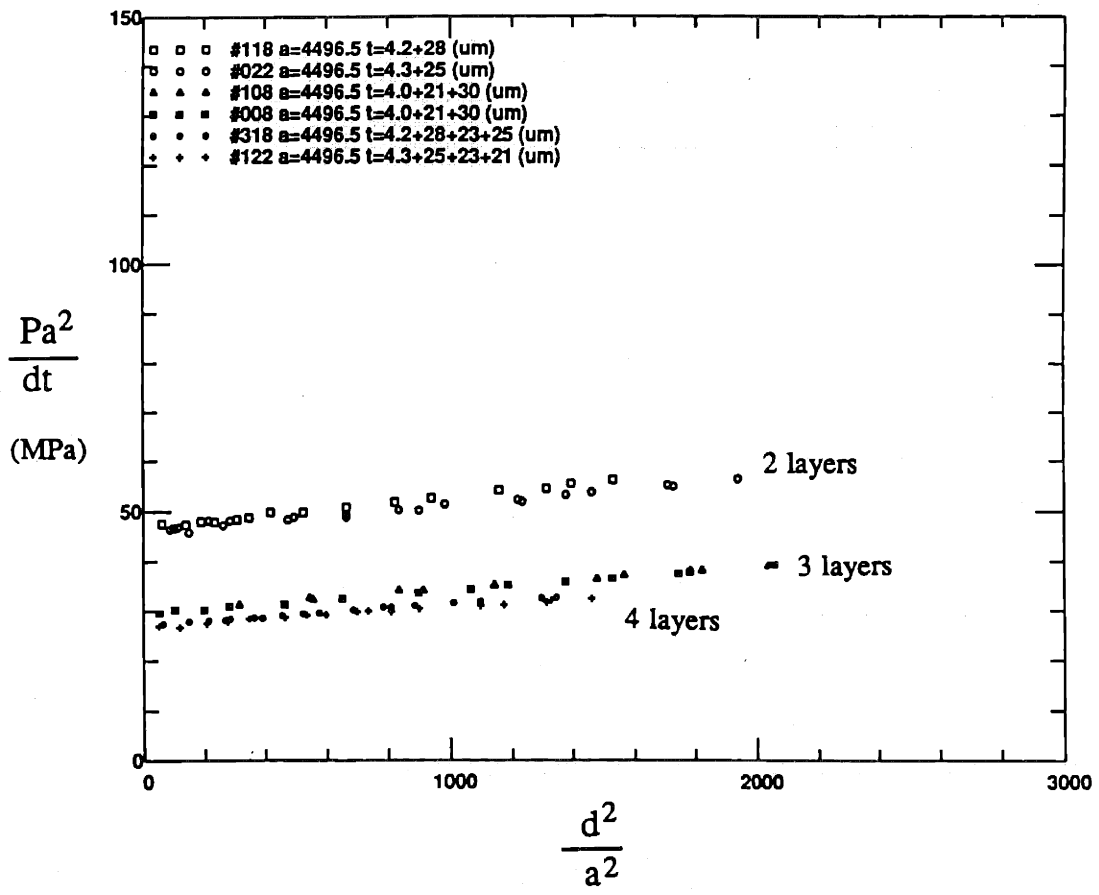

Figure 5.3 The pressure-deflection data for PI+APC (two-layer), PI+APC+APC-D (three-layer), and PI+APC+APC-D+PEU (four-layer) from the blister test.

The slope and intercept of each data line in Fig. 5.3 were calculated using least-square fitting. Substituting the biaxial modulus and residual stress of the first layer (Table 5.3 for PI and twice-cured coatings) into Eqs. 5.5 and 5.6 (setting n equal to 2), the biaxial modulus and residual stress of the second layer were calculated. Similarly, using the data of three-layer films and including the previously-measured mechanical properties of the first and second layers into Eqs. 5.5 and 5.6 (now n equals 3), the biaxial modulus and residual stress of the third layer were obtained. The calculation procedure was the same for four-layer films.

The summary of the results for all square films is shown in Table 5.6. Table 5.7 shows the results of circular films. The residual strain, ε, was calculated by dividing residual stress by biaxial modulus. The results are discussed in the following section.

	2 layers			3 layers			4 layers	
Sample	APC PI	APC-D PI	PEU PI	APC PEU PI	APC-D APC PI	PEU APC-D PI	APC-D APC PEU PI	PEU APC-D APC PI
Top layer	APC	APC-D	PEU	APC	APC-D	PEU	APC-D	PEU
$E/(1-\nu)$, GPa	2.3±0.3	2.1±0.3	0.09±0.2	3.1±1	2.4±1	0.59±0.3	2.3±1	0.69±0.4
σ_o, MPa	11±2	5.7±1	2.3±0.4	8.7±1.8	5.1±1.5	2.8±0.6	4.7±1.4	4.4±1.4
ε, %	0.48±0.15	0.27±0.1	2.6±1	0.28±0.14	0.21±0.12	0.29±0.15	0.2±0.1	0.64±0.5

Table 5.6 The results of the biaxial modulus, the residual stress, and the residual strain for multi-layer films (square samples).

	2 layers			3 layers	
Sample	APC APC-D	APC-D PEU	PEU APC	PEU APC APC-D	APC APC-D PEU
Top layer	APC	APC-D	PEU	PEU	APC
$E/(1-\nu)$, GPa	2.1±0.3	1.9±0.5	0.064±0.02	0.01±0.008	2.6±1
σ_o, MPa	1.5±0.4	2.0±0.5	1.7±0.5	0.71±0.5	1.2±0.4
ε, %	0.07±0.03	0.1±0.05	2.6±1	5.9±4.5	0.05±0.02

Table 5.7 The results of the biaxial modulus, the residual stress, and the residual strain for multi-layer films (circular samples).

5.3.3 Discussion of Mechanical Properties of Multi-layer Coatings

Comparing Table 5.3 (for single-layers) with Tables 5.6 and 5.7 (for multi-layers), the results of two-layer films were in good agreement (within 5%) with the results of single-layer films. This indicates Eq. 5.1 and Eq. 5.4 are quite consistent with each other. The deviation of the experimental results for the second layer was about 15%. The error for the low modulus materials is even higher (e.g. PEU, about 22% for the biaxial modulus). This is partly due to the large error in the subtraction of a high modulus layer from the bi-layer (Eqs. 5.5 and 5.6).

Comparing the biaxial moduli of two-layer films in Tables 5.6 and 5.7, the results of circular films (Table 5.7) were in reasonable agreement with those of square films (Table

5.6) except for the PEU. As mentioned above, this is due to the large error in evaluating the mechanical properties of low modulus materials on top of a high modulus material. As also noted in this comparison, the biaxial moduli of coatings (Table 5.7) were generally smaller than those in Table 5.6. This is partly due to the difference between the thickness measurement techniques. The micrometer (for measuring circular films) usually gave higher values than the surface profilometer (for square films) because of the surface roughness of coatings. Therefore, the values of biaxial modulus for circular films were a bit lower.

Comparing the residual stress of two-layer films in Tables 5.6 and 5.7, the residual stress of coatings cured on the release layer (Tedlar®) is much lower than for those cured on PI, where the adhesion is good. This shows why curing films on release layers may not give the same results as curing on the final end-use substrate; hence the importance of *in situ* methods.

Tables 5.6 and 5.7 also show that three-layer films and four-layer films have a large deviation in the results of biaxial modulus and residual stress and hence, the results were only in fair agreement with those of first-layer and second-layer films. As mentioned in Section 5.2.3, the variation in thickness of spray-coated films was probably the major error source in this mechanical measurement. More discussion of load-deflection measurements is given in the next section.

5.4 Discussion of Load-Deflection Measurements

5.4.1 The Variation of Thickness Data

The causes of the variation in thickness can be divided into two sources: the uniformity of thickness and the surface roughness. The uniformity of films was tested by

measuring the thickness of films on different locations across a 2-inch wafer. The coatings were sprayed onto blank silicon wafers and the thicknesses of coatings at different locations were measured using a surface profilometer. The results showed that the thickness variations across a one-inch distance of APC, APC-D, and PEU were approximately ±4.5%, ±3.7%, and ±7.4%, respectively.

The surface roughness of spray-deposited coatings was not a problem at all. The surfaces were scanned using a surface profilometer, which showed the roughness of APC and APC-D was within ±0.4μm. The roughness of PEU was slightly higher (±1μm). These data indicate that the roughness was not a problem since it only caused a variation of approximately ±1.3%-3.3%, assuming the thickness was 30μm. However, the coatings released from the Tedlar® films have duplicated the surface roughness of the Tedlar® films. The surface roughness of the Tedlar® films was measured to be ±1.2μm, or 4%. Thus, the thickness measured by the micrometer for circular samples (released from Tedlar® films) tended to be slightly larger. This is probably why the values of the biaxial modulus for circular films were slightly smaller than those for square films.

In conclusion, the thickness variation due to the spraying process was approximately ±3.7%-7.4%. The surface roughness of coatings was ±1.3%-3.3%, while the roughness introduced by Tedlar® films was ±4%. Hence, the thickness variation was approximately ±5%-10.7% for square samples and was approximately ±9%-14.7% for circular samples. The additional variation of circular films was caused by the Tedlar® films.

5.4.2 Sensitivity of Mechanical Measurements on Thickness Data

The purpose of the sensitivity analysis is to understand how sensitive the mechanical results are to the variations in thickness. Seven square samples (Table 5.8) were chosen for this analysis.

Sample	2 layers			3 layers			4 layers	
	APC PI	APC-D PI	PEU PI	APC PEU PI	APC-D APC PI	PEU APC-D PI	APC-D APC PEU PI	PEU APC-D APC PI
Top layer	APC	APC-D	PEU	APC	APC-D	PEU	APC-D	PEU
$\Delta E/E_{avg}$, %	±1.1	±2.2	±46	±6.8	±2.4	-	±37.4	±19
$\Delta\sigma_o/\sigma_{oavg}$ %	±1.8	±10.3	±21.4	±4.5	±10.3	±45	±36.3	±17

Table 5.8 Thickness sensitivity analysis on the evaluation of mechanical properties for multi-layer films.

The procedures for calculating the biaxial modulus and the residual stress were exactly the same as those in the previous section. The procedures began with the PI+coating two-layer samples. The thickness and mechanical data evaluated for PI were assumed to be correct. Also, the thickness data for each coating layer were assumed to be mismeasured with ±10% margin of error. These "wrong" thickness data certainly gave "wrong" answers in the calculation of the biaxial modulus and the residual stress of coatings that were on top of the PI. Then the maximum and minimum biaxial moduli and the residual stresses of the coatings analyzed from the "wrong" thickness data were

recorded and were also used to evaluate the mechanical properties of PI+coating+coating three-layer coatings. The procedures were repeated until all mechanical properties of four layers were solved.

The results were calculated as the half difference between the maximum and the minimum divided by the average value (Table 5.8). Two points are worth mentioning here. First, the ±10% variation in thickness did not cause a great difference in the results of APC and APC-D in the two-layer films. However, large variations were found for PEU in the two-layer films, due to the low biaxial modulus and residual stress of PEU. For example, for APC and APC-D, the variation in biaxial modulus was up to ±1.1%-2.2% (PI+APC and PI+APC-D), while the variation of PEU was as high as ±46% (PI+PEU). Second, the mechanical results of the upper layer generally had a greater variation than the results of the lower layers, except for the case when PEU was under APC and APC-D. This is reasonable because the generated errors of each layer were transferred to and accumulated in the next calculation. It is found that the variations of the results are within 6% for two-layer films (except for PEU); the variations are less than 10% for three-layer films, and are above 17% for four-layer samples. This indicates that highly uniform films and accuracy in the thickness measurements are needed in order to evaluate the mechanical properties of four-layer coatings within a reasonable error range.

5.4.3 Sensitivity of the Measurement on Mechanical Property Data

In the previous section, the effect on the mechanical properties of coatings were shown when thickness of coatings was varied within a margin of ±10% error. In this section, the purpose of this analysis was to calculate sensitivity of the mechanical properties of coatings from the load-deflection data of PI+coating films. In other words, it investigated how much margin of error was generated when mechanical properties of PI

were measured improperly. The assumed variation of the mechanical properties (biaxial modulus and residual stress) of PI was ±10%. The maximum and minimum biaxial modulus and residual stress of the coatings were calculated by the same procedures presented in the previous section using 10% variation in the PI properties. Again, for multi-layer films, these maximum and minimum properties of lower layer coatings were used to calculate the properties of upper layers. Thus, the margin of errors of ±10% was transferred and propagated in the mechanical evaluation to see what the "worst cases" would be.

	2 layers			3 layers			4 layers	
Sample	APC PI	APC-D PI	PEU PI	APC PEU PI	APC-D APC PI	PEU APC-D PI	APC-D APC PEU PI	PEU APC-D APC PI
Top layer	APC	APC-D	PEU	APC	APC-D	PEU	APC-D	PEU
$\Delta E/E_{avg}$, %	±2.8	±3.7	±41	±5.1	±5.1	±53	±18	±30
$\Delta\sigma_o/\sigma_{oavg}$ %	±4.2	±8.5	±24	±14	±16	±39	±26	±33

Table 5.9 Mechanical property sensitivity analysis on the evaluation of mechanical properties for multi-layer films.

The results are shown in Table 5.9. For a high-modulus material (e.g., APC and APC-D), the deviation was only 3-5% in the biaxial modulus and 4-16% in the residual stress. For a low-modulus material (PEU), the deviations were quite dramatic – about 41-53% change in the biaxial modulus and 24-39% change in the residual stress. The margin of error was found to increase for a multi-layer structure. As expected, the results for the

four-layer structures had the highest margin of error since the margin of errors of the three bottom layers were accumulated in the mechanical evaluation of the fourth layer. For example, as seen in Table 5.9, the variation in APC-D in a four-layer membrane (18% in biaxial modulus and 26% in residual stress) is much higher than in a two- or three-layer membrane (4-5% for biaxial modulus and 8-16% for residual stress).

Compared to Section 5.4.2, it was found that for residual stress, the ±10% in the mechanical properties of PI has more influence than the ±10% in thickness variation. Both variations affected the values of the biaxial modulus in a similar way. Hence, this analysis indicates that if the "worst case" happened, the variation for low-modulus materials and the variation for films more than three layers are too large to be acceptable.

5.4.4 Strain Rate Effect on Mechanical Properties of Coatings

In the load-deflection experiments, the relationship of pressure and deflection was recorded. The change of the rate of increasing pressure is similar to the change of the strain rate in the uniaxial tensile test. Thus, the "strain rate" discussed in this section is the pressure rate. The load-deflection experiments were performed in a quasi-steady state. That is, the pressure was increased at a very slow rate. In the experimental set-up, the pressure was controlled by gradually opening a needle valve.

Usually, the rate of increasing pressure was estimated by dividing the final strain with the time needed for pumping the film. The final strain was on the order of 0.5%. In each experiment, 10-20 pressure-deflection readings were recorded. The time needed to increase the pressure for each datum is about 1-3 seconds. Therefore, total time needed to have a 0.5% strain was approximately 50 seconds. Then the estimated strain rate of load-

deflection experiments was about 0.6% per minute. The corresponding pressure rate was about 0.03 psi/sec, which was reasonably small.

In this study, the strain rate was reduced even more. The time needed to increase the pressure for each reading was decreased to about 80 seconds. Thus, total time needed for the entire experiment was about 1200 seconds. The strain rate was, therefore, about 0.02% per minute and the corresponding pressure rate was about 0.001 psi/sec. The effect of the decreased strain rate is shown in Table 5.10.

Samples	APC	APC-D	PEU
$E/(1-\nu)$, GPa	1.94	1.60	0.045
σ_o, MPa	1.43	1.27	0.88
ε, %	0.074	0.079	2.0

Table 5.10 The strain rate effect on the biaxial modulus and the residual stress of coatings.

As expected, the biaxial modulus and the residual stress of coatings decreased with the strain rate. This is in good agreement with the literature [75]. However, some of the changes in mechanical properties were less than 10%, which is very small and is within the normal range of the experimental error. It was also found that PI was minimally affected by the change of the strain rate.

5.5 Uniaxial Tensile Test

Uniaxial tensile tests are one of the most straightforward methods to obtain the stress-strain relationship of materials. The purpose of this test is to obtain Young's modulus of films which can be calculated from the initial slope of the stress-strain curve.

The Young's modulus obtained from this test was then compared with biaxial modulus from load-deflection tests to calculate in-plane Poisson ratio of films (Section 5.5.5).

5.5.1 Types of Samples

The materials used for this study were PI, APC, APC-D, and PEU. Table 5.11 shows that seven types of samples were subjected to uniaxial tensile tests: four single-layer films and three bi-layer films. Among these samples, two of them were fabricated using microfabrication techniques and these samples contained PI (BTDA-MPDA(40%)/ODA(60%)). The other five types of samples were made using the coat-and-peel method and contained no PI. The details of sample fabrication are described in Sections 2.7.1 and 2.7.2.

1 layer	2 layers
PI	PI+APC
APC	APC+PEU
APC-D	APC-D+PEU
PEU	

Table 5.11 The samples for the uniaxial tensile test.

5.5.2 Young's Modulus for Single-Layer Films

To compare these results with the load-deflection measurement which was tested under a quasi-steady state, the strain rate of this test was kept as low as possible. Since the strain rate was very low, it took a little time for the Instron machine to apply the load to the sample, which caused nonlinearity in the very beginning of the stress-strain plots.

Therefore, the maximum slope in the beginning of the stress-strain curve was calculated to be the Young's modulus of the film. A typical stress-strain curve is shown in Fig. 5.4. The results for single-layer films are shown in Table 5.12.

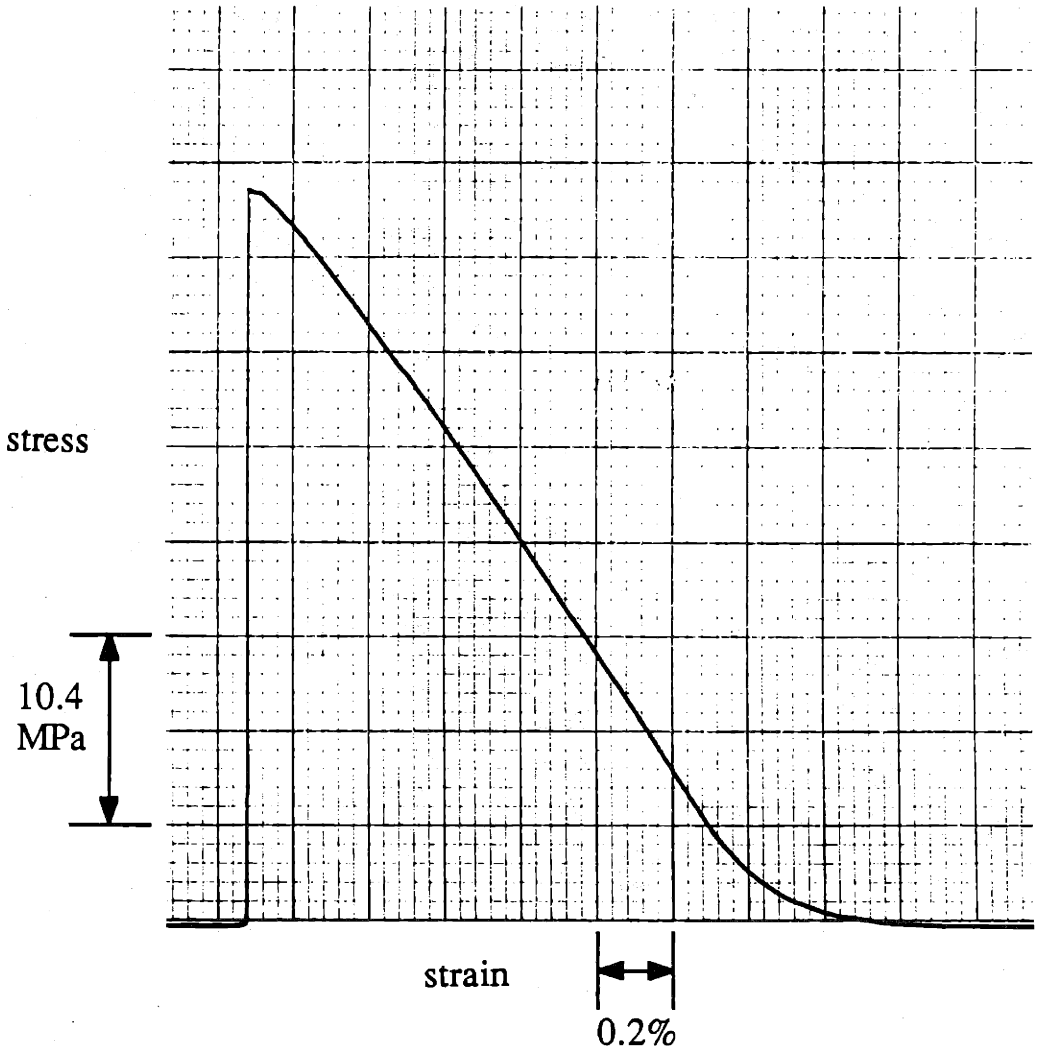

Figure 5.4 The stress-strain curve of PI in the uniaxial tensile test.

One of the assumption in the load-deflection experiment was the linear elasticity of materials. The stress-strain results of PI, APC and APC-D indicated that this was a reasonable assumption, since the residual strain plus the strain from the load-deflection test did not exceed the linear elasticity regime. Therefore, the results from both load-deflection and tensile tests were comparable.

Sample	Number of Samples	Young's Modulus, GPa	Average, GPa
PI	7	3.4, 3.2, 3.0, 3.4, 3.2, 2.9, 3.3	3.2±0.3
APC	2	1.20, 1.21	1.20±0.01
APC-D	4	1.21, 1.24, 1.17, 1.18	1.20±0.04
PEU	3	0.052, 0.051, 0.048	0.05±0.002

Table 5.12 The Young's modulus of PI and coatings from the uniaxial tensile tests.

The case of PEU was slightly different. That is, the modulus actually measured from load-deflection tests was smaller than the modulus calculated from the maximum slope of the stress-strain curve (Fig. 5.5). Thus, in order to calculate the Poisson ratio of PEU, the Young's modulus had to be measured from the slope after the residual stress mark since that was the beginning point of the load-deflection test. This new value of Young's modulus (called the "effective" Young's modulus) was calculated to be 0.041GPa for PEU.

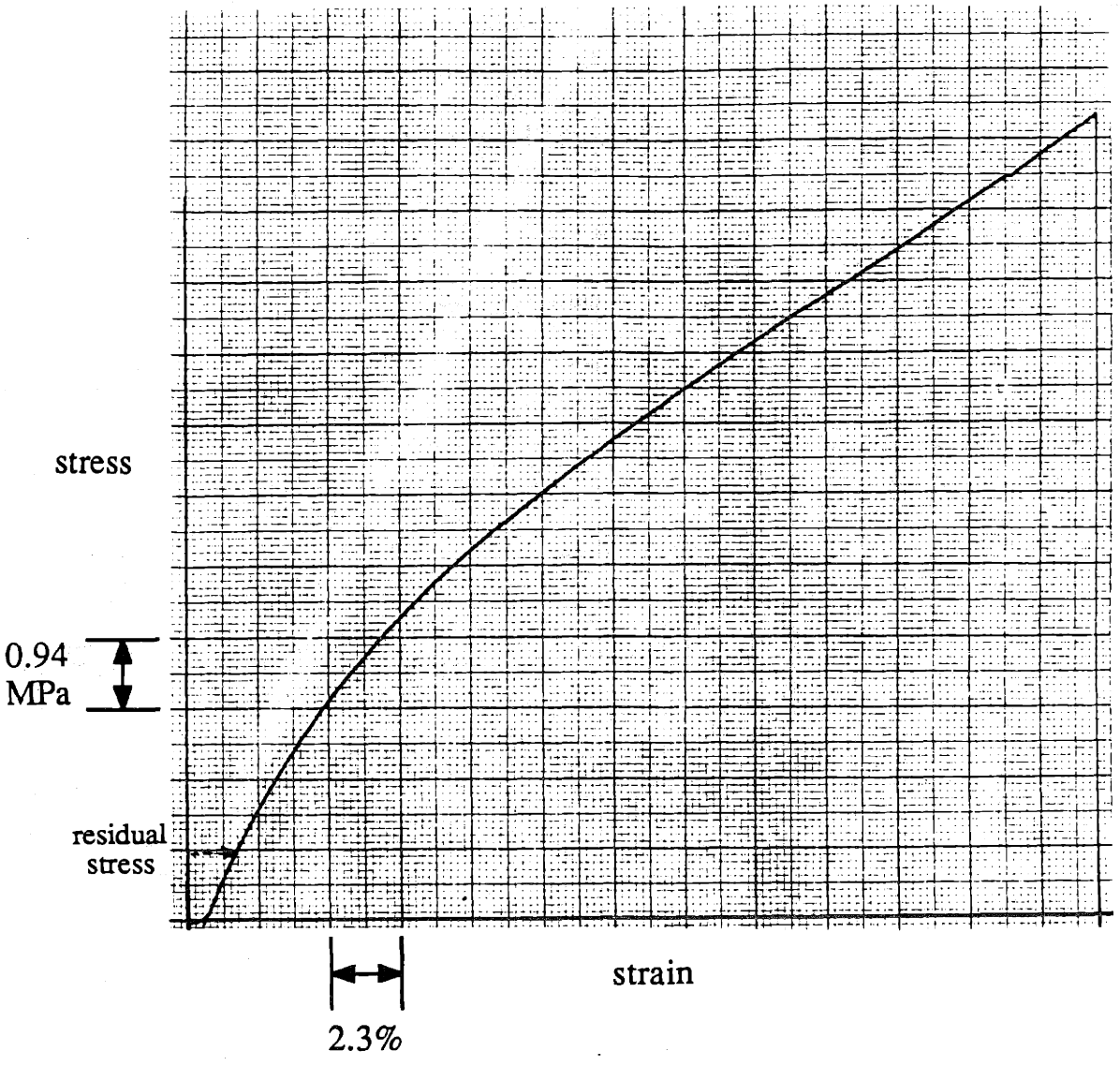

Figure 5.5 The stress-strain curve of PEU in the uniaxial tensile test. The residual stress (about 0.9MPa) was also marked in the curve.

5.5.3 Young's Modulus for Twice-Cured Coatings

Table 5.13 shows the Young's modulus for twice-cured coatings. These coatings were fabricated in the same way as those in Table 5.12 except for two curings. It was

found that the Young's moduli of the twice-cured coatings were higher than the once-cured coatings. The increase in the Young's moduli was about 16%-19% for APC and APC-D, and was about 122% for PEU. The increase for PEU was more than two-fold, indicating that PEU is very sensitive to the curing process at elevated temperatures. Similar results were also found from the load-deflection tests and were discussed in Section 5.2.5.

Sample	Number of Samples	Young's Modulus, GPa	Average, GPa
APC	2	1.36, 1.51	1.44±0.08
APC-D	2	1.46, 1.32,	1.39±0.07
PEU	3	0.117, 0.106, 0.117	0.113±0.007

Table 5.13 The Young's modulus for twice-cured coatings.

5.5.4 Young's Modulus for Two-Layer Films

The average Young's modulus for three different two-layer films was measured. The purpose of this test is to establish a bench mark for the mechanical properties of multi-layer films measured by load-deflection tests. Assuming the strain on each layer is the same during the tensile test, a first order approximation can be obtained:

$$E_{avg}\, t_{tot} = \sum_{i=1}^{2} E_i t_i \qquad (5.7)$$

where E_{avg} is the average Young's modulus, t_{tot} the total thickness, the E_i the individual Young's modulus, and t_i the individual thickness. Since the Young's modulus of the first

layer was already obtained (Table 5.12), the Young's modulus of the second layer can be calculated using Eq. 5.7.

The results calculated from Eq. 5.9 are shown in Table 5.14. Compared to Table 5.12, the results were in good agreement except for APC-D, for which only one sample was available. It is concluded that the results of multi-layer films using the uniaxial tensile test are a reasonable reference for the mechanical properties evaluated by the blister test.

Sample	Top Layer	Young's Modulus, GPa	Average, GPa
PI+APC	APC	1.52, 1.40, 1.63 1.25, 1.40	1.44±0.19
PEU+APC-D	APC-D	0.73,	0.73
APC+PEU	PEU	0.032, 0.074	0.053±0.021

Table 5.14 The Young's modulus of the top layer in the two-layer coatings.

5.5.5 Calculation of In-Plane Poisson Ratio

The results from uniaxial tensile tests give information about Young's modulus, while the results from the load-deflection experiments give the values of the biaxial modulus. Thus, by dividing the values in Table 5.3 by the values in Table 5.12, the in-plane Poisson ratios can be obtained. For twice-cured coatings, the in-plane Poisson ratios were also calculated from Tables 5.3 and 5.13. The values of in-plane Poisson ratios are listed in Table 5.15.

Samples	Once-cured			Twice-cured		
	APC	APC-D	PEU	APC	APC-D	PEU
E, GPa	1.20	1.22	0.041†	1.44	1.39	0.082†
E/(1-ν), GPa	2.12	1.83	0.06	2.5	2.1	0.116
ν	0.43	0.33	0.32	0.42	0.34	0.29

† E was calculated at the residual strain.

Table 5.15 The in-plane Poisson ratio for both once-cured and twice-cured coatings.

It is noted that the Poisson ratio of once-cured and twice-cured coatings were in good agreement. This indicates that both measurements of biaxial modulus and Young's modulus were very reasonable. In general, the margin of error of the Poisson ratio measurements is about 20%, since both the results of the load-deflection test and the uniaxial tensile test are in ±10% margin of error.

CHAPTER 6

Humidity Effect on Mechanical Properties

6.1 Introduction

The effect of environmental changes (e.g. humidity) on mechanical properties is very important to the performance of coatings. In this chapter, the effects of humidity on both the biaxial modulus and the residual stress of single-layer coatings were analyzed using the blister method. The purpose of this study was to determine quantitatively the change of mechanical properties due to the humidity effect. The focus of this work was to verify the capability of this technique (the blister test) rather than to study the mechanism of moisture absorption for coatings.

The fundamentals of the humidity effect on coatings are introduced in Section 6.2. In Section 6.3, the types of samples used in this study are described. Two different types of measurements are presented in Section 6.4: the change in mechanical properties as a function of time and the change in the mechanical properties with respect to the relative humidity (RH).

6.2 Background of Humidity Effect on Coatings

Humidity change is very critical to the performance of polymeric coatings. For coatings used as paints, good weatherability and durability are essential. The most recent studies about the humidity effect on coatings are related to outdoor exposure of coatings [76]. When paints are used for outdoor purposes, moisture is one of the major factors

causing the degradation of paint films. Other influences such as solar radiation, temperature changes, and oxidation may also cause a change in the mechanical properties of the coatings [2]. The so-called accelerated test methods were primarily used to examine the mechanical failure of coatings under severe environmental conditions. Hence, most investigations of these techniques were related to the degradation of coatings with respect to chalking, scaling, gloss, hardness and so on.

Water absorption usually occurs when polymeric films are exposed to a humid environment [77]. Moisture uptake can be measured using a gravimetric method which measures the mass change of films after absorbing moisture. Other changes in physical properties as a function of time (such as dieletric properties) can be used to measure the diffusion constant of water molecules [78,79]. Also, the bending beam method for measuring the residual stress of coatings (Section 1.2.2) has been used to monitor the moisture effect on the residual stress [80]. Hence, the swelling factor which is correlated to the moisture uptake and the hygroscopic strain can be calculated, provided that the moisture content is known.

The mechanical properties of many polymers have been reported to be influenced by the moisture content. For example, water molecules have been known to have a plasticization effect to nylon [81]. In such a case, water molecules break the intermolecular hydrogen bonding and decrease the modulus dramatically. Epoxy resins were also reported to have a problem of adhesion failure due to water molecules modifying interfacial bondings [82].

6.3 Types of Samples

Three different coatings were studied using the blister method: APC, APC-D, and PEU. Circular single-layer samples were fabricated from these materials; details of sample fabrication are shown in Section 2.4. The evaluation of the mechanical properties were similar to the procedures shown in Chapter 5.

6.4 Mechanical Properties Measurements

The test samples were isolated in a sample chamber in which the relative humidity was controlled by a humid air stream. A dry environment was achieved using a house compressed air source (the dew point was lower than -46°C). Before each blister test, the sample was seated in the sample chamber to reach the equilibrium state. The details of measurement procedures are described in Sections 2.6.2 and 5.2.2.

6.4.1 Mechanical Properties Versus Time

The purpose of this measurement was to find the time needed for the coatings to reach an equilibrium condition in a humid environment. First, the sample chamber was purged with dry air for about 2 hours. Then the relative humidity (RH) of the sample chamber was changed to 60%. All experiments were conducted at room temperature. The load-deflection behavior of coatings as a function of time was measured and the starting time for each blister test was recorded. Because each experiment took 5-10 minutes, the results were not real-time measurements. Nevertheless, the mechanical properties as a function of time still reveal information about the approximate time needed for the moisture absorption to reach a equilibrium state.

The biaxial modulus and the residual stress of coatings versus time are shown in Fig. 6.1. It is noted that the biaxial modulus was not changed significantly, while the residual stress was decreased for about 30% after one hour in the humid environment. Figure 6.1 also shows that the change in the residual stress levels off after one hour. This indicates that the moisture absorption of the coatings were at equilibrium state after approximately one hour. Hence, it is reasonable to believe that the samples reached a equilibrium state of moisture absorption after 90 minutes in the humid environment.

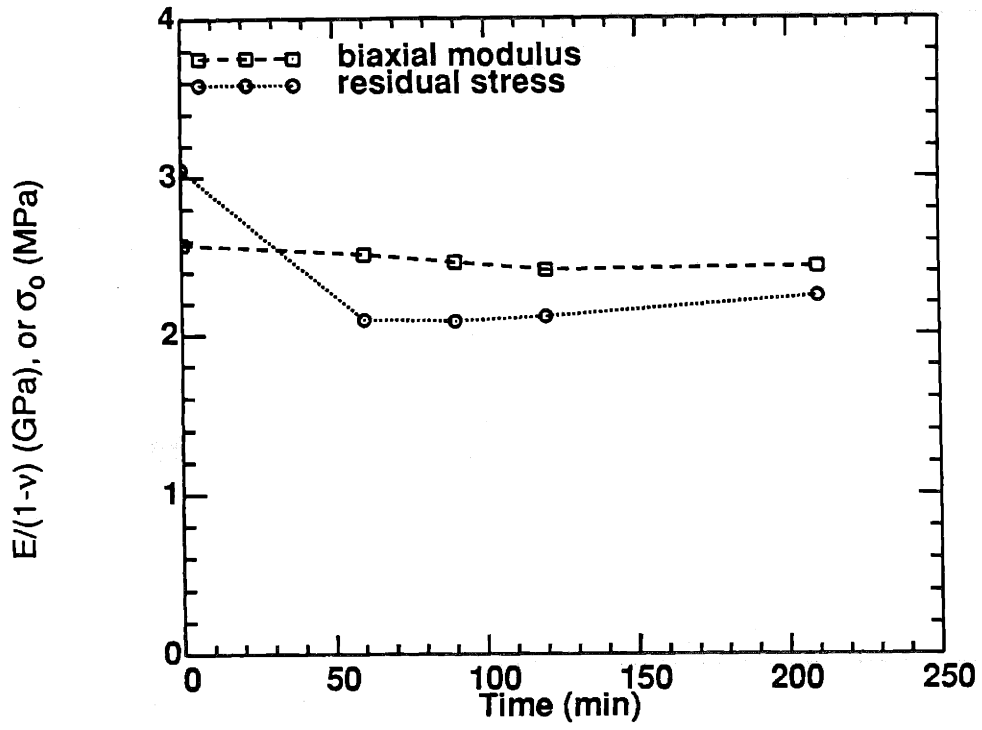

Figure 6.1 The biaxial modulus and residual stress versus time for a relative humidity change from 0% to 60% at room temperature for APC.

6.4.2 Humidity Effect on Mechanical Properties

The load-deflection data of APC are shown in Fig. 6.2. There were four different RH: 0%, 20%, 40%, and 60%. Each measurement at certain RH was repeated once. Figure 6.2 shows that the reproducibility of the measurements was reasonably good. The biaxial modulus and the residual stress were calculated from the slope and the intercept of the linear least-square fitting in Fig. 6.2. It is noted that the biaxial modulus of APC did not change significantly with the RH, while the residual stress of APC was decreased as the RH was increased.

Similarly, the biaxial modulus and the residual stress of APC-D and PEU were obtained as a function of RH. Thus, the biaxial moduli of APC, APC-D, PEU at 0% RH were calculated to be 2.6, 2.34, and 0.088 GPa, respectively. The residual stresses of APC, APC-D, PEU at 0% RH were 3.05, 3.06, and 0.748 MPa, respectively. Figure 6.3 shows the change in the biaxial modulus as a function of RH for APC, APC-D, and PEU. Similar to APC, the biaxial modulus of APC-D and PEU were not changed with RH. Figure 6.4 shows the change of the residual stress for these three coatings. It is found that the change in the residual stress decreased as the RH was increased. At 60% RH, the residual stress of PEU decreased to about 9% and the residual stress of APC and APC-D decreased up to 29% and 41%, respectively. These data indicates that the moisture absorbed in the coatings causes a significant decrease in the residual stress, while the biaxial modulus was not almost not affected. This implies that the water molecules inside coatings did not cause a significant plasticizing effect to decrease the value of modulus. The relaxation of the residual tensile stress is attributed to the swelling of coatings caused by the absorption of water molecules.

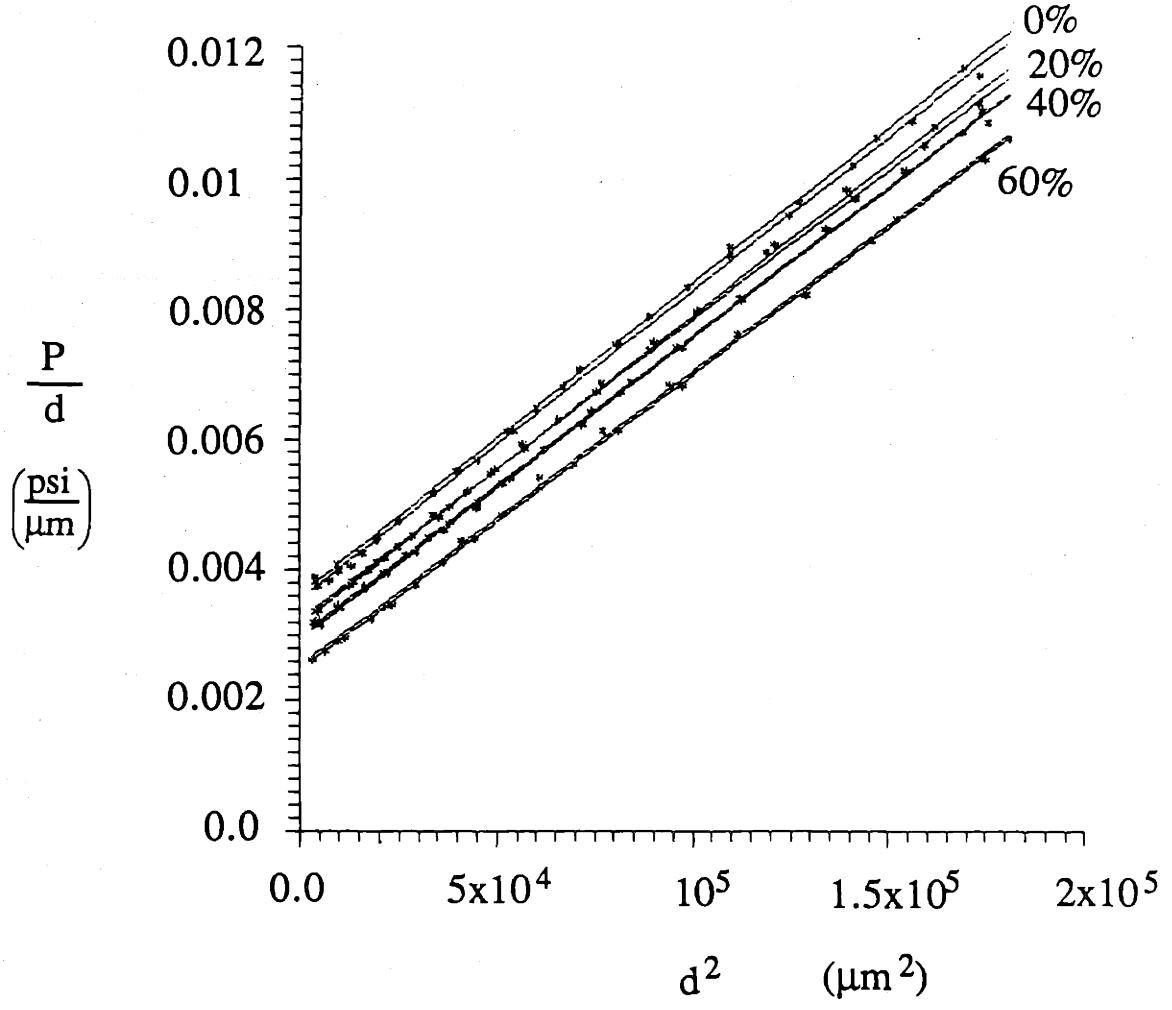

Figure 6.2 The pressure-deflection data for APC with different relative humidities. Each experiment was repeated twice.

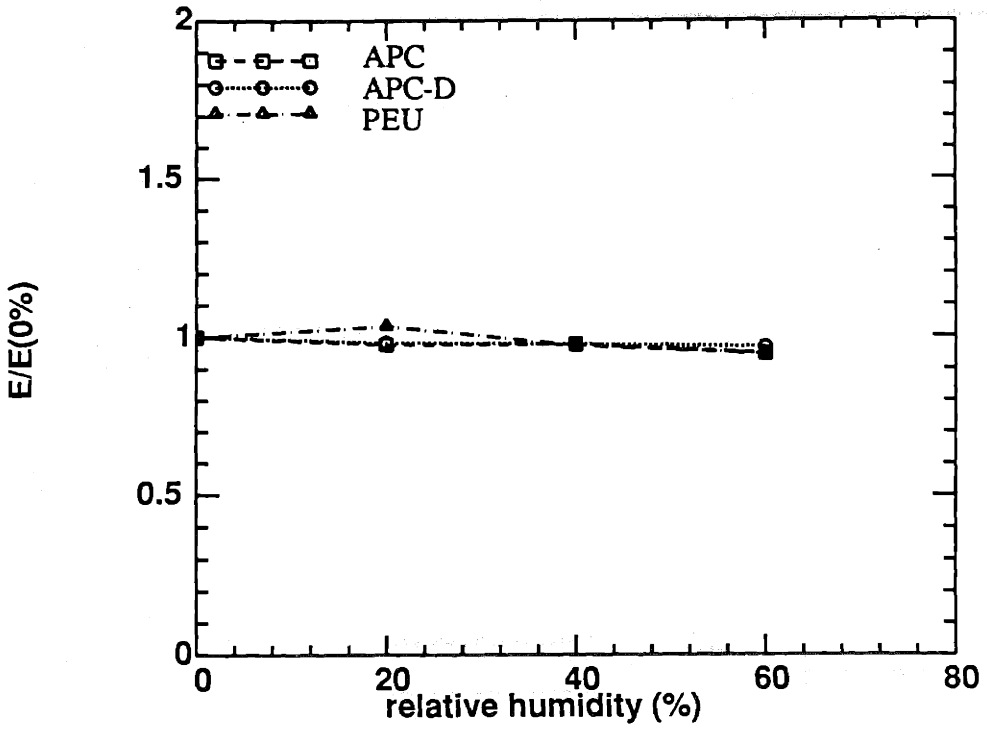

Figure 6.3 The change of the biaxial modulus of APC, APC-D, and PEU versus the relative humidity.

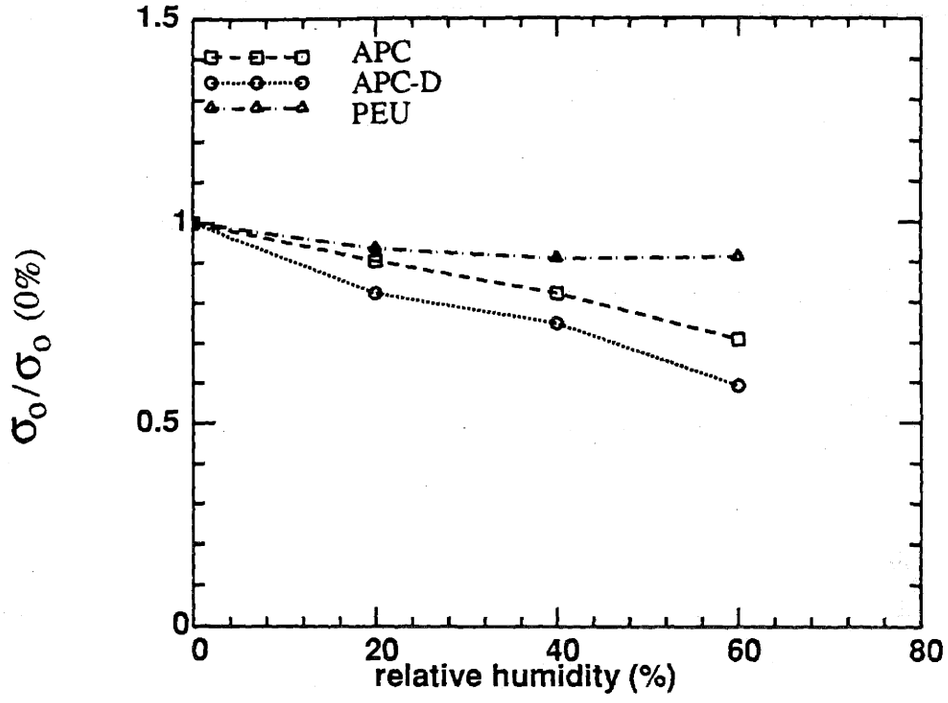

Figure 6.4 The change of the residual stress of APC, APC-D, and PEU versus the relative humidity.

6.5 Conclusion

The blister method were verified to be useful in studying the humidity effect of the biaxial modulus and the residual stress of coatings. The humidity causes a significant decrease in the residual stress but not in the biaxial modulus. It is found that the change of the residual stress can be as large as 40% at 60% RH.

CHAPTER 7

Summary and Conclusions

This thesis has discussed the *in situ* measurement of the mechanical properties of multi-layer films. The basic concept is to infer the mechanical properties of the films coated on top of previously-characterized films using the blister methods and corresponding mathematical models. This technique provided a new way to evaluate the mechanical properties of each layer in a multi-layer coating system. This work contained two main parts: the development of experimental techniques and the mathematical models.

The development of experimental techniques included sample fabrication and the measuring techniques. Both square and circular multi-layer samples were fabricated for this study. Polyimide, (PI) and three commercially available coatings were studied: acrylic polymer coating (APC), acrylic polymer coating with dispersed resin (APC-D), and polyester urethane (PEU). The design of the sample fabrication showed that the fabrication technique can be adopted easily by the coating industry for routine measurement.

Mathematical models for single-layer and multi-layer films were developed. Analytical solutions were used to obtain the form of the models and the finite element method (FEM) was used to evaluate the constants in these models. FEM analysis converged to the same deflection results regardless of the element type when the mesh was fine enough. The use of FEM was justified by showing the FEM predicted deflection shapes match the experimentally measured deflection shapes within 3%. When using FEM for the study of film deflection, certain restriction on the mesh of elements have to be

considered, such as the use of ratioed elements to avoid errors in center deflection. The thick-film model included the bending effect, caused by thickening films. The difference between the thin-film model and the thick-film model was two additional terms due to the bending effects. As the films get thicker, the thick-film model should be applied in order to avoid the error in evaluating the residual stress.

The Young's moduli of coatings were obtained from standard Instron tests for this comparison to the results of the blister test. The Instron test samples were made using the same technique as used for load-deflection tests. The in-plane Poisson ratio of coatings were evaluated by comparing the values of Young's modulus with the value of the biaxial modulus.

The mechanical properties of top layers were inferred from the measurements of single-layer and multi-layer films and hence, the mechanical properties of the first layer should be well characterized. Several different analyses were done for the first layer material: solvent effect, processing effect, strain rate effect, and humidity effect. The solvent effect showed that PI was not significantly affected by the solvent and the curing cycles. The process effect showed that both the biaxial modulus and residual stress of twice-cured coatings were higher than those of the once-cured coatings. The increase was as high as 93% for the biaxial modulus and 30% for the residual stress. The strain rate effect showed that the mechanical properties of films were decreased with the strain rate of the blister test. The blister method was verified to be useful in studying the humidity effect of the biaxial modulus and the residual stress of coatings. The humidity caused a significant decrease in the residual stress but not in the biaxial modulus. It was found that the change of the residual stress can be as large as 40% at 60% RH.

The mechanical properties of both the square and circular films were in agreement, which implies the models for both shapes were consistent. The mechanical properties evaluated from two-layer films were also in good agreement with the single-layer films, indicating the consistency between the single-layer and multi-layer models.

The limitations of this technique are first, the long processing time for sample fabrication and second, the accuracy in the evaluating the mechanical properties of multi-layer films more than three layers. The long processing time for preparing square samples can be cut by using the circular films. However, circular films were fabricated on the release layer (Tedlar®), from which the residual stress is much lower than those on well-adhered substrates.

The accuracy on the evaluation of two-layer films is about 15%. The accuracy of evaluating the mechanical properties of compliant materials on top of strong material is even lower. The accuracy of evaluating the mechanical properties of the three-layer and four-layer is poor also. The major factor causing this poor accuracy is the variation of thickness. If the variation of the thickness is improved, then the accuracy of this technique would certainly be improved as well.

References

1. T. A. Strivens, "Mechanical Properties of Paints and Coatings", in *Paint and Surface Coatings*, ed. R. Lambourne, John Wiley & Sons, New York, 1987.

2. S. Paul, *Surface Coatings*, Chap. 6, John Wiley & Sons, New York, 1985.

3. C. M. Hansen, "Polymer Coatings", *Ind. Eng. Chem. Prod. Res. Develop.*, **9 (3)**, 282, 1970.

4. A. A. Martynenko, "Residual Stresses in Multi-layer Coatings", *Strength of Materials*, **12**, 1448, 1980.

5. G. D. Cheever, "Analysis of Defects Occurring at Interfaces in Multi-layer Paint Systems on Polymeric Substrates", *J. Coating Tech.*, **58 (742)**, 25, 1986.

6. J. W. Beams, "Mechanical Properties of Thin Film of Gold and Silver", in *Structure and Properties of Thin Films*, ed. C. A. Neugebauer, J. B. Newkirk, and D. A. Vermilyea, John Wiley & Sons, New York, pp. 183-192, 1959.

7. R. Papirno, "Stress and Strain in Thin Films Bulged over Circular Openings", *J. Appl. Phys.*, **32**, 1175, 1961.

8. J. A. Hinkley, "A Blister Test for Adhesion of Polymer Films to SiO_2", *J. Adhesion*, **6**, 115, 1983.

9. E. I. Bromley, J. N. Randall, D. C. Flanders, and R. W. Mountain, "A Technique for the Determination of stress in Thin Films", J. Vac. Sci. Technol. B, **1 (4)**, 1364, 1983.

10. M. G. Allen, M. Mehregany, R. T. Howe, and S. D. Senturia, "Microfabricated structures for the in situ measurement of residual stress, Young's modulus, and ultimate strain of thin films", *Appl. Phys. Lett.*, **51 (4)**, 241, 1987.

11. O. Tabata, K. Kawahata, S. Sugiyama, and I. Igarashi, "Mechanical Property Measurements of Thin Films Using Load-Deflection of Composite Rectangular Membrane", Micro Electro Mechanical System (MEMS): An Investigation of Micro Structures, Sensors, Actuators, Machines, and Robots, IEEE, pp. 152, 1989.

12. F. Maseeh, and S. D. Senturia, "Elastic Properties of Thin Polyimide Films", in Polyimides: Materials, Chemistry, and Characterization", eds. C. Feger, M. M. Khojasteh, and J. E. McGrath, Elsevier Science Publishers B. V., Amsterdam, pp. 575, 1989.

13. J. W. Prane, "The Coating Industry: Economics and End-Use Market", in *Applied Polymer Science*, 2nd Ed., ed. R. W. Tess, and G. W. Poehlein, Am. Chem. Soc. Symp. Series 285, ACS, 1985.

14. W. C. Golton, and P. McGonigal, private communication.

15. W. Volkson, and P. M. Cotts, "Synthesis of Polyimides with Controlled Molecular Weights", in Polyimides – Synthesis, Characterization, and Application", ed. K. L. Mittal, Plenum, New York, p. 163, 1984.

16. G. M. Bower, and L. W. Frost, "Aromatic Polyimides", *J. Poly. Sci.*, **A1 (10)**, 3135, 1963.

17. F. Maseeh, M. A. Schmidt, M. G. Allen, and S. D. Senturia, "Calibrated Measurements of Elastic Limit, Modulus, and the Residual Stress of Thin Films Using Micromachined Suspended Structures", IEEE Solid-State Sensors Workshop, Hilton Head Island, S. Carolina, 1988.

18. D. Y. Perera, and D. Vander Eynde, "Solvent Influence on the Development of Internal Stress in a Thermoplastic Coating", *J. Coating Tech.*, **55 (699)**, 37, 1983.

19. S. G. Croll, "The Origin of Residual Internal Stress in Solvent-Cast Thermoplastic Coatings", *J. Appl. Polym. Sci.*, **23**, 847, 1979.

20. S. G. Croll, "Internal Strain in Solvent-Cast Coatings", *J. Coating Tech.*, **51 (648)**, 64, 1979.

21. S. G. Croll, "Adhesion Loss Due to Internal Stress", *J. Coating Tech.*, **52 (665)**, 35, 1980.

22. D. H. Smelt, D. A. Smith, and W. W. Harpur, "Investigation of failure in Paint films", *J. Mat. Sci.*, **14**, 2845, 1979.

23. K. L. Chopra, *Thin Film Phenomena*, Chap. 5, New York, 1969.

24. R. Glang, R. A. Holmwood, and R. L. Rosenfeld, "Determination of Stress in Films on Single Crystalline Silicon Substrates", *Rev. Sci. Instrum.*, **36 (1)**, 7, 1965.

25. D. S. Campbell, "Mechanical Properties of Thin Films", in *Handbook of Thin Film Technology*, eds. L. I. Maissel, and R. Glang, McGraw-Hill, New York, 1970.

26. P. M. Schaible, and R. Glang, "Automated Measurement of Stress in Thin Films", in *Thin Film Dielectrics*, ed. F. Vratny, Electrochem. Soc. Inc., New York, 1969.

27. R. W. Hoffman, "Stresses in the Films: the Relevance of Grain Boundaries and Impurities", *Thin Solid Films*, **34**, 185, 1976.

28. E. Klokholm, "An Apparatus for Measuring Stress in Thin Films", *Rev. Sci. Instrum.*, **40 (8)**, 1054, 1969.

29. R. J. Jaccodine, and W. A. Schlegel, "Measurement of Strains at Si-SiO_2 Interface", *J. Appl. Phys.*, **37 (6)**, 2429, 1966.

30. S. Jovanovic, and C. S. Smith, "Elastic Modulus of Amorphous Nickel Films", *J. Appl. Phys.*, **32**, 121, 1961.

31. E. M. Corcoran, "Determining Stress in Organic Coatings Using Plate Beam Deflection", *J. Paint Tech.*, **41 (538)**, 635, 1969.

32. D. Y. Perera, and D. Vander Eynde, *J. Coating Tech.*, **53 (678)**, 40, 1981.

33. T. S. Chow, C. A. Liu, and R. C. Penwell, *J. Poly. Sci., Poly. Phys. Ed.*, **14 (7)**, 1311, 1976.

34. A. Saarnak, E. Nilsson, and L. O. Kornum, "Usefulness of the Measurement of Internal Stresses in Paint Films", *J. Oil Col. Chem. Assoc.*, **59**, 427, 1976.

35. W. Buckel, "Internal Stress", *J. Vac. Sci. Tech.*, **6 (4)**, 606, 1969.

36. G. Stoney, *Proc. Roy. Soc. London A*, **82**, 172, 1909.

37. R. W. Springer, and R. W. Hoffman, "Growth Effects on Stress in Nickel Films", *J. Vac. Sci. Technol.*, **10 (1)**, 238, 1973.

38. A. Catlin, and W. P. Walker, "Mechanical Properties of Thin Single-Crystal Gold Films", *J. Appl. Phy.*, **31 (12)**, 2135, 1960.

39. S. T. Chen, C. H. Yang, H. M. Tong, and P. S. Ho, "Temperature Dependence of Stress Relaxation at the Copper/Polyimide Interface", in *Scattering, Deformation and Fracture in Polymers*, Mat. Res. Soc. Symp. Proc., eds. G. D. Wignall, B. Crist, T. P. Russell, and E. L. Thomas, vol. 79, 1987.

40. P. Geldermans, C. Goldsmith, and F. Bedetti, "Measurement of Stresses During Curing and in Cured Polyimide Films", in *Polyimides - Syntheses, Characterization, and Applications*, ed. K. L. Mittal, Plenum, New York, 1984, pp. 695.

41. K. Roll, "Analysis of Stress and Strain Distribution in Thin Films and Substrates", *J. Appl. Phys.*, **47 (7)**, 3224, 1976.

42. G. H. Olsen and M. Ettenberg, "Calculated Stress in Multilayered Heteroepitaxial Structures", *J. Appl. Phys.*, **48 (6)**, 2543, 1977.

43. H. Yamada-Kaneta, T. Ogawa, and K. Wada. "Elastic Calculation of the Thermal Strains and Stresses of the Multilayered Plate", *J. Appl. Phys.*, **62 (1)**, 62, 1987.

44. S. N. G. Chu, A. T. Macrander, K. E. Strege, and W. D. Johnson, Jr., "Misfit Stress in GaAs/InP Heteroepitaxial Structures Grown by Vapor-phase Epitaxy", *J. appl. Phys.*, **57 (2)**, 249, 1985.

45. Z. Feng and H. Liu, "Generalized Formula for Curvature Radius and Layer Stresses Caused by Thermal Strain in Semiconductor Multi-layer Structure", *J. Appl. phys.*, **54 (1)**, 83, 1983.

46. C. Bauer, and R. Farris, *Proc. Third Int'l Conf. on Polyimides*, ed. C. Feger, Society of Plastics Engineers, 1988.

47. M. G. Allen, Ph.D. Thesis, Department of Chemical Engineering, Massachusetts Institute of Technology, Cambridge, Mass., 1989.

48. F. Maseeh, Ph.D. Thesis, Department of Civil Engineering, Massachusetts Institute of Technology, Cambridge, Mass., 1990.

49. M. Mehregany, M. Allen, and S. D. Senturia, "The use of Micromachined Structures for the Measurement of Mechanical Properties and Adhesion of Thin Films", IEEE Solid-State Sensors Workshop, Hilton Head Island, S. Carolina, 1986.

50. L. W. Altschuler, and J. A. Simms, U. S. Patent No. 4,632,964 (30 December 1986).

51. J. A. Antonelli, and H. Clementon, U. S. Patent No. 4,591,533 (27 May 1986).

52. Frank Rohrhacher, private communication.

53. S. Paul, in ref. 2, Chap. 2, p. 181.

54. F. Maseeh, private communication.

55. J. Y. Pan, Ph.D. Thesis, Department of Electrical Engineering and Computer Science, Massachusetts Institute of Technology, Cambridge, Mass., in preparation.

56. J. P. Mario, Bachelor Degree student, Department of Electrical Engineering and Computer Science, Massachusetts Institute of Technology, Cambridge, Mass., 1980.

57. S. Timoshenko, *Theory of Plates and Shells*, Chap. 13, p. 396-400, McGraw-Hill, New York, 1940.

58. M. G. Allen, M. S. Thesis, Department of Chemical Engineering, Massachusetts Institute of Technology, Cambridge, Mass., 1986.

59. S. Timoshenko, in ref. 57, Chap. 13, p. 420, and Chap. 12, p.378-383.

60. A. Yasukawa, S. Shimada, Y. Matsuoka, and Y. Kanda, "Design Considerations for Silicon Circular Diaphragm Pressure Sensors", *Japanese J. Appl. Phys.*, **21 (7)**, 1049, 1982.

61. J. C. Lambropoulos and S. Wan, "Stress in Anisotropic Thin Films Bonded to Stiff Substrates", Mat. Res. Soc. Fall Meeting, Boston, Mass., 1987.

62. J. Y. Pan, P. Lin, F. Maseeh, and S. D. Senturia, "Verification of FEM Analysis of Load-Deflection Methods for Measuring Mechanical Properties of Thin Films", IEEE Solid-State Sensors Workshop, Hilton Head Island, S. Carolina, 1990.

63. S. S. Rao, *The Finite Element Method in Engineering*, Chap. 1, Pergamon Press, New York, 1982.

64. C. S. Desai, *Elementary Finite Element Method*, Chap. 2, Prentice-Hall Inc., Englewood Cliffs, New Jersey, 1979.

65. H. Kardestuncer, Chap. 3 (Part 2), in *Finite Element Handbook*, ed. H. Kardestuncer, and D. H. Norrie, McGraw-Hill, New York, 1987.

66. R. D. Cook, *Concepts and Applications of Finite Element Analysis*, 2nd Ed.,John Wiley & Sons, New York, 1974.

67. H. H. Fong, "A Commentary on Commercial Finite Element Systems", in ref. 69, p. 3.

68. O. C. Zienkiewicz, *The Finite Element Method*, Chap. 2, McGraw Hill, New York, 1977.

69. K.-J. Bathe, and G. Larsson, "The use of ADINA in Engineering Practice", in *Finite Element Systems: A Handbook*, ed. C. A. Brebbia, Springer-Verlag, New York, 1985.

70. K.-J. Bathe, and L. W. Ho, "Some Results in the Analysis of Thin Shell Structures", in *Nonlinear Finite Element Analysis in Structural Mechanics*, eds. W. Wunderlich, E. Stein, and K.-J. Bathe, Springer-Verlag, New York, 1981.

71. P. Lin, and S. D. Senturia, "The In-Situ Measurement of Biaxial Modulus and Residual Stress of Multi-layer Polymeric Thin Films", Material Research Society Spring Meeting, San Francisco, 1990 .

72. C. Goldsmith, P. Geldermans, F. Bedetti, and G. A. Walker, "Measurement of Stresses Generated in Cured Polyimide Films", *J. Vac. Sci. Tech.*, **A1 (2)**, 407, 1983.

73. J. Y. Pan, private communication.

74. A. E. Lever and J. A. Rhys, *Properties and Testing of Plastics Materials*, 3rd ed., Chemical Rubber Co., New York, 1968.

75. J. V. Schmitz, ed., *Testing of Polymers*, Vol. 2, Wiley-Interscience, New York, 1966.

76. U. Zorll, "The Effect of Climatic Stress on the Mechanical Behavior of Topcoats in Multi-layer Coatings", *Dtsch. Farben-Z*, (in German, translated into English by DuPont), **33 (9)**, 300, 1979.

77. D. D. Denton, D. R. Day, D. F. Priore, and S. D. Senturia, "Moisture Diffusion in Polyimide Films in Integrated Circuits", *J. Elect. Mat.*, **14 (2)**, 119, 1985.

78. D. D. Denton, J. B. Camou, and S. D. Senturia, "Effect of Moisture Uptake on the Dielectric Permittivity of Polyimide Films", Moisture and Humidity Spring Meeting, Washington D. C., 1985.

79. S. D. Senturia, "Studies of Moisture in Polyimide: A Summary", RADC/NBS Workshop on Moisture Control for Microelectronics", 1986.

80. B. S. Berry, and W. C. Pritchet, "Bending-Cantilever Method for the Study of Moisture Swelling in Polymers", *IBM J. Develop.*, **28 (6)**, 662, 1984.

81. B. L. Deopura, A. K. Sengupta, and A. Verma, "Effect of Moisture on Physical Properties of Nylon", *Polymer Communications*, **24**, 287, 1983.

82. H. Lee, and K. Neville, Handbook of Epoxy Resins, McGraw-Hill, New York, 1967.

83. Pradnya V. Nagakar, private communication.